

## ABSTRACT

Title of dissertation: MODELING THE RESUPPLY, DIFFUSION,  
AND EVAPORATION OF CESIUM  
ON THE SURFACE OF CONTROLLED  
POROSITY DISPENSER PHOTOCATHODES

Zhigang Pan, Doctor of Philosophy, 2013

Dissertation directed by: Professor Patrick O'Shea & Dr. Kevin L. Jensen  
Department of Physics

High quantum efficiency (QE) photocathodes are useful for many accelerator applications requiring high brightness electron beams, but suffer from short operational lifetime due to QE decay. For most photocathodes, the decrease in QE is primarily attributed to the loss of a cesium layer at the photocathode surface during operation. The development of robust, long life, high QE photoemitters is critically needed for applications demanding high brightness electron sources. To that end, a controlled porosity dispenser (CPD) photocathode is currently being explored and developed to replace the cesium during operation and increase photocathode lifetime. A theoretical model of cesium resupply, diffusion, and evaporation on the surface of a sintered wire CPD photocathode is developed to understand and optimize the performance of future controlled porosity photocathodes. For typical activation temperatures within the range of 500K–750K, simulation found differences of less than 5% between the quantum efficiency (QE) maximum and minimum over ideal homogenous surfaces. Simulations suggest more variation for real cases

to include real surface non uniformity. The evaporation of cesium from a tungsten surface is modeled using an effective one-dimensional potential well representation of the binding energy. The model accounts for both local and global interactions of cesium with the surface metal as well as with other cesium atoms. The theory is compared with the data of Taylor and Langmuir comparing evaporation rates to sub-monolayer surface coverage of cesium, gives good agreement, and reproduces the nonlinear behavior of evaporation with varying coverage and temperature.

MODELING THE RESUPPLY, DIFFUSION, AND  
EVAPORATION OF CESIUM ON THE SURFACE OF  
CONTROLLED POROSITY DISPENSER PHOTOCATHODES

by

Zhigang Pan

Dissertation submitted to the Faculty of the Graduate School of the  
University of Maryland, College Park in partial fulfillment  
of the requirements for the degree of  
Doctor of Philosophy  
2013

Committee members:

Professor Patrick G. O'Shea, Chair/Advisor

Dr. Kevin L. Jensen, Co-Advisor NRL

Dr. Rami A. Kishek

Dr. Thomas M. Antonsen

Dr. Gregory S. Nusinovich

Deans Representative:

Dr. John Melngailis

© Copyright by  
Zhigang Pan  
2013

## Dedication

To my loving wife Jenny, my family and relatives, the amazing colleagues I work with at school as well as at NRL, and all the friends and families at Grace Fellowship who have made these 5 years of graduate school a very pleasant and rewarding experience.

## Acknowledgments

There are many people who have helped me get to where I am today both academically as well as spiritually whom I would like to thank here.

First, I want to thank my wife Jenny. Meeting you and getting to know you during my time as a graduate student has been one of the most happiest and rewarding moments of my life. Your love and continued support at home has been so valuable for me during these past two years of marriage. Thank you for all your encouragement and for believing in me through this whole process.

The next person whom I would like to thank is my advisor Dr. O'Shea. It was your constant support and words of wisdom that have allowed me to become a better researcher as well as finish my dissertation. I remember that I was just a summer intern when I started doing work in your research group. Thank you for giving me the opportunity to work under your mentorship at the University of Maryland College Park. Your patience and support throughout the years have been so valuable to me and my family during my time here at UMD. May you continue to use your leadership and wisdom to inspire many other young minds and students in the years to come.

The third very important person whom I would like to thank is my colleague as well as work mentor Kevin Jensen. Thank you Kevin for giving me the opportunity to come and do my graduate school research at the Naval Research Laboratory. Sharing an office with you at NRL has been both fun as well as rewarding. Thank you for all your guidance in research as well as your frequent good humor that make

work both productive as well as enjoyable.

The fourth group of people that I want to thank is my family. Getting to where I am today would not have been possible without the support and nurture of my mother Jianying Li, father Qiyuan Pan, and sister Jane Pan. Thank you mom for all those delicious home cooked meals. Thanks dad for all your help and advice during as well as after the home buying process. Thanks Jane for all your silly jokes and youtube videos that are absolutely hilarious.

I also would like to thank all the friends and families at the Chinese Grace Fellowship at College Park. Thank you Simon for allowing the fellowship to be like a second extended family for me during my time at College Park. I am very grateful to have had the opportunity to serve as a co-leader at the fellowship. I has been a blessing to know you as well as your wife Maggie during these past years. May God continue to use you and the fellowship to take care of the needs of the many students that come far away from China to study at the University of Maryland.

Finally, I want to thank the God whom I serve Jesus Christ for His continued presence and guidance in my life. I pray that God will continue to lead me after graduate school and use me for his purposes wherever he choses to take me and my family.

# Table of Contents

List of Figures	vii
1 Introduction	1
1.1 Historical Background of CPDs . . . . .	4
1.2 Present Challenges for Developing CPD Photocathodes and Scope of the Dissertation . . . . .	7
1.3 Chapter Conclusions . . . . .	8
2 Roadmap to Modeling Controlled Porosity Dispenser Photocathode Perfor- mance	10
2.1 Cesium Migration to the Surface . . . . .	11
2.2 Cesium Spreading Across the Surface . . . . .	12
2.3 Cesium Leaving the Surface . . . . .	12
2.4 Results . . . . .	13
2.5 Discussion . . . . .	13
2.6 Chapter Conclusions . . . . .	15
3 Modeling Cesium Flow from the Reservoir to the Surface	16
3.1 Modeling $\Theta_{pore}$ . . . . .	17
3.2 Flux Due to Pore Walls $J_z^w$ . . . . .	21
3.3 Assumptions of the model . . . . .	24
3.4 Modeling CPD Lifetime . . . . .	26
3.4.1 Comparison between Circular and Noncircular Pores . . . . .	29
3.5 Chapter Conclusions . . . . .	31
4 Diffusion	32
4.1 Fick's Law and the Diffusion Equation . . . . .	32
4.2 Numerical Methods Used for Modeling . . . . .	34
4.2.1 Discreet Laplacian and Gradient Operators on a Hex Lattice .	36
4.2.2 Discretizing the Nonlinear Diffusion Equation Implicitly in Time	39
4.3 Diffusivity Measurements of Cs:W in Literature . . . . .	41
4.4 Chapter Conclusions . . . . .	44
5 Evaporation of Cesium off Cathode Surfaces	45
5.1 Previous Evaporation Studies . . . . .	45
5.1.1 Becker's Experiment . . . . .	46
5.1.2 Langmuir's Evaporation Studies . . . . .	48
5.1.3 Discussion and Summary of Previous Studies . . . . .	50
5.2 Overview of the Evaporation Model . . . . .	51
5.3 Calculating the Evaporation Probability "P" and $V_0$ . . . . .	54
5.3.1 The Coulomb Contribution to $V_0$ . . . . .	58
5.3.2 The Lennard-Jones Contribution to $V_0$ . . . . .	66
5.3.3 The Thermodynamic Contribution to $V_0$ . . . . .	67

5.3.4	Summary . . . . .	68
5.4	Calculating time $\tau$ . . . . .	68
5.5	Limitations of the Model and Future Work . . . . .	72
5.6	Chapter Conclusions . . . . .	74
6	Simulations of Cesium Tungsten Controlled Porosity Dispenser Photocathode . . . . .	75
6.1	Results for Modeling the Cesium Flow through CPD Pores . . . . .	75
6.2	Results for Modeling Cesium Evaporation rates off CPD surfaces . . . . .	80
6.3	Simulations for the QE map of a CPD photocathode . . . . .	82
6.4	Chapter Conclusions . . . . .	86
7	Concluding Remarks . . . . .	88
7.1	Discussion of Results . . . . .	88
A	Main Source Code in MATLAB . . . . .	91
B	Functions and Subroutines . . . . .	113
	Bibliography . . . . .	120

## List of Figures

1.1	Quantum efficiency (y-axis) vs $1/e$ lifetime for some common photocathode materials. Notice all high efficiency photocathodes have Cs in their formula [36]. . . . .	3
1.2	Cross section schematic of thermionic CPD cathode prototype first developed by Falce and Thomas. Fig obtained from [12]. . . . .	5
1.3	Comparison of emission images [54]. (a) Type-B cathode at $0.6 \text{ A/cm}^2$ (b) CPD cathode at $0.7 \text{ A/cm}^2$ . . . . .	6
1.4	SEM image of a CPD surface formed by stacking and sintering 20 micron diameter tungsten EDM wire [19]. . . . .	7
3.1	Diagrammatic overview of modeling the cesium resupply rate the the surface . . . . .	17
3.2	Schematic diagram of flux onto the differential wall element $dA_z$ due to evaporation from $dA_w$ . . . . .	21
3.3	Schematic diagram of flux through the differential area element $d\mathbf{A}$ due to evaporation from $d\mathbf{S}$ . . . . .	27
3.4	Circular cross section where the shape factor $\langle \cos \psi \rangle_A$ is independent with respect to location around the perimeter . . . . .	29
3.5	The shape factor $\langle \cos \psi \rangle_A$ for a triangular pore is dependent with respect to location but is bounded by the two cases shown above. . .	30
4.1	SEM image of the sintered wire CPD cathode surface. Highlighted red region represents the region that is modeled assuming periodic boundary conditions. . . . .	35
4.2	Schematic wire stencil of the hexagonal grid showing the discretization parameter $h$ as well as the points used to evaluate the Laplacian operators. . . . .	37
4.3	The numbering scheme used for the numerical discretization of the hexagonal lattice. $N_D^j$ are the number of grid points contained in the $j$ th diagonal. . . . .	40
5.1	Filament and collector arrangement for Langmuir's setup [53]. . . . .	49
5.2	Arrangement of a cesium atom on the [100] surface of tungsten. . . . .	53
5.3	Effective 1D potential well used to model the evaporation. . . . .	56
5.4	Cesium interaction with image charge and nearest neighbor . . . . .	63
6.1	Results from modeling the cesium coverage along the pore walls as a function of distance down the pore . . . . .	76
6.2	Schematic overview of the hybrid CPD dispenser [34]. The cesium throughput is limited and controlled by adding a sintered tungsten powder diffusion barrier between the reservoir and the CPD emitter [35]. . . . .	78

6.3	Extrapolated curves from Langmuir’s paper [53] for cesium coverage at various cesium vapor pressures. The coverage maintained goes linear in temperature over a wide range of temperatures, especially for lower vapor pressures. . . . .	79
6.4	Comparison between theory and experimental data for evaporation of cesium off tungsten . . . . .	81
6.5	Results for modeling the cesium coverage $\theta$ and the corresponding QE map across the surface for an operating temperature of 500 K at a wavelength of 475 nm . . . . .	83
6.6	Simulations of Averaged QE of Cs:W as a function of Temperature and various wavelengths (nm) . . . . .	84
6.7	Results for modeling the QE map across the surface for an operating temperature of 500 K when two out of six pores are clogged . . . . .	85

# Chapter 1

## Introduction

Free Electron Lasers (FELs) are light sources that emit coherent radiation by passing a relativistic beam of electrons through a series of magnets called an “undulator” [43]. In order to reduce space charge induced effects such as beam breakup [56, 42, 9], radio frequency (rf) electric fields are typically used [28] to quickly accelerate the electron beam to relativistic speeds. Accelerators that employ rf fields to accelerate charged particles are called rf linear accelerators (rf-linacs). The peak rf field gradients inside these accelerating structures can be as high as several hundred MV/m [9, 40]. Within the rf field cavities, the electric fields oscillate with frequencies on the order of a GHz. For the half rf period corresponding to acceleration in the forward direction, only a few degrees of phase (typically a few picoseconds) around the maximum field amplitude do the electrons get optimally accelerated. Therefore, the electron beam going into the rf cavities needs to be in the form of a pulse train of electron bunches, with each bunch matched to the correct phase and length necessary to be optimally accelerated by the rf fields.

For this reason, laser switched photocathodes are electron sources suitable for direct injection into rf linacs because they can be switched on and off very fast by pulsing the drive laser. In photoemission, incident photons from the drive laser excite the electrons near the surface of the material to be emitted. The rapid switching

from the drive laser enables photocathodes to emit short bunches of electrons at frequencies equal to or at a subharmonic of the frequencies of the rf-fields.

For photocathodes, the ratio of the number of electrons emitted per incident photon is called the quantum efficiency, or QE. Higher QE results in higher charge per bunch emitted from the photocathode. A high QE ( $\geq 10\%$ ) photocathode is desirable for high peak and high average current accelerator applications involving electron beams, such as but not limited to future high performance FELs [24].

A.H. Sommer summarized the development of photocathodes from 1930 to 1980 [50]:

Basic science contributed only one important rule in the search for new cathodes. This rule states that whatever cathode material synthesized, the photoemissive performance is enhanced by the incorporation of cesium. (A.H. Sommer 1982)

The presence of cesium (Cs) serves to lower the electron binding energy near the surface of the material, greatly enhancing emission [55]. For the purposes of this thesis, the term “workfunction” is synonymous with the barrier height in the absence of an applied field for cesium on metal. Workfunction lowering by sub-monolayer coverages of cesium on the surface has been treated in detail by Gyftopoulos and Levine [16].

Fig 1.1 shows a graph of the QE vs lifetime of some common photocathodes [36]. As shown in Fig 1.1, all high QE photocathodes have Cs in their chemical formula. From the graph, there is a noticeable trend between higher QE and lower

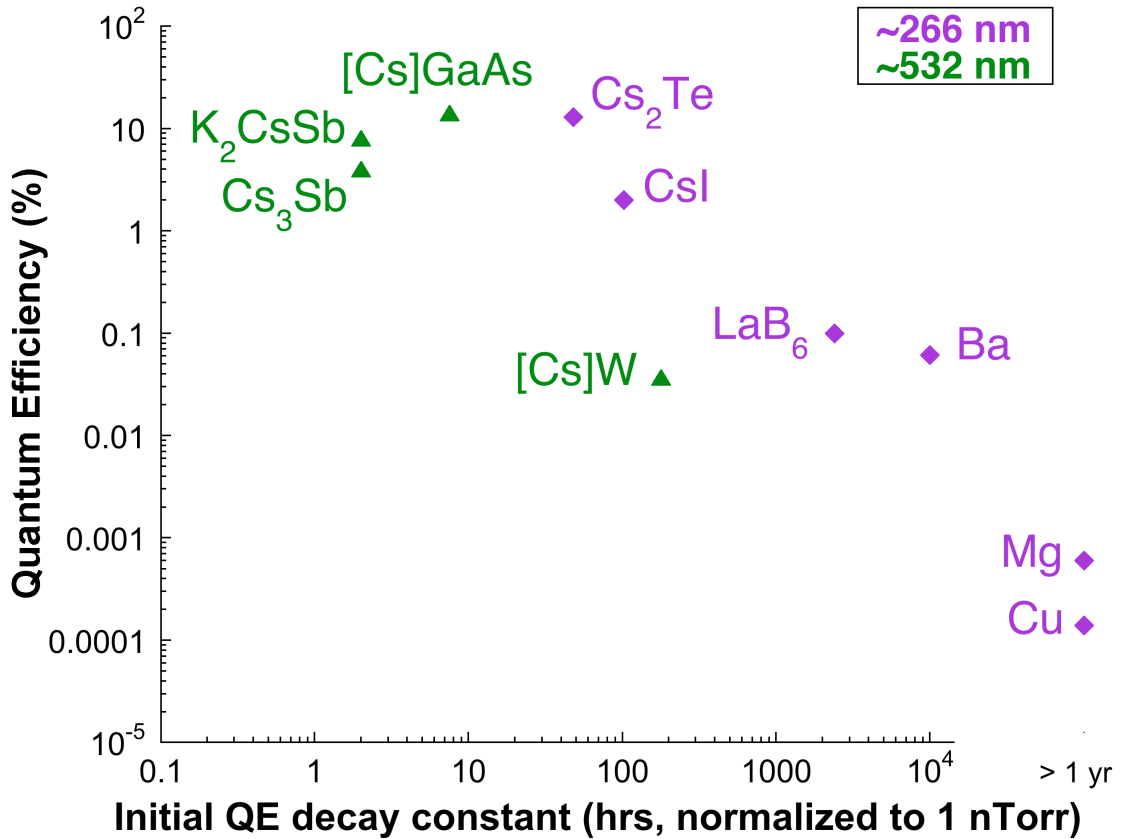


Figure 1.1: Quantum efficiency (y-axis) vs  $1/e$  lifetime for some common photocathode materials. Notice all high efficiency photocathodes have Cs in their formula [36].

photocathode lifetime. This downward trend is one of the primary challenges limiting modern high QE photocathodes. For many applications including FELs, the short lifetime greatly limits the photocathodes usefulness and reliability.

The reason for this decrease in lifetime lies in the continuous loss of Cs atoms at the surface during operation, causing QE to drop quickly [39]. The thin layer of Cs atoms at the cathode surface is very easily lost to evaporation or contamination during operation. The technology gap for a high QE and long lifetime photocathode is clearly seen from Fig 1.1. In order for photocathodes to remain useful for

future high brightness electron beam applications such as FELs, novel techniques need to be developed to make the Cs layer on the surface robust to evaporation and contamination in the harsh operating environment of an rf photoinjector. The proposed method to accomplish this borrows an idea from another cathode technology, thermionic barium (Ba) dispenser cathodes, where the Ba at the surface is replaced in-situ from a Ba reservoir within the bulk cathode material [23]. The research presented in this dissertation seeks to fill the technology gap shown in Fig 1.1 by the modeling and design of a controlled porosity dispenser (CPD) photocathode to dispense and replace lost Cs instead of Ba, thereby extending photocathode lifetime.

## 1.1 Historical Background of CPDs

Experiments at the University of Maryland College Park have shown that recessiating the surface of Cs-based photocathodes can indeed restore QE back up to the original value [38]. The experiments support the claim that if one is able engineer photocathodes to replace lost cesium on the surface during operation, the lifetime could be greatly extended [33]. A sought after solution to fill the technology gap has been to replace the lost cesium in-situ through a controlled periodic array of pores on the cathode surface leading down to a cesium reservoir beneath [37].

A dispenser with a periodic array of pores leading from the reservoir to the surface is known as a controlled porosity dispenser (CPD) cathode. To allow for greater reproducibility, controlled resupply, and uniformity in emission on the surface, a CPD photocathode is desired. CPD cathodes have been previously studied

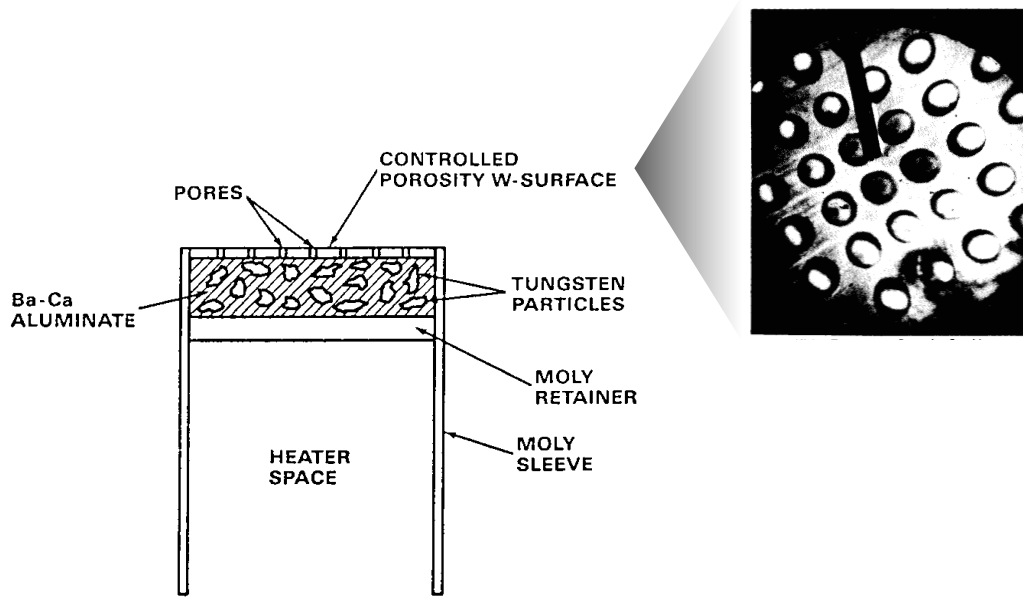


Figure 1.2: Cross section schematic of thermionic CPD cathode prototype first developed by Falce and Thomas. Fig obtained from [12]

for the application of barium based thermionic dispenser cathode. This section gives a short background of the previous advancements in CPD technology and put the present dissertation into perspective.

An iridium-barium oxide controlled porosity dispenser(CPD) cathode was first investigated and developed by L.R. Falce and R.E. Thomas at the Naval Research Laboratory in 1978 [12]. The cathode uses an iridium coated molybdenum foil containing an array of holes 0.001” in diameter formed by photolithography techniques. A schematic of their CPD design is shown in figure 1.2. The periodic array of holes allows for BaO to migrate to the surface from a reservoir behind the controlled porosity iridium foil. At the time, the design for a CPD thermionic cathode was a novel concept and promised increased emission uniformity, controllable rejuvenation rate of Ba or BaO, as well as much better performance reproducibility than conven-

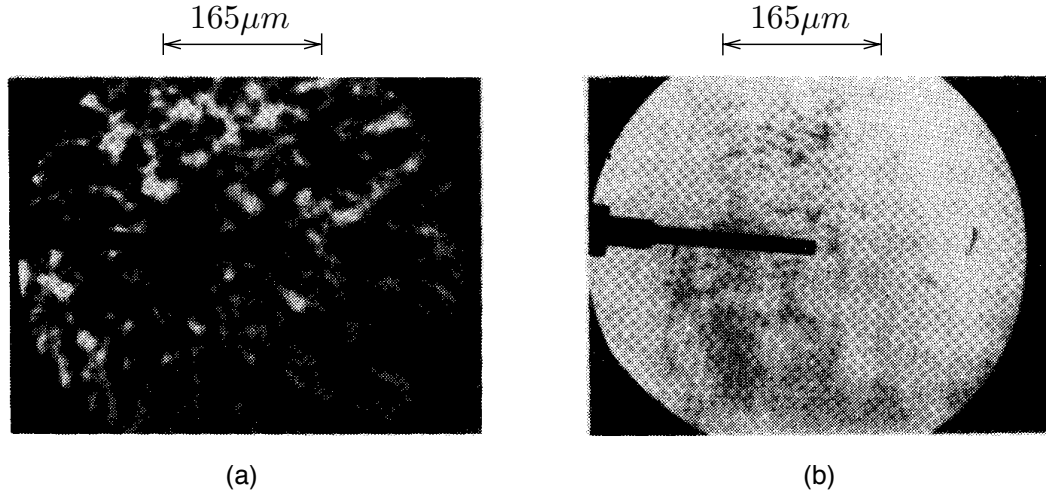


Figure 1.3: Comparison of emission images [54]. (a) Type-B cathode at  $0.6 \text{ A/cm}^2$   
 (b) CPD cathode at  $0.7 \text{ A/cm}^2$

tional impregnated dispenser cathodes. Fig 1.3 compares the emission uniformity between a CPD and a type B impregnated thermionic cathode operating with similar currents [54]. As shown in the figure, a CPD dispenser cathode emits current considerably more uniformly than traditional impregnated cathodes.

Although the CPD concept developed in the 1980s was novel and offered great potential in improving dispenser cathodes, it was too difficult and expensive to fabricate in batch processing mode. At the time, the array of micron diameter holes either had to be laser drilled or etched. Both of the two techniques were very inefficient as well as too costly for CPDs to be useful at the time [54]. Because of this, further development of CPDs was abandoned for a number of years.

It was not until 2005, that Lawrence Ives et al. [20] developed a novel and inexpensive process for practically manufacturing CPD tungsten cathodes. Their technique was based on an experiment performed in 1957 by Alexander and Balluffi[1].

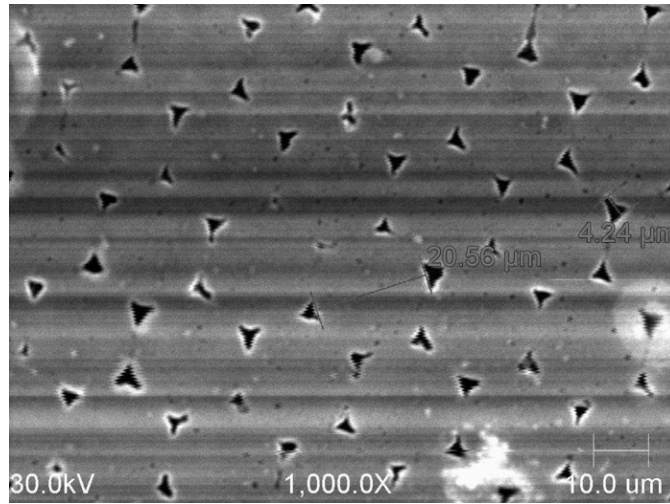


Figure 1.4: SEM image of a CPD surface formed by stacking and sintering 20 micron diameter tungsten EDM wire [19].

The process consists of sintering together micron diameter tungsten wires under high heat around 2000 C°. When the sintering is performed over time, a hexagonal pattern of pores is formed throughout the tungsten material. Figure 1.4 shown a SEM image of a CPD surface formed by sintering 20 micron diameter tungsten wire at 2075 C° for 75 min. This new method of fabricating CPD arrays from sintered tungsten wire is attractive because it is cheap and unlike alternative methods such as laser drilling or focused ion beam drilling, scales well to large numbers of pores.

## 1.2 Present Challenges for Developing CPD Photocathodes and Scope of the Dissertation

While CPDs have initially been developed as thermionic dispenser cathodes, a new area of research is to design CPDs as dispenser photocathodes. The techniques

developed by Lawrence Ives et al. [19] are readily adaptable for the fabrication of sintered wire CPD photocathodes. However, because of the novel nature of the technology, there is a lack of a physical model designed to simulate CPD photocathodes during operation. Such a model would not only serve as an efficient diagnostics tool for the future design of CPD photocathodes, but also greatly aid in efficient optimization of minimum CPD operating temperatures [44]. With that point, there are three major physical processes that happen for CPDs which need to be understood and modeled simultaneously:

1. Cesium flow and resupply from the reservoir through the pores onto the surface
2. Cesium diffusion across the surface from the pores
3. Cesium evaporation off the CPD pores and surface during operation

Such is the scope of this present dissertation. The next chapter will give a roadmap for modeling each of these processes on the surface of CPD photocathodes.

### 1.3 Chapter Conclusions

- Laser switched photocathodes are the electron source of choice for producing short pulse, high peak current electron beams required by many applications, of which the most demanding are next generation Free Electron Lasers (FELs) [10].
- There is currently a technology gap for a photocathode that is both robust and efficient.

- The tradeoff in lifetime and quantum efficiency is due to the loss of cesium at the surface.
- Controlled Porosity Dispenser Photocathodes (CPDs) promise to replace the cesium as it's being lost, so there is a significantly improved tradeoff between lifetime and quantum efficiency.
- Modeling the resupply, diffusion, and cesium loss through evaporation of the surface of a CPD is needed to predict its performance during operation as well as optimize design parameters.

## Chapter 2

### Roadmap to Modeling Controlled Porosity Dispenser Photocathode

#### Performance

Beginning with the end in mind, the ultimate goal in this study is to simulate the surface of a controlled porosity dispenser photocathode (CPD) during operation. The purpose of this chapter is to outline the approach used to model the surface of a CPD as well as introduce the remaining chapters in this dissertation. The equation used to model the surface is presented below:

$$\frac{\partial \Theta}{\partial t} = \nabla \cdot [D(T)\nabla \Theta] - F_{evap} \quad (2.1)$$

$$\Theta(\Omega) = \Theta_{pore}, \quad \Omega \in \text{pore edges}$$

Eq (2.1) captures the three major processes that occur simultaneously at the CPD surface. The first is the flow of cesium through the source pores onto the surface. This is included by fixing the the pore boundaries,  $\Omega$ , to be at a constant equilibrium coverage  $\Theta_{pore}$ . The second is the spreading of the cesium across the surface via diffusion. The diffusion term  $\nabla \cdot [D(T)\nabla \Theta]$  takes into account temperature dependent diffusivities for cesium on the cathode surface. The third is the continued loss of cesium at the surface due to evaporation. This process is accounted for by evaporation loss term  $F_{evap}$ . In the end, these three processes are integrated into one equation which governs the evolution of the cesium coverage across the surface of a CPD. While Eq (2.1) may look deceptively simple, solving it to produce a realistic

predictive model of the CPD is nontrivial and will be the focus of this dissertation. The next couple of sections will give a breakdown overview of the remaining chapters in this dissertation. The last two sections in this chapter will discuss some general assumptions made by the modeling followed by chapter conclusions.

## 2.1 Cesium Migration to the Surface

The first process to be covered in chapter 3 is the diffusion and cesium flow through the pores from the reservoir beneath the CPD to the surface. Preceding the cesium diffusion and evaporation at the CPD surface, the atoms need to get from the reservoir to the surface in the first place. A model for cesium transport along the walls of the pores up to the surface is presented in chapter 3 and will serve to determine the boundary condition  $\Theta_{pore}$  in Eq (2.1).

During rejuvenation, the reservoir is heated and cesium vapor is released inside. Since gas flows down a pressure gradient, there will be a net flow of cesium atoms from the reservoir with a high partial vapor pressure of cesium, down each source tube towards the surface of the cathode which is maintained in vacuum. Furthermore, there will also be a net diffusion of cesium along the pore walls towards the surface. The model of cesium transport through the pores accounts for three physical processes: 1) the diffusion of cesium along the walls of the pore, 2) Knudsen flow transport and flux onto the pore walls, and 3) the evaporation loss of cesium along the pore walls during rejuvenation. These three processes work together to maintain an equilibrium coverage,  $\Theta_{pore}$ , at the pore boundaries on the surface.

The last section in chapter 3 presents a model of CPD lifetime. The equations governing total cesium flow out of each pore are derived. Furthermore, comparisons between pores having a circular cross section to those having a triangular cross section are made. It is argued that difference between the two geometries are negligible. Therefore, the model is justified into approximating the triangular-like pores in Fig 1.4 as cylindrical.

## 2.2 Cesium Spreading Across the Surface

Chapter 4 will focus on modeling the spreading out of the cesium as it moves from a higher concentration to lower concentration across the surface, commonly referred to as diffusion. Diffusion is described by Fick's Law which simply states that a collection of atoms goes from higher concentration to lower concentration on average. In order to numerically solve 2D diffusion efficiently for the CPD geometry in question, numerical techniques are developed for the diffusion operator on a triangular net lattice grid mesh. A triangular grid faithfully reproduces the geometry of the CPD pore arrangement but additionally has greater accuracy than a square grid in modeling diffusion.

## 2.3 Cesium Leaving the Surface

Modeling cesium evaporation, the third physical process which occurs on a CPD surface, is covered in chapter 5. Cesium loss from cathode surfaces, if not replaced, is the main reason why photocathodes lose QE over time as explained

in the first chapter. For CPDs, the evaporation will work in conjunction with the resupply of cesium from the pores as well as diffusion to maintain an equilibrium coverage of cesium  $\Theta$  averaged across the surface. A first-principles analytic model for cesium evaporation off of tungsten was developed. The model takes into account cesium nearest neighbor interactions on the surface as well as captures the nonlinear coverage and temperature dependence of  $F_{evap}$ .

## 2.4 Results

Chapter 6 presents the results obtained for modeling the surface of a CPD tungsten photocathode using Eq (2.1). Results for modeling the cesium migration along the pore walls during rejuvenation as well as the model for cesium evaporation are presented. The methods used for modeling cesium resupply (chapter 3), diffusion (chapter 4), and evaporation (chapter 5) are all combined to yield a map of the surface over time as the cathode is being rejuvenated. The QE is also calculated from the cesium coverage. Different ideal and non ideal cases for a CPD surface were simulated the results are compared. This completes the modeling for a CPD photocathode.

## 2.5 Discussion

The CPD photocathode modeled in this dissertation is a cesiated tungsten photocathode. There are several reasons why the cesium on tungsten is modeled. First, tungsten-cesium is a widely studied system which can serve as a surrogate

for many other materials. The model developed here is broadly applicable across a range of alkali metal adsorbates and transition metal substrates. For examples of prior work on Na, K, and Cs on W see [32]. Second, while high QE photocathodes are usually complex multi-coating cesiated semiconductors [22], the binary cesium on tungsten system provides a stepping stone to model more complicated systems. A proof of principle study is first needed. Once the model has been proven for simple systems, it can then be further modified to describe systems of higher complexity or similar binary systems with alkali metal adsorbate and transition metal substrates. Finally, note that the CPD photocathodes currently in the process of being fabricated and tested are made from tungsten wires. As mentioned in the previous chapter, the method is adopted from the techniques developed by Lawrence Ives et. al. for thermionic barium CPD cathodes [19]. Therefore, modeling the cesium-tungsten binary system first allows for comparison with experiment.

There are some general simplifications that Eq (2.1) makes. First, cesium atoms are lost not only through evaporation from the surface, but also through contaminants from the vacuum environment. Ion back bombardment at high energies (high photo injector field strengths) also causes the surface to degrade and get damaged over time. So the question becomes whether the lifetime is contamination limited or evaporation limited. Eq (2.1) in this study assumes that lifetime is evaporation limited.

Additional assumptions that are made specifically for modeling resupply (Chapter 3), diffusion (Chapter 4), and evaporation (Chapter 5) are presented in their corresponding chapters.

## 2.6 Chapter Conclusions

- The ultimate goal in this study is to simulate the coverage of cesium on the surface of a tungsten based controlled porosity dispenser photocathode (CPD). The specific cathode is fabricated by stacking and sintering micron diameter tungsten wires, described in Chapter 1 (Fig 1.4).
- The equation used to model the resupply and coverage of cesium across the surface of a CPD during operation is given by Eq (2.1).
- Eq (2.1) accounts for the three physical processes that occur simultaneously for a CPD: 1) Cesium resupply to the surface through the source pores. 2) Cesium diffusion across the surface 3) Cesium loss through evaporation off the surface.
- The model for cesium migration and resupply to the surface through the source pores is presented in chapter 3.
- The numerical methods used to model cesium diffusion across the surface are presented in chapter 4.
- The analytic model developed for cesium evaporation off the surface, which accounts for the nonlinear dependence of evaporation on coverage and temperature, is presented in chapter 5.
- Chapter 6 focuses on presenting the results of the modeling presented in chapters 3-5.

## Chapter 3

### Modeling Cesium Flow from the Reservoir to the Surface

During operation of the CPD, cesium will diffuse out from the reservoir, through the pores and onto the surface; this is shown schematically in Fig 3.1. As shown in Fig 3.1, there will be a cesium coverage  $\Theta_{pore}$  maintained at the pore boundaries on the surface. This chapter is focused on presenting the model to determine  $\Theta_{pore}$  in Eq (2.1). This boundary condition, when combined with diffusion and evaporation in Eq (2.1), will model the cesium coverage profile and QE across the surface of the CPD during operation. At the surface,  $\Theta_{pore}$  is maintained by 1) total cesium flux onto the surface from within the pore, 2) diffusion of cesium along the pore walls onto the cathode surface, and 3) evaporation of cesium off of the surface, schematically shown in Fig 3.1.

This chapter is organized as follows: The first section introduces the main equation used to model the flow of cesium along the walls of the pore from the CPD reservoir to the surface. The equation combines Knudsen Flow, diffusion and evaporation to model the coverage of cesium maintained down the length of the pore walls at equilibrium. This yields the correct boundary condition  $\Theta_{pore}$  used to model the CPD surface. The next section give a more detailed derivation of the Knudsen Flow flux equations [5, 6, 7, 8]. The last two sections discuss the assumptions of the model as well as summarize the main points of the chapter.

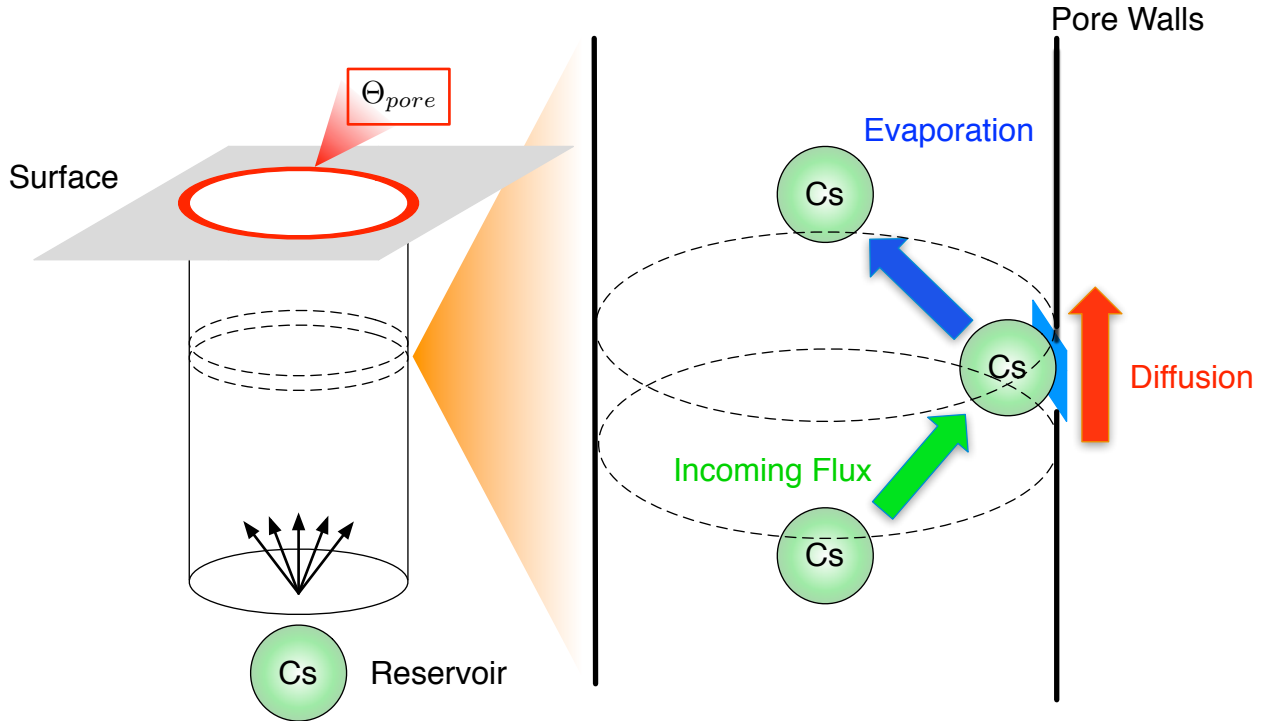


Figure 3.1: Diagrammatic overview of modeling the cesium resupply rate to the surface

### 3.1 Modeling $\Theta_{pore}$

Let each pore be approximated as cylinder<sup>1</sup>. Fig 3.1 gives a schematic diagram of  $\Theta_{pore}$  as well as the three physical processes that occur inside the walls of each pore: 1) the cesium flux onto the walls, 2) diffusion, and 3) evaporation off the pore walls. From symmetry, there should be no azimuthal angular dependence for the cesium density along the walls. Let  $\rho$  be the cesium density along the wall a distance

<sup>1</sup>Though from Fig 1.4 of the actual sintered wire CPD surface, the pores are actually triangular in shape, it will later be shown that the difference between assuming a cylindrical pore versus a triangular pore is negligible

$z$  down the pore, then the equation that models  $\rho$  and  $\Theta_{pore}$  is given by:

$$\frac{\partial \rho}{\partial t} = D \frac{\partial^2 \rho}{\partial z^2} + \frac{P_z}{\sqrt{2\pi m k_B T}} + J_z^w - F_{evap}^z \quad (3.1)$$

$$\rho(0) = \rho_0, \quad \rho(L) = \Theta_{pore}$$

In Eq (3.1),  $D$  is the diffusivity of cesium on tungsten, which will be further discussed in Chapter 4. The incoming flux of cesium atoms due to the background cesium vapor pressure at  $z$ , given by:  $P_z/\sqrt{2\pi m k_B T}$  [29], where  $m$  is the mass of cesium,  $k_B$  is the Boltzmann constant and  $T$  is temperature<sup>2</sup>.  $J_z^w$  is the flux onto the pore wall at  $z$  due to contributions from cesium evaporation throughout the entire length of the pore [57], and  $F_{evap}^z$  is the cesium evaporation rate at location  $z$ . The expression for  $J_z^w$  will be derived in the next section. The model for the cesium evaporation rate  $F_{evap}^z$  is presented in Chapter 5.

In Eq (3.1), the boundary condition at the reservoir,  $z = 0$ , is set to be  $\rho_0$ .  $\rho_0$  is the equilibrium coverage maintained by the tungsten surface in the presence of cesium vapor in the reservoir with pressure  $P_0$ . The other boundary condition at  $z = L$  is  $\Theta_{pore}$ . This connects Eq (3.1), which models cesium migration up the pores from the reservoir, to Eq (2.1) which models the cesium across the surface. Recall from Eq (2.1) that  $\Theta_{pore}$  is the coverage maintained at the pore edges on the surface.

The value of  $\Theta_{pore}$  is not fixed, but is determined by the cesium migration through the pore as well as across the surface. Therefore, Eq (2.1) and Eq (3.1) work together to determine the coverage at the pore boundaries,  $\Theta_{pore}$ . In order to

---

<sup>2</sup>In SI units,  $k_B = 1.381 \times 10^{-23} \text{m}^2 \text{kg}^{-1} \text{K}^{-1}$  and the mass of a cesium atom  $m = 132.9$  amu

step the equations forwards in time, the following relationship is needed:

$$\rho(L) = \Theta(\Omega) \quad (3.2)$$

where  $\Omega$ , the pore boundaries at the surface, was defined previously in Eq (2.1).

With Eq (3.2), the model can be stepped forwards in time as follows: for a given initial  $\Theta$  across the surface, Eq (2.1) is numerically stepped forwards in time to yield  $\Theta$  for the next time step. From  $\Theta$ , the value of  $\Theta(\Omega)$  is obtained. The new value of  $\Theta(\Omega)$  is then inputted as the boundary condition  $\rho(L)$  for Eq (3.1). Eq (3.1) can then be stepped forwards in time to yield a new value of  $\rho(L)$ , or  $\Theta_{pore}$ . At  $\rho(L)$ , the value of the surface coverage at  $\Theta(\Omega + \delta z)$  will be used as the upwind point to calculate the numerical second derivative in Eq (3.1). The new value of  $\Theta_{pore}$  is then inputted into Eq (2.1) and the process is repeated.

To numerically solve Eq (3.1), an implicit discretization in time was used.

Discretizing Eq (3.1) yields:

$$\begin{aligned} \frac{\rho_{n+1,j} - \rho_{n,j}}{\delta t} = & D \frac{1}{2} \left[ \left( \frac{\partial^2 \rho}{\partial z^2} \right)_{n+1,j} + \left( \frac{\partial^2 \rho}{\partial z^2} \right)_{n,j} \right] + \frac{P_z}{\sqrt{2\pi m k_B T}} \\ & + \frac{1}{2} \left[ (J_z^w - F_{evap}^z)_{n+1,j} + (J_z^w - F_{evap}^z)_{n,j} \right] \end{aligned} \quad (3.3)$$

$$\rho(0) = \rho_0, \quad \rho(L) = \Theta_{pore}$$

where the “ $n$ ” index represents the time discretization and “ $j$ ” represents the spatial discretization. The pressure profile  $P_z$  down the length of the pore is assumed to not change over time. A solution for  $\rho$  at each time step is obtained by implicitly using the average value of  $\rho$  for the  $n$ th and  $n + 1$  time step. Eq (3.3) produces a system of  $N$  nonlinear equations<sup>3</sup> ( $N$  is the number of grid points used) where

---

<sup>3</sup>the equations are nonlinear because the evaporation rate  $F_{evap}^z$  and flux term  $J_z^w$  both have a

the coverage  $\rho$  for the next time step  $n + 1$  is obtained by solving the system. The second derivatives are evaluated using a second order central differencing method, given by:

$$\left(\frac{\partial^2 \rho}{\partial z^2}\right)_{n,j} = \frac{\rho_{n,j-1} - 2\rho_{n,j} + \rho_{n,j+1}}{\delta z^2} + O(\delta z^2) \quad (3.4)$$

where  $\delta z$  is the spatial discretization of the pore length.

The time step  $\delta t$  was chosen to be the smaller one of either the characteristic time of diffusion ( $\delta t_{diff}$ ), or of evaporation ( $\delta t_{evap}$ ). The two are given by:

$$\begin{aligned} \delta t_{diff} &= \frac{\delta z^2}{D} \\ \delta t_{evap} &= \frac{\rho_0}{F_{evap}^z} \end{aligned} \quad (3.5)$$

where the characteristic evaporation time  $\delta t_{evap}$  was calculated assuming that  $\rho_0$  is 1% of a full monolayer of cesium in atoms per area (since  $F_{evap}^z$  is in atoms per area per second). Choosing  $\rho_0$  to be only 1% of a full monolayer ensures that  $\delta t_{evap}$  would not be too large and that the  $\delta t$  at each time step will be chosen small enough to allow proper convergence.

In order to test convergence, the model was run using two cases. The first case used a discretization that spatially divided the pore length from 0 to L using one thousand grid spacings. The second assumed a much coarser discretization and only used one hundred grid spacings for the same pore length. The results obtained for the two cases match very closely for large times, so convergence to a unique solution is shown.

---

nonlinear dependence on the cesium coverage  $\rho$ .

### 3.2 Flux Due to Pore Walls $J_z^w$

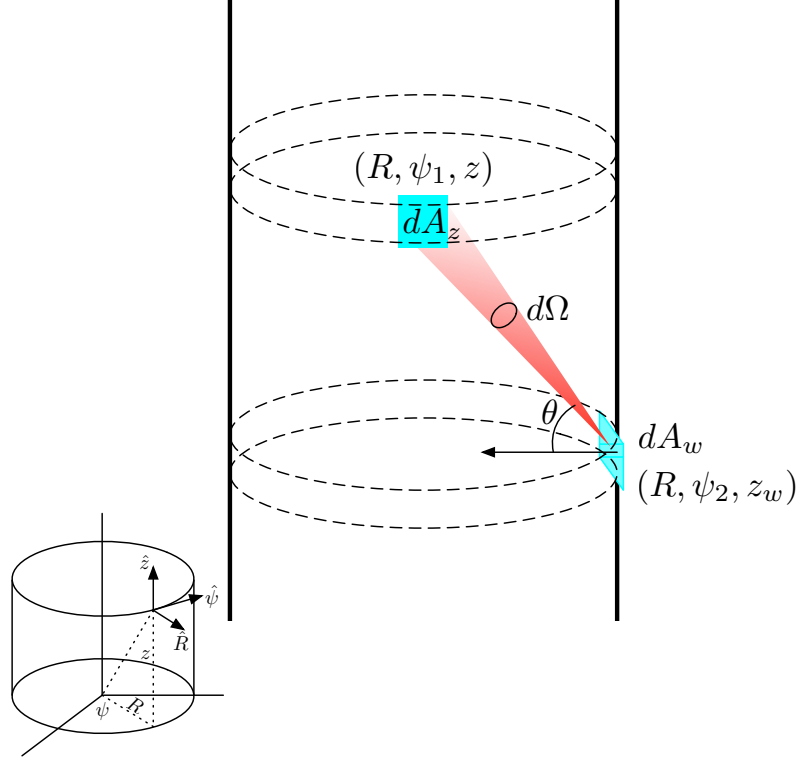


Figure 3.2: Schematic diagram of flux onto the differential wall element  $dA_z$  due to evaporation from  $dA_w$

This section derives the expression for  $J_z^w$ , the net flux of cesium down the pore due to evaporation off the walls in Eq (3.1). Figure ?? gives a schematic representation of the flux onto the differential area element  $dA_z$ , a distance  $z$  down the pore, due to evaporation from  $dA_w$ . Let  $J$  be the flux onto  $dA_z$  due to evaporation from  $dA_w$ .  $J$  can then be written as:

$$JdA_z = F_{evap}f(\theta)d\Omega dA_w \quad (3.6)$$

where  $d\Omega$  is the solid angle subtended by  $dA_z$  from  $dA_w$ .  $F_{evap}f(\theta)$  is the total

evaporation flux off of  $dA_w$  multiplied by a distribution function  $f(\theta)$ , with  $\theta$  being the angle measured from the normal. The total flux onto  $dA_z$  can be obtained by integrating Eq (3.6) over the entire tube. To set up the integration, it is convenient to work in cylindrical coordinates. From Fig ??, let the location of  $dA_z$  and  $dA_w$  be given by  $\vec{r}_z$  and  $\vec{r}_w$  respectively:

$$\vec{r}_z = R \cos \psi_1 \hat{\mathbf{x}} + R \sin \psi_1 \hat{\mathbf{y}} + z \hat{\mathbf{z}} \quad (3.7)$$

$$\vec{r}_w = R \cos \psi_2 \hat{\mathbf{x}} + R \sin \psi_2 \hat{\mathbf{y}} + z_w \hat{\mathbf{z}}$$

The density of cesium within the tube is low enough such that the mean free path of the cesium gas is much much longer than the tube diameter, hence that cesium-cesium collisions may be safely ignored. Assuming that cesium atoms travel in straight line trajectories upon evaporation off  $dA_w$  towards  $dA_z$ , their trajectory is given by:

$$\vec{l} = (R \cos \psi_1 - R \cos \psi_2) \hat{\mathbf{x}} + (R \sin \psi_1 - R \sin \psi_2) \hat{\mathbf{y}} + (z - z_w) \hat{\mathbf{z}} \quad (3.8)$$

With  $\vec{l}$  determined, the solid angle  $d\Omega$  subtended by the area  $dA_z$  in Fig ?? can be expressed as:

$$d\Omega = \frac{\hat{l} \cdot d\vec{A}_z}{l^2} \quad (3.9)$$

The vector  $d\vec{A}_z$  and  $d\vec{A}_w$  is always normal to the surface. From Fig ??,  $d\vec{A}_z$  and  $d\vec{A}_w$  in cylindrical coordinates are given by:

$$d\vec{A}_z = -R d\psi_1 dz_z \hat{\mathbf{r}} \quad (3.10)$$

$$d\vec{A}_w = -R d\psi_2 dz_w \hat{\mathbf{r}}$$

It will be assumed that the cesium atoms evaporating off the walls follow a  $\cos \theta$  distribution, where  $\theta$  is the angle to the normal. This approximation is well used in the Knudsen flow analysis [45]. With this assumption,  $f(\theta)$  in Eq (3.6) is given by:

$$f(\theta) = \frac{\cos \theta}{\pi} \equiv \frac{-\hat{l} \cdot \hat{r}}{\pi} \quad (3.11)$$

Combining Eq (3.7)–Eq (3.11), Eq (3.6) can be integrated over  $dA_w$  to give an expression for the total flux onto  $dA_z$  from the entire length of the pore:

$$J_z^w = \int_0^L \int_0^{2\pi} \frac{F_{evap} \cdot (R - R \cos \psi)^2}{\pi [2R^2 + (z - z_w)^2 - 2R^2 \cos \psi]^2} R d\psi dz_w \quad (3.12)$$

where the following substitution was made for the angular integration:

$$\psi \equiv \psi_1 - \psi_2 \quad (3.13)$$

Upon performing the angular integration over  $2\pi$ , the expression given previously for  $J_z^w$  by Eqs (3.15) – (3.16) is reproduced:

$$J_z^w = \int_0^L \frac{F_{evap}^{z_w}}{2R} \left[ 1 - \frac{\frac{|z-z_w|}{\sqrt{2R}} \left( 3 + \left( \frac{z-z_w}{\sqrt{2R}} \right)^2 \right)}{\left( 2 + \left( \frac{z-z_w}{\sqrt{2R}} \right)^2 \right)^{3/2}} \right] dz_w \quad (3.14)$$

The final expression for  $J_z^w$  can be written as:

$$J_z^w = \int_{(z-L)/\sqrt{2R}}^{z/\sqrt{2R}} \frac{\sqrt{2}F_{evap}^u}{2} \left( 1 - \frac{u(3 + u^2)}{(2 + u^2)^{3/2}} \right) du \quad (3.15)$$

The following substitution was made for the integration variable  $z_w$  in Eq (3.14) over the entire pore from 0 to  $L$ :

$$u \equiv \frac{|z - z_w|}{\sqrt{2R}} \quad (3.16)$$

where  $R$  is the radius of the pore, and  $F_{evap}^u$  is the cesium evaporation rate at  $u$ .

To evaluate Eq (3.15), the evaporation flux  $F_{evap}^{z_w}$  down the length of the pore must be known. For the CPD in question,  $F_{evap}^{z_w}$  is simply the evaporation rate of cesium off of tungsten, which will be discussed and modeled in detail in Chapter 5. Suffice it to say for now that  $F_{evap}^{z_w}$  at location  $z_w$  has a nonlinear dependence on the temperature and coverage of cesium at  $z_w$ .

Before going on however, it is useful for completeness to examine the behavior of Eq (3.15) to see if it is indeed consistent. The first thing to verify is whether or not Eq (3.15) converges to the correct limits for the case where the length of the pore goes to infinity. For an infinitely long pore with uniform coverage, the flux onto the pore wall at any point must equal the evaporation off the wall. For the limit which  $L \rightarrow \infty$ , it can be shown that:

$$\lim_{L \rightarrow \infty} \int_0^L \frac{1}{2R} \left[ 1 - \frac{\frac{z_w}{\sqrt{2R}} \left( 3 + \left( \frac{z_w}{\sqrt{2R}} \right)^2 \right)}{\left( 2 + \left( \frac{z_w}{\sqrt{2R}} \right)^2 \right)^{3/2}} \right] dz_w = \frac{1}{2} \quad (3.17)$$

For an infinitely long pore with uniform coverage, the evaporation flux  $F_{evap}$  should be equal to the flux onto the wall  $J_z^w$ . With uniform coverage,  $F_{evap}$  is constant throughout the entire pore and the following result follows from Eq (3.17):

$$J_z^w = \int_{-\infty}^{\infty} \frac{F_{evap}}{2R} \left[ 1 - \frac{\frac{|z-z_w|}{\sqrt{2R}} \left( 3 + \left( \frac{z-z_w}{\sqrt{2R}} \right)^2 \right)}{\left( 2 + \left( \frac{z-z_w}{\sqrt{2R}} \right)^2 \right)^{3/2}} \right] dz_w = F_{evap} \quad (3.18)$$

### 3.3 Assumptions of the model

In applying Eq (3.1) to calculate the cesium resupply rate to the surface, the pressure profile through the pore  $P_z$  needs to be known. In theory, this can be calculated from first principles but it is not entirely obvious how it can be done. Because

of the lack of data as well as theory to determine  $P_z$ , the model simply assumes the simplest possible pressure profile that yields the correct boundary values. At the surface of the cathode or where  $z = L$ , the pressure is assumed to be close to zero since its vacuum. At the reservoir end of the pore or  $z = 0$ , the pressure is assumed to be simply the partial vapor pressure of cesium within the reservoir  $P_0$ . The pressure profile throughout the pore assuming that the reservoir maintains a partial cesium vapor pressure of  $P_0$  is taken to be:

$$P_z = P_0 \left(1 - \frac{z}{L}\right) \quad (3.19)$$

This pressure profile is the usual approximation used in the Knudsen analysis [5, 6, 7].

The second assumption made by the model was that the mean free path of cesium atoms is greater than or on the same order as the characteristic size of the pores, such that cesium-cesium collisions can be ignored. This assumption can be verified by treating the cesium in the reservoir as an ideal gas, and using the equation for the mean free path given by:

$$l = \frac{k_B T}{\pi \sqrt{2} d^2 P_0} \quad (3.20)$$

where  $k_B$  is Boltzmann's constant,  $T$  is temperature,  $d$  is the diameter of the cesium atom, and  $P_0$  is the pressure of cesium in the reservoir. Assuming that the pressure of cesium in the reservoir is equal to the vapor pressure of cesium over bulk cesium, then the mean free path for a temperature range from  $400K - 700K$  is about  $0.02 - 1.8 \times 10^{-6}$  meters. This is greater than or equal to the radius of the pores, which

is only on the order of several microns. Therefore, the assumption about the mean free path for the temperatures of interest holds.

### 3.4 Modeling CPD Lifetime

Apart from the model for  $\Theta_{pore}$  and cesium migration down the walls (Eq (3.1)), the total cesium flux through each pore can be modeled. This section outlines the model for the total cesium flux passing through a pore with given cross sectional area. This model is the same model used in the Knudsen flow literature [5, 6, 7]. Various pore cross-sectional geometries are considered and compared with the cylindrical pore approximation assumed for modeling the CPD. It will be shown that the difference between assuming a cylindrical pore versus a triangular pore is small.

Figure 3.3 gives a schematic representation of the flux passing through a differential cross section  $\mathbf{dA}$  due to evaporation from  $\mathbf{dS}$ . Let  $J$  be the flux passing through  $\mathbf{dA}$  due to evaporation from  $\mathbf{dS}$ .  $J$  can then be written as:

$$J\mathbf{dA} = F^w f(\theta)\mathbf{d}\Omega\mathbf{dS} \quad (3.21)$$

where  $F^w$  is the flux coming off of  $\mathbf{dS}$ ,  $f(\theta)$  is the distribution function given by Eq (3.11), and  $\mathbf{d}\Omega$  is the solid angle subtended by  $\mathbf{dA}$  from  $\mathbf{dS}$ . From Fig 3.3, the expressions for  $f(\theta)$ ,  $\mathbf{d}\Omega$ ,  $\mathbf{dA}$  and  $\mathbf{dS}$  can be written in terms of the variables  $r$ ,  $l$ ,  $w$ , and  $\psi$  from purely geometrical arguments alone. From Fig 3.3, the expression for  $f(\theta)$  is given by:

$$f(\theta) = \frac{\cos\theta}{\pi} = \frac{r \cos\psi}{\pi l} \quad (3.22)$$

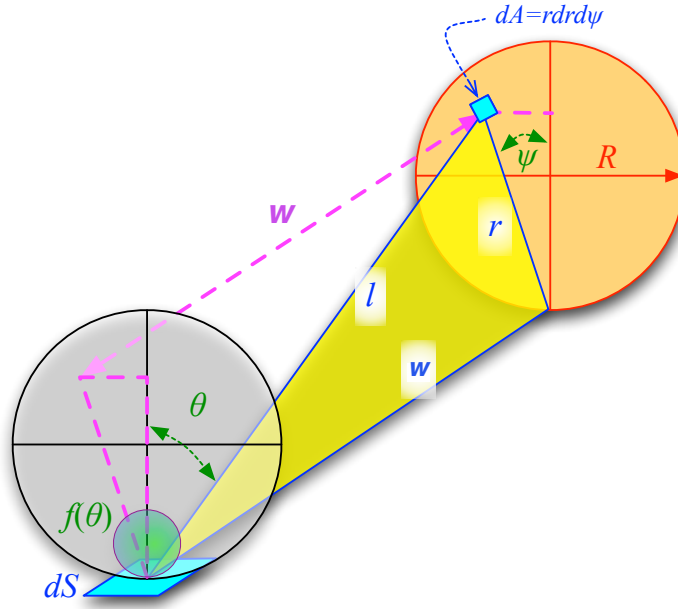


Figure 3.3: Schematic diagram of flux through the differential area element  $\mathbf{dA}$  due to evaporation from  $\mathbf{dS}$

The expression for the differential solid angle  $\mathbf{d}\Omega$  can be obtained by writing the area vector for  $\mathbf{d}\vec{A}$  as  $rdrd\psi\hat{\mathbf{n}}$  and convincing oneself that  $\hat{\mathbf{l}} \cdot \hat{\mathbf{n}} = w/l$ . The expression for  $\mathbf{d}\Omega$  is then given as:

$$\mathbf{d}\Omega = \frac{\hat{\mathbf{l}} \cdot \hat{\mathbf{n}}}{l^2} r dr d\psi = \frac{w r dr d\psi}{l^3} \quad (3.23)$$

The last piece of Eq (3.21),  $\mathbf{dS}$ , is simply the differential wall element and from Fig 3.3, can be written as:

$$\mathbf{dS} = 2\pi R \mathbf{d}w \quad (3.24)$$

Let  $Q$  be the total number of cesium atoms per unit time passing through the cross sectional area  $A$ .  $Q$  can be calculated by integrating Eq (3.21) throughout the entire pore. Inserting the expressions for  $f(\theta)$ ,  $\mathbf{d}\Omega$ ,  $\mathbf{dA}$  and  $\mathbf{dS}$  given by equations

Eq (3.22) - Eq (3.24),  $Q$  can be calculated from the following expression:

$$Q = \int_0^{2R \cos \psi} r^2 \mathbf{d}r \int_{-\pi/2}^{\pi/2} \cos \psi \mathbf{d}\psi \int_0^L \frac{w F^w}{\pi l^4} 2\pi R \mathbf{d}w \quad (3.25)$$

where the limits of integration over  $\mathbf{d}r$  goes from 0 to  $2R \cos \psi$ , which is the upper limit describing the edge of the circle bounding the area  $A$ . To get  $F^w$ , the theory continues to assume from Eq (3.19) that the pressure profile down the pore is linear, with the partial cesium vapor pressure at the reservoir to be  $P_0$  and the pressure at the CPD surface to be vacuum. The flux off the pore walls  $F^w$  is given by:

$$F^w = \frac{P_0 w}{L \sqrt{2\pi m k_B T}} \quad (3.26)$$

where the length parameter  $w$  is has boundary conditions such that  $w = 0$  is the surface side of the pore and  $w = L$  is the reservoir side. Inserting Eq (3.26) into Eq (3.25) and assuming that  $L/R \gg 1$ , integrating out the integral over  $\mathbf{d}w$  yields the following:

$$Q = \frac{P_0 2\pi R}{4L \sqrt{2\pi m k_B T}} \int_0^{2R \cos \psi} r \mathbf{d}r \int_{-\pi/2}^{\pi/2} \cos \psi \mathbf{d}\psi \quad (3.27)$$

It is useful when comparing to other pore cross-sectional geometries to rewrite Eq (3.27) in terms of a dimensionless tube cross section geometry factor  $W$ , given by [52]:

$$Q = \frac{P_0}{4\sqrt{2\pi m k_B T}} AW \quad (3.28)$$

where  $A$  is the cross sectional area of the pore tube and  $W$  is defined as:

$$W \equiv \frac{P_A}{L} \langle \cos \psi \rangle_A \quad (3.29)$$

Here,  $P_A$  is the perimeter of the cross sectional area  $A$  and  $\langle \cos \psi \rangle_A$  is an averaged value independent of pore area and depends only on shape. The expression for

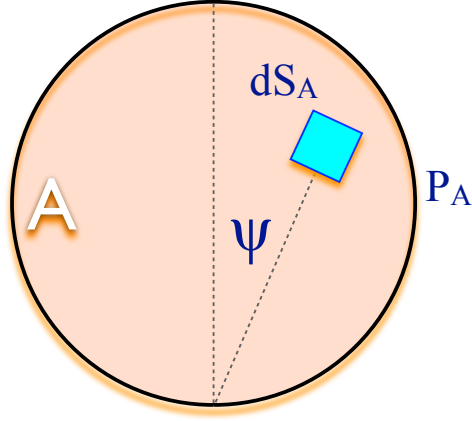


Figure 3.4: Circular cross section where the shape factor  $\langle \cos \psi \rangle_A$  is independent with respect to location around the perimeter

$\langle \cos \psi \rangle_A$  is given below [52]:

$$\langle \cos \psi \rangle_A = \frac{1}{A} \int \int_A \cos \psi \, dA \quad (3.30)$$

Observe that  $\langle \cos \psi \rangle_A$  is an average value of a dimensionless quantity – it is a pure number  $\leq 1$  because  $\cos \psi \leq 1$ . So the shape of the tube only factors into the total flux  $Q$  by appending it with a coefficient of order unity.

### 3.4.1 Comparison between Circular and Noncircular Pores

From Eq (3.28), it becomes straightforward to make comparisons of how the total cesium flow through the pores will differ between various pore geometries. Specifically, the value of  $\langle \cos \psi \rangle_A$  in Eq (3.30) will change for different shape pores. For a cylindrical pore cross sections, the value of  $\langle \cos \psi \rangle_A$  is the same for all locations around the area  $A$ . This is simply a result of azimuthal symmetry as shown in Fig

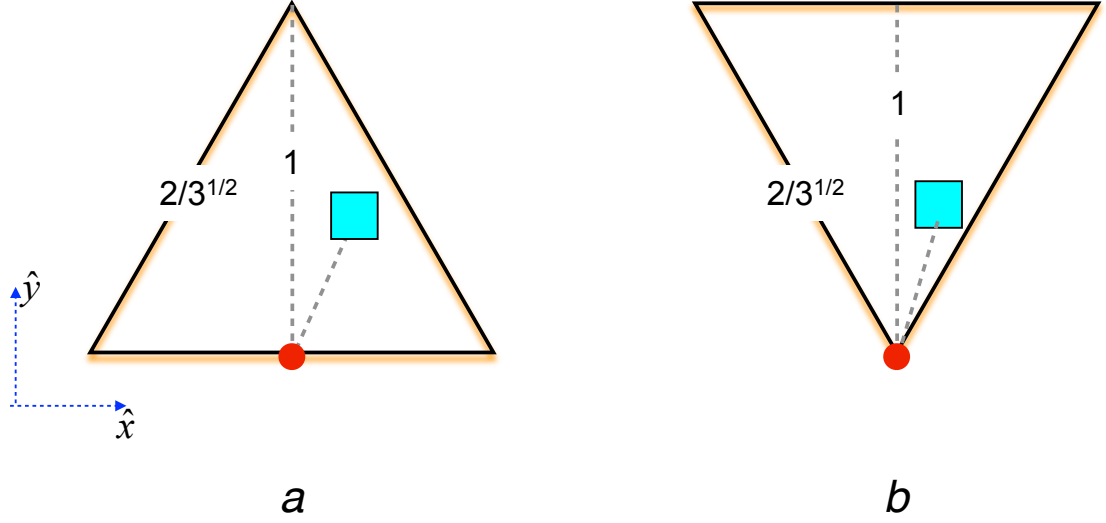


Figure 3.5: The shape factor  $\langle \cos \psi \rangle_A$  for a triangular pore is dependent with respect to location but is bounded by the two cases shown above.

3.4.  $\langle \cos \psi \rangle_A$  calculated for the cylindrical pore is [52]:

$$\langle \cos \psi \rangle_A = \frac{\int_0^{2R \cos \psi} r \mathbf{d}r \int_{-\pi/2}^{\pi/2} \cos \psi \mathbf{d}\psi}{\int_0^{2R \cos \psi} r \mathbf{d}r \int_{-\pi/2}^{\pi/2} \mathbf{d}\psi} = \frac{8}{3\pi} \approx 0.8488 \quad (3.31)$$

For non azimuthally-symmetric cases such as a triangular pore with all sides the same length, the value of  $\langle \cos \psi \rangle_A$  would not be independent of location around the pore area. However, there are two locations for which the integrals giving  $\langle \cos \psi \rangle_A$  can be calculated analytically. These locations are shown in Fig 3.5. For convenience, the height of the triangular areas are set to unity in Fig 3.5. For the first case labeled as  $a$  in Fig 3.5, the integral giving  $\langle \cos \psi \rangle_A$  is given by:

$$\langle \cos \psi \rangle_A = 2\sqrt{3} \int_0^{1/\sqrt{3}} \mathbf{d}x \int_0^{1-\sqrt{3}x} \frac{y \mathbf{d}y}{\sqrt{x^2 + y^2}} \approx 0.721 \quad (3.32)$$

For the second case labeled as  $b$  in Fig 3.5, the integral giving  $\langle \cos \psi \rangle_A$  is given by:

$$\langle \cos \psi \rangle_A = \frac{6\sqrt{3}}{5} \int_0^{1/\sqrt{3}} \mathbf{d}x \int_{x/\sqrt{3}}^1 \frac{y \mathbf{d}y}{\sqrt{x^2 + y^2}} \approx 0.864 \quad (3.33)$$

From a limiting cases arguments, all values of  $\langle \cos \psi \rangle_A$  for the triangular pore must be bounded between Eq (3.32) and Eq (3.33). This gives an average value of about 0.8 for the shape dependent area factor in Eq (3.30). When compared with the cylindrical case, the difference is only about 5%. Therefore, even if the actual sintered wire CPD pores are closer to triangular in shape (Fig 1.4), and even if the pores are non-uniform (where some are more circularly necked during sintering), the error involved in assuming that the pores are cylindrical for modeling purposes is negligible.

### 3.5 Chapter Conclusions

- The cesium resupply rate for a CPD is modeled by setting the value of cesium coverage at the pore boundaries on the surface to be  $\Theta_{pore}$  in Eq (2.1).
- A model for cesium transport along the walls of the pores up to the surface is developed and presented in this chapter to determine the boundary condition  $\Theta_{pore}$  in Eq (2.1).
- The model takes into account the cesium diffusion, evaporation, and flux on the walls of the pore during rejuvenation.
- The model assumes that the cesium vapor pressure varies linearly from the reservoir up to the surface of the CPD photocathode during operation.
- The difference between assuming a cylindrical pore geometry and a triangular pore geometry is small.

## Chapter 4

### Diffusion

This chapter will focus mainly on the numerical methods that are used to model diffusion across the cathode surface. Diffusion is what governs how fast and how smoothly the cesium atoms will spread across the surface as they come up through the source pores. Because the pores on a CPD are arranged in a periodic array, specific methods for solving the diffusion equation unique to the periodic arrangement and geometry of the cathode surface are discussed and derived in this chapter.

The chapter can be divided into the following sections: The first section gives an introduction to Fick's law and shows how to obtain the basic diffusion equation. The second section presents the numerical methods used to model Eq (2.1) on a hexagonal grid mesh. The motivation and advantages for modeling on a hexagonal grid are also discussed. The third section gives a brief summary of some experimental studies done in literature for obtaining the diffusivity of cesium on tungsten. The final section summarizes the main points of the chapter.

#### 4.1 Fick's Law and the Diffusion Equation

On a macroscopic scale, the granular structure produced by single atoms gets averaged out and the density of material present in any space can be approximated

by a smoothly varying function. Fick's Law is an equation that relates the flux of the material passing through a boundary to its density. Fick's law is based on the empirical observation that material will spread from high concentration to low concentration. Mathematically, it simply states that the flux is proportional to the negative gradient of the density at that point. If  $\vec{J}$  is the flux,  $\Theta$  is the density of material, and  $D$  is the proportionality factor, Fick's Law can be written as:

$$\vec{J} = -D\vec{\nabla}\Theta \quad (4.1)$$

Fick's law by itself cannot fully describe a given system since there are two unknowns,  $\vec{J}$  and  $\Theta$ , and only one equation. A second equation relating the flux  $\vec{J}$  and density  $\Theta$  is required to fully solve the system. This second equation comes from conservation of matter, or the continuity equation. In order for matter to be conserved, the change in the density at any given point is equal to the net amount entering or leaving from that point. The net amount entering or leaving a given region is simply the divergence of the flux. Assuming that no material is created or destroyed at any given instance or location, the continuity equation is given by:

$$\frac{\partial\Theta}{\partial t} + \vec{\nabla} \cdot \vec{J} = 0 \quad (4.2)$$

Combining Eq (4.1) and (4.2) by substituting for the flux  $\vec{J}$ , the standard diffusion equation is given by [29]:

$$\frac{\partial\Theta}{\partial t} = \vec{\nabla} \cdot (D\vec{\nabla}\Theta) \quad (4.3)$$

With appropriate boundary conditions, the diffusion equation describes how an initial given density of material spreads or evolves over time.

For modeling the surface of a CPD, Eq (2.1) presented in chapter 2 of this dissertation is used. Eq (2.1) is equivalent to the 2-d diffusion equation on a surface with sources and sinks. The source term is provided by the pore boundaries on the surface, and the sink term is the evaporation rate of cesium across the surface. Eq (2.1) can be obtained by adding the cesium evaporation sink term,  $-F_{evap}$ , to Eq (4.2) and doing the same substitution. The source is modeled by setting the boundary conditions at the pores to be  $\Theta_{pore}$ .

## 4.2 Numerical Methods Used for Modeling

Eq (2.1) for modeling the surface of a CPD is rewritten below explicitly for 2 dimensions:

$$\frac{\partial \Theta}{\partial T} = D \left( \frac{\partial^2 \Theta}{\partial X^2} + \frac{\partial^2 \Theta}{\partial Y^2} \right) + \frac{\partial D}{\partial \Theta} \left[ \left( \frac{\partial \Theta}{\partial X} \right)^2 + \left( \frac{\partial \Theta}{\partial Y} \right)^2 \right] - F_{evap} \quad (4.4)$$

$$\Theta(\Omega) = \Theta_{pore}, \quad \Omega \in \text{pore edges}$$

The sintered tungsten wires create a periodic hexagonal array of pores shown in Fig 4.1. Fig 4.1 highlights a region of the cathode that is modeled. From symmetry arguments, the boundary conditions for the highlighted region are assumed to be periodic. Effects from the edge of the cathode surface are ignored. This is valid since the area of the simulated region is orders of magnitude smaller than the entire size of the cathode. For typical CPD cathodes made from 20 micron diameter tungsten wire, the simulated area would be around 800 square microns. This is several orders of magnitude smaller than the area of the entire cathode, usually on the order of millimeters squared.

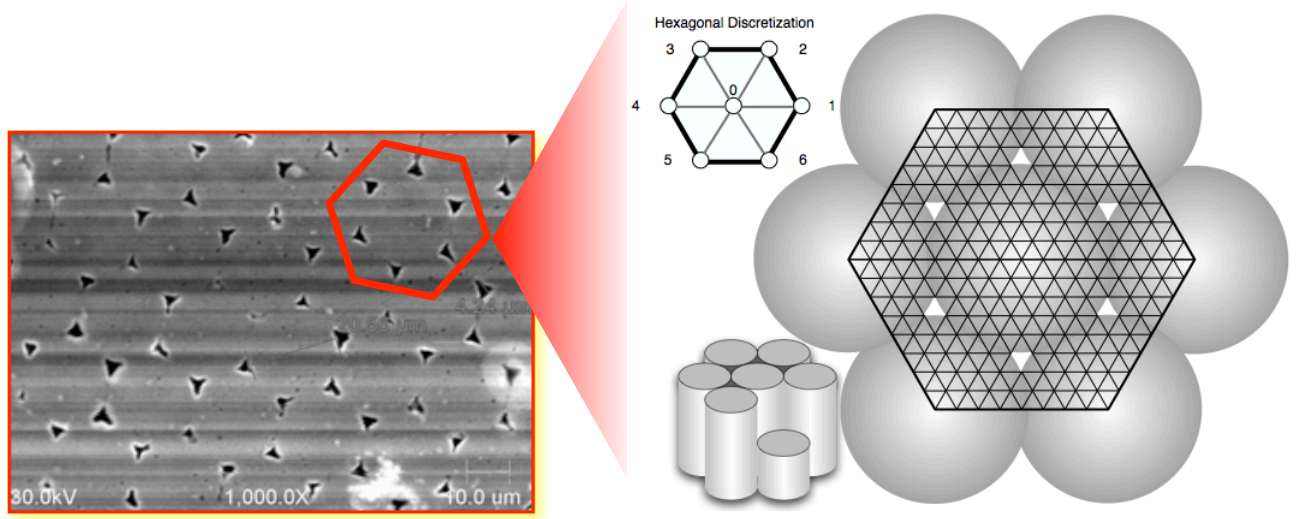


Figure 4.1: SEM image of the sintered wire CPD cathode surface. Highlighted red region represents the region that is modeled assuming periodic boundary conditions.

Equation 4.4 is solved numerically. Because of the geometry of the surface, all the numerics were performed on a hexagonal mesh grid, schematically shown in Fig 4.1. The main advantage in working with a hexagonal mesh is that it allows natural inclusion of the periodic boundary conditions. A hexagonal grid is also more accurate than the traditional rectangular grid for evaluating the discrete Laplacian and differencing operators. It is useful to work with Eq (4.4) in its non-dimensional form when doing the numerics [49]. To do this, the following dimensionless variables

are defined:

$$x \equiv \frac{X}{L} \tag{4.5}$$

$$y \equiv \frac{Y}{L} \tag{4.6}$$

$$\theta \equiv \frac{\Theta}{\Theta_0} \tag{4.7}$$

$$d \equiv \frac{D}{D_0} \tag{4.8}$$

Where  $x$ ,  $y$ ,  $\theta$ , and  $d$  are the dimensionless distances, coverage, and diffusivity respectively. Substituting back in (4.4) and assuming that the diffusivity is independent on coverage yields:

$$\Theta_0 \frac{\partial \theta}{\partial T} = \frac{\Theta_0 D_0 d}{L^2} \left( \frac{\partial^2 \theta}{\partial x^2} + \frac{\partial^2 \theta}{\partial y^2} \right) - F_{evap} \tag{4.9}$$

Rearranging and collecting terms gives the dimensionless version of equation (4.4) to be:

$$\frac{\partial \theta}{\partial t} = d \left( \frac{\partial^2 \theta}{\partial x^2} + \frac{\partial^2 \theta}{\partial y^2} \right) - \frac{L^2}{D_0 \Theta_0} F_{evap} \tag{4.10}$$

It is straightforward to show that the dimensionless time variable  $t$  is:

$$t = \frac{D_0 T}{L^2} \tag{4.11}$$

#### 4.2.1 Discret Laplacian and Gradient Operators on a Hex Lattice

The expressions for the discrete 2D Laplacian and derivative operators on a hexagonal grid lattice are derived in this subsection. Fig 4.2 schematically illustrates the basic stencil for the hexagonal mesh. In a traditional rectangular grid, the center point would be surrounded by neighboring four points. For the hexagonal mesh,

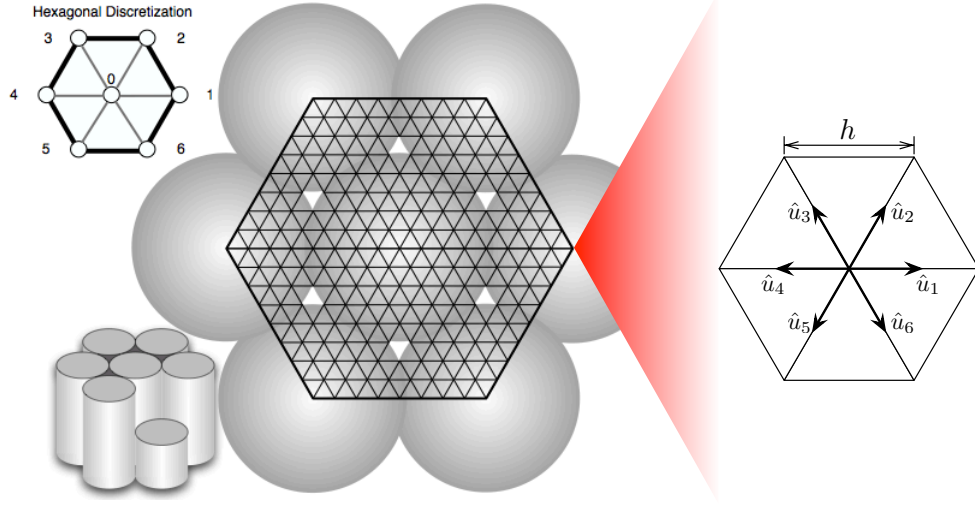


Figure 4.2: Schematic wire stencil of the hexagonal grid showing the discretization parameter  $h$  as well as the points used to evaluate the Laplacian operators.

a center point is surrounded by a six point stencil. The directional unit vectors pointing from the center point to each neighboring point on the hexagonal stencil are given by:

$$\hat{u}_1 = \hat{x} \quad (4.12)$$

$$\hat{u}_2 = \frac{1}{2}\hat{x} + \frac{\sqrt{3}}{2}\hat{y} \quad (4.13)$$

$$\hat{u}_3 = -\frac{1}{2}\hat{x} + \frac{\sqrt{3}}{2}\hat{y} \quad (4.14)$$

$$\hat{u}_4 = -\hat{x} \quad (4.15)$$

$$\hat{u}_5 = -\frac{1}{2}\hat{x} - \frac{\sqrt{3}}{2}\hat{y} \quad (4.16)$$

$$\hat{u}_6 = \frac{1}{2}\hat{x} - \frac{\sqrt{3}}{2}\hat{y} \quad (4.17)$$

From calculus, directional derivatives from the center point to each of the six surrounding points are given by:

$$\theta_{\mathbf{u}} = \vec{\nabla}\theta \cdot \hat{\mathbf{u}}_i \quad (4.18)$$

where  $\theta_{\mathbf{u}}$  represents the partial derivative along the direction  $\hat{\mathbf{u}}_i$ , given by Eqs (4.12)-(4.17). In much the same way, the directional derivatives of the second order can be written as:

$$\theta_{\mathbf{uu}} = \vec{\nabla}\theta_{\mathbf{u}} \cdot \hat{\mathbf{u}}_i \quad (4.19)$$

In order to approximate the Laplacian operator for such a hexagonal mesh grid, it is necessary to use Eqs (4.18) and (4.19) to write out the Taylor series expansions for the value of  $\theta$  at each of the six nearest neighbors. For a given point on the grid located at position  $r_0\hat{\mathbf{r}}$ , the position of each of its six nearest neighbors can be written as  $r_0\hat{\mathbf{r}} + h\hat{\mathbf{u}}_i$ , where  $h$  is the discretization length. The Taylor series expansion up to fourth order about  $r_0\hat{\mathbf{r}}$  for each of the six neighboring points for a given hexagonal stencil is given by:

$$\theta(r_0\hat{\mathbf{r}} + h\hat{\mathbf{u}}_i) - \theta(r_0\hat{\mathbf{r}}) = \theta_{\mathbf{u}}(r_0\hat{\mathbf{r}})h + \frac{h^2}{2}\theta_{\mathbf{uu}}(r_0\hat{\mathbf{r}}) + \frac{h^3}{6}\theta_{\mathbf{uuu}}(r_0\hat{\mathbf{r}}) + O(h^4) \quad (4.20)$$

It can be shown from symmetry as well as explicitly that the following relationships are true for all points on the hexagonal mesh:

$$\sum_{\mathbf{u}} \theta_{\mathbf{u}} = 0 \quad (4.21)$$

$$\sum_{\mathbf{u}} \theta_{\mathbf{uuu}} = 0 \quad (4.22)$$

Where the sums extends over all six directional derivatives. From (4.21) and (4.22), summing up all the Taylor series expansions over all six directions  $\hat{\mathbf{u}}$  about  $r_0\hat{\mathbf{r}}$  yeilds:

$$\left( \sum_{\mathbf{u}} \theta(r_0\hat{\mathbf{r}} + h\hat{\mathbf{u}}_i) \right) - 6\theta(r_0\hat{\mathbf{r}}) = \frac{h^2}{2} \sum_{\mathbf{u}} \theta_{\mathbf{uu}} + O(h^4) \quad (4.23)$$

It can be shown that the following relationship is true:

$$\sum_{\mathbf{u}} \theta_{\mathbf{uu}} = 3(\theta_{xx} + \theta_{yy}) \equiv 3\nabla^2\theta \quad (4.24)$$

Therefore from Eqs (4.23) and (4.24), the approximation to the Laplacian for the hexagonal unit cell to  $O(h^2)$  is given by:

$$\nabla^2\theta = \frac{2}{3h^2} \left( -6\theta(r_0\hat{\mathbf{r}}) + \sum_{\mathbf{u}} \theta(r_0\hat{\mathbf{r}} + h\hat{\mathbf{u}}) \right) + O(h^2) \quad (4.25)$$

## 4.2.2 Discretizing the Nonlinear Diffusion Equation Implicitly in Time

In this subsection, the system of equations that determine the cesium coverage at each time step on the cathode surface is derived. There is one equation for each grid point on the discrete hexagonal lattice. Let the index  $n$  represent the  $n^{\text{th}}$  time step such that:

$$t = n \delta t \quad (4.26)$$

where  $\delta t$  is the discretization of the dimensionless time  $t$  given by Eq (4.11). From Eq (4.10), the following relationship is obtained between the  $n^{\text{th}}$  time step and the  $n + 1$  time step:

$$\begin{aligned} \frac{\theta_{n+1} - \theta_n}{\delta t} = & \frac{d}{2} \left[ \left( \frac{\partial^2\theta}{\partial x^2} + \frac{\partial^2\theta}{\partial y^2} \right)_{n+1} + \left( \frac{\partial^2\theta}{\partial x^2} + \frac{\partial^2\theta}{\partial y^2} \right)_n \right] \\ & - \frac{L^2}{2D_0\Theta_0} [F_{evap}^{n+1} + F_{evap}^n] \end{aligned} \quad (4.27)$$

The Laplacian as well as the evaporation rate  $F_{evap}$  are approximated by averaging their values at the  $n^{\text{th}}$  and  $n + 1$  time step. This is known as the implicit scheme for numerically solving the partial differential equation [49]. Eq (4.27) implicitly assumes knowledge of  $\theta$  for the  $n + 1$  time step. The grid points on the hexagonal lattice are indexed by  $i$ . The index numbering goes from left to right along the diagonals of the hexagonal lattice. Fig 4.3 shows an example of the numbering for

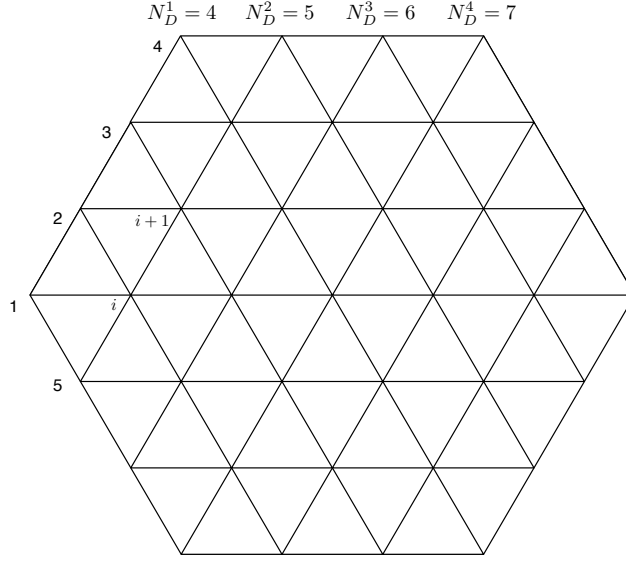


Figure 4.3: The numbering scheme used for the numerical discretization of the hexagonal lattice.  $N_D^j$  are the number of grid points contained in the  $j$ th diagonal.

a small hexagonal lattice grid. As shown in Fig 4.3, let  $N_D^j$  be the number of grid points in the  $j$ th diagonal on the hexagonal grid. The index  $m$ , to be used shortly, will be defined by:

$$m \equiv N_D^j + 1 \quad (4.28)$$

From Eqs (4.25), and (4.27) the coverage at the  $i$ th grid point,  $\theta_i$ , not including the boundaries can be expressed as:

$$\begin{aligned} r(\theta_{i,n+1} - \theta_{i,n}) = & d [(\theta_{i-1} + \theta_{i+1} + \theta_{i-m} + \theta_{i-m+1} + \theta_{i+m} + \theta_{i+m+1} - 6\theta_i)_{n+1} \\ & + (\theta_{i-1} + \theta_{i+1} + \theta_{i-m} + \theta_{i-m+1} + \theta_{i+m} + \theta_{i+m+1} - 6\theta_i)_n] \quad (4.29) \\ & - \frac{3h^2 L^2}{2D_0 \Theta_0} [F_{evap}^{n+1} + F_{evap}^n] \end{aligned}$$

where  $m$  is defined in Eq (4.28) and  $r$  is defined by:

$$r \equiv \frac{3h^2}{\delta t} \quad (4.30)$$

The boundaries of the hexagonal grid have periodic boundary conditions that are reflected in the calculation of the Laplacian. Let the coverage values for all the points on the hex mesh at the  $n^{th}$  time step be contained in the vector  $\vec{\theta}_n$ . A square matrix  $\mathbf{M}$  was created such that the  $i^{th}$  row of the operation  $\mathbf{M} \cdot \vec{\theta}_n$  will be:

$$\left[ \mathbf{M} \cdot \vec{\theta}_n \right]_i = \theta_{i-1} + \theta_{i+1} + \theta_{i-m} + \theta_{i-m+1} + \theta_{i+m} + \theta_{i+m+1} - 6\theta_i \quad (4.31)$$

The above equation will be valid for all indices of  $i$  not corresponding to a boundary point on the hexagonal lattice. At the boundaries, the points used to calculate the Laplacian reflect the periodic boundary conditions of the lattice. The rows of matrix  $\mathbf{M}$  for the boundaries will also be modified accordingly. Finally, the system of equations that give  $\vec{\theta}_{n+1}$  from  $\vec{\theta}_n$  at the previous time step can be written as:

$$(r \cdot \mathbf{I} - d \cdot \mathbf{M}) \cdot \vec{\theta}_{n+1} + \frac{3h^2 L^2}{2D_0 \Theta_0} \vec{F}_{evap}^{n+1} = (r \cdot \mathbf{I} + d \cdot \mathbf{M}) \cdot \vec{\theta}_n - \frac{3h^2 L^2}{2D_0 \Theta_0} \vec{F}_{evap}^n \quad (4.32)$$

where  $\mathbf{I}$  is the identity matrix. The equations are nonlinear because the evaporation term  $F_{evap}$  is nonlinear in coverage. Solutions to this system were numerically found using MATLAB 2011.

### 4.3 Diffusivity Measurements of Cs:W in Literature

The diffusivity  $D$  in Eq (4.3) characterizes how fast a macroscopic coverage of atoms spreads across the surface in units of length squared per unit time. From (4.3), measurement of coverage over position and time will yield a measurement for the diffusivity [2]. On a microscopic scale, the diffusivity  $D$  is related to the rate at which an atom jumps from one surface site to the next as well as the energy barrier

$\Delta E_d$  associated with the jump [15]. From statistical mechanics, the diffusivity has an Arrhenius temperature dependence [47]. The relationship between diffusivity and temperature is given by:

$$D = D_0 e^{\Delta E_d/kT} \quad (4.33)$$

An Arrhenius plot of measured diffusivity  $D$  for various temperatures should yield values for  $D_0$  and  $\Delta E_d$ . In the literature, there have been two well known independent experiments for diffusion of cesium on tungsten.

The first study of diffusion was reported by Langmuir and Taylor in 1932 [26]. For their experiment, a tungsten filament wire was surrounded by a concentric electrode. The electrode was segmented such that a central section was surrounded by guard rings on either side. The central section was electrically insulated from the guard rings. With this setup, Langmuir and Taylor were able to measure the amount of cesium atoms present on the surface of tungsten filament in the central section at any time and temperature by flashing. At temperatures above 1000 K, any cesium on the surface will evaporate as a cesium ion. By measuring the total ion charge accumulated from the center electrode, the amount of cesium atoms previously present on the surface is determined. The experiment proceeded as follows. The tungsten filament was first exposed to a cesium vapor to coat the surface with a uniform coverage of cesium. The center section of the tungsten wire was then cleaned by heating. The result was a uniform coverage of cesium on the guard ring sections of the wire, and no cesium on the central section. This established the initial coverage profile of cesium on the filament. The filament was then maintained at a constant

temperature and diffusion of cesium from the either side of the central section was allowed to take place. Langmuir and Taylor measured the total amount of cesium that flowed into the central region after a given time interval. The measurements were repeated for a series of different times. Comparing to analytic solutions of the diffusion equation given the initial conditions set up by the experiment, Langmuir and Taylor found the diffusivity for cesium on tungsten to be:

$$D = 0.2e^{-14 \times 10^3 / RT} \text{ cm}^2 / \text{sec} \quad (4.34)$$

The second measurement of diffusivity for cesium on tungsten was done by Love and Wiederick [30] using a technique developed by Bosworth [4]. An initial uniform cesium profile was deposited onto the tungsten surface through a mask. Concentration changes, as well as concentration gradients were then measured by sweeping across the surface with a laser beam profile and observing the changes in photocurrent. The spatial resolution of the laser was high enough compared to the dimensions of the cesium profile on the surface. Their measurements for the diffusivity of cesium on tungsten done under ultrahigh vacuum yielded:

$$D = (0.23 \pm 0.1)e^{-13.1 \pm 0.5 \times 10^3 / RT} \text{ cm}^2 / \text{sec} \quad (4.35)$$

This was in good agreement with earlier data taken by Langmuir and Taylor.

There are some fine points that must be mentioned in interpreting these measurements for diffusivity  $D$ . Both Eq (4.34) and (4.35) were measurements of diffusion averaged over a range of coverage values on the surface. It is well known that the diffusivity is a coverage dependent quantity [11]. Furthermore, the measurements of Langmuir and Taylor were done on a polycrystalline tungsten surface,

while the second measurement by Love and Wiederick were done for the W[110] crystal plane. The differences in diffusion rates for various single crystal planes have not been extensively measured.

#### 4.4 Chapter Conclusions

- After the cesium atoms travel from the reservoir to the surface through the pores, they will undergo surface diffusion on the photocathode. A two dimensional diffusion equation is used to model the time evolution of coverage.
- Because of the geometry of the pore arrangements for a CPD dispenser, all diffusion modeling needed to be done on a hexagonal lattice mesh. The hexagonal grid allows for straightforward implementation of the periodic boundary conditions of the surface as well as increased numerical accuracy when compared to using a traditional cartesian mesh.
- Laplacian operators for a hexagonal grid lattice were derived and Eq (4.4) and the model for the surface was discretized implicit in time on the hexagonal grid.
- Values used for the diffusivity  $D$  were based on previously measured values for  $D$  done by Taylor and Langmuir [26] as well as Love and Wiederick [30].

## Chapter 5

### Evaporation of Cesium off Cathode Surfaces

This chapter will analyze and derive the expression used for the evaporation term, first appearing in Eq (2.1) as  $F_{evap}$ , and later on in chapter 3 Eq (3.1). As introduced in chapter 1, CPD photocathodes aim to extend cathode lifetime by replacing the cesium evaporating off the surface with fresh cesium diffusing from controlled source pores on the cathode surface. The size and spacing of the source pores as well as reservoir temperature can be designed such that the cesium resupply, and evaporation will work together to maintain an optimum coverage of cesium at the surface, maximizing the QE and lifetime.

This chapter is focused on presenting the evaporation theory and modeling done in this study. The chapter is organized as follows: the first section gives a brief history on previous evaporation work found in the literature. The second and third sections outlines and derives the evaporation model developed in this study. Finally, limitations of the model as well as future work are discussed.

#### 5.1 Previous Evaporation Studies

Previously, there have been two well known independent experimental studies of cesium evaporation from tungsten at various temperatures and coverages. The first study was done by Joseph A. Becker and reported in his 1926 paper titled

*Thermionic and adsorption characteristics of cesium on tungsten and oxidized tungsten* [3]. The second study was done by Irving Langmuir and John Bradshaw Taylor and reported in their 1933 paper titled *The evaporation of atoms, ions and electrons from cesium films on tungsten* [53]. This section will give an overview of these two studies, as well as further motivate the need for evaporation modeling.

An explanation on the basic approach for measuring the evaporation rate for both Becker and Langmuir will now be summarized. Evaporation is a process that balances out condensation at equilibrium. Both Langmuir and Becker's experiments do not focus on measuring the evaporation rate directly, but rather the fractional coverage  $\theta$  maintained at equilibrium for various filament temperatures. The rate of arrival<sup>1</sup> then gives the cesium evaporation rate for various  $\theta$  and  $T$ .

### 5.1.1 Becker's Experiment

Becker's method for studying evaporation will now be outlined. Becker uses a tungsten wire filament of diameter 0.0076 cm and length 4.5 cm enclosed in an airtight glass tube containing a molybdenum plate. The tube was also connected to a vacuum pump of some type <sup>2</sup>. The filament was heat treated at around 2800 K with the vacuum pump running to get rid of any surface impurities or contaminants. Cesium was then introduced into the system by breaking a capsule (initially filled with cesium vapor) within the glass tube. The tube was sealed off from the vacuum

---

<sup>1</sup>Measuring the rate of arrival, which changes depending on the cesium vapor pressure, will be explained in the next subsection

<sup>2</sup>At the time, the pump was most likely a mercury diffusion vacuum pump

pump before the cesium was released so cesium vapor would be present inside. The vapor pressure of cesium could be raised or lowered by heating or cooling the tube. By either negatively biasing or positively biasing the molybdenum plate, Becker was able to measure either the electron current, or cesium ion current coming from the filament.

At equilibrium for a given vapor pressure, the atomic rate of arrival of cesium atoms onto the tungsten surface exactly balances the evaporation of cesium off the surface. Langmuir and Kingdon in their 1923 paper [25] have shown that at temperatures close to 1000 K°, every cesium atom hitting the surface of tungsten, or oxidized tungsten will not stick but leave as an ion with charge  $e$ . By measuring the ion current from the tungsten filaments at 1040 K and dividing by  $e$  as well as the filament surface area, Becker was able to obtain the number of cesium atoms that strike per  $\text{cm}^2$  per second. Changing the vapor pressure of cesium in the tube will change the rate of arrival of cesium at the surface. The remainder of Becker's experiment is aimed at determining the fractional coverage  $\theta$  that is maintained on the surface at equilibrium. This will yield evaporation data as a function of  $\theta$  and  $T$ .

The coverage  $\theta$  as measured by Becker was done as follows: Upon equilibrium at  $T$ , the tungsten filament is quickly cooled to a temperature of around 600 K. The time it takes for the current to reach a maximum value after cooling is recorded by Becker as  $t_3$ . Becker interprets  $t_3$  as the time it takes for the surface to be covered with a full monolayer after the tungsten is suddenly cooled from  $T$  to 600 K. Becker at the time assumed that maximum electron emission for tungsten occurs when the

surface is covered with a full monolayer of cesium. The assumption made by Becker is that at 600 K, every cesium atom hitting the tungsten surface will stick until maximum electron emission is reached (full monolayer). The coverage  $\theta$  at  $T$  is then given by:

$$\theta = 1 - \frac{t_3}{t_m} \quad (5.1)$$

Where  $t_m$  is the time it takes for a full monolayer of cesium to form on an initially clean surface assuming a sticking coefficient of unity. Becker measured  $t_m$  by cooling the filament quickly from 1040 K directly to 600K and recording the time it takes for the current to reach a maximum value. The vapor pressure of cesium in the tube is the same for both  $t_3$  and  $t_m$  measurements. By changing the vapor pressure different equilibrium points for  $\theta$  and temperature  $T$  can be reached.

### 5.1.2 Langmuir's Evaporation Studies

Langmuir used a different technique than Becker to measure the equilibrium coverage  $\theta$ . The two filament method used by Langmuir will now be described.

In a cylindrical tube, two straight tungsten filament wires, A and B, were mounted parallel to each other. A sketch provided in Langmuir's paper of the experimental setup is shown in Fig 5.1. The cylindrical tube was divided into three sections  $c_0$ ,  $c_1$  and  $c_2$ . In each section, the tube glass was coated with a thin layer of conducting platinum and attached to wires embedded inside the glass. Both electron and ion emission from the filaments could then be collected depending of the biasing of  $c_0$ ,  $c_1$  and  $c_2$  relative to the filament wires. The sections were electrically

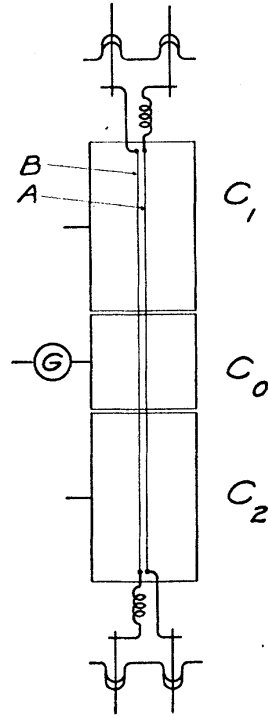


Figure 5.1: Filament and collector arrangement for Langmuir's setup [53].

insulated from each other. The middle section  $c_0$  was attached to a galvanometer that allowed measurements of both ion currents and electrical currents from the the length of the filaments within  $c_0$ . During the course of the experiment, the tube was sealed in vacuum with cesium vapor already present within. The cesium vapor pressure was controlled by changing the temperature of the tube. The temperature was controlled by immersing the whole tube in a large Dewar heat bath containing kerosene vigorously stirred at temperature  $T$ . With this setup, Langmuir was able to measure  $\theta$  at various temperatures and vapor pressures of cesium.

To measure  $\theta$  at equilibrium, filament B was maintained at a high temperature

of around 2400 K, while the temperature of the other filament, filament A, was allowed to accumulate cesium at various temperatures from 300 K to 1000 K until equilibrium was reached. Filament A was then flashed at a high temperature of 1800 K to instantly evaporate all the accumulated cesium atoms. A fraction of the evaporated cesium atoms will hit the hot filament B and be converted into cesium ions. The ion current is measured as a ballistic kick on a galvanometer attached to  $c_0$ . The fractional cesium coverage  $\theta$  of filament A at temperature T can then be calculated from the equation:

$$\theta = \frac{Q}{S_A e f \sigma_{A1}} \quad (5.2)$$

where  $Q$  is the total charge due to the cesium ions measured by the galvanometer,  $f$  is the fraction of cesium atoms intercepted by filament B and converted into cesium ions,  $S_A$  is the surface area of the section of filament A in  $c_0$ ,  $e$  the electronic charge, and  $\sigma_{A1}$  is the number of cesium atoms per  $\text{cm}^2$  for a full monolayer.

### 5.1.3 Discussion and Summary of Previous Studies

A major source of error in Becker's experiment was that Becker had assumed that maximum electron emission from tungsten occurred at a full monolayer coverage of cesium. It is now well known that optimum emission occurs for  $\theta_{opt}$  of 0.67 [16] [22]. Becker measures  $t_3$  and  $t_m$  as the time it takes the electron emission to reach an optimum value, which Becker incorrectly assumes to occur at  $\theta_{opt}$  equal to 1. Furthermore,  $t_3$  and  $t_m$  were measured at 600 K under the assumption that every atom hitting the surface sticks until maximum emission. This assumption at the time

was not yet proven and there has been evidence in Langmuir’s study that indicates evaporation does occur before  $\theta_{opt}$  at these temperatures. This will increase the values measured for  $t_3$  and  $t_m$  as well as skew the data towards higher coverage values than actually present at a given temperature and introduce error in Eq (5.1).

Langmuir’s experiment on the other hand measures the coverage  $\theta$  directly by measuring deflections on the galvanometer and thus  $Q$ , the total cesium ion current as outlined in the previous section.

Langmuir’s data will be used for the remainder of the chapter to compare with the theory developed in this study. In both Langmuir and Becker’s study, a theory for evaporation was not present. At best, the data is fitted to a function with adjustable parameters. The following sections present a simplified theory of evaporation that captures the main features of Langmuir’s data and also tie into the rest of this dissertation to model and predict the performance of CPD photocathodes.

## 5.2 Overview of the Evaporation Model

This section introduces and derives the model developed to describe the evaporation of cesium atoms off single crystal face metal surfaces. A simple model was sought after to predict the evaporation off the surface at a given temperature and partial monolayer coverage of cesium.

From an atomic scale, one can view a single crystal face solid surface as a periodic two dimensional Bravais lattice formed by the atoms of the material. Specific sites able to accommodate an adsorbed atom such as cesium are then present on the

surface of the crystal lattice. Cesium atoms will occupy these well defined adsorption sites at the surface. This has been shown from low energy electron diffraction studies [48]. At each adsorption site, a cesium atom is held to the surface by a binding potential, characteristic of the surface and the various types of interactions present [27].

A bound cesium atom at an adsorption site will have a number of discrete bound energy states available for it to occupy. Assuming the cesium atoms are in thermal equilibrium with the rest of the solid lattice, the probability of finding a cesium atom at a particular energy state  $E$  is given by the Boltzmann distribution  $e^{-E/kT}$ , ignoring normalization. At any instant in time, let  $P$  be the probability that a given cesium atom at the surface will have enough energy to overcome the binding potential and evaporate.  $P$  is then given by:

$$P = \frac{\sum_{free} e^{-E/kT}}{\sum_{i=0}^n e^{-E_i/kT} + \sum_{free} e^{-E/kT}} \quad (5.3)$$

where the numerator sums over all the free energy states  $E$  and the normalization factor in the denominator sums over all the bound states  $E_i$  as well as the free states. The evaporation rate is a product of the frequency at which the Cs atom oscillates, the probability that it has sufficient energy to overcome the binding potential, and the local surface density of atoms. Evaporation per unit area per unit time is then given by:

$$E_{evap} = \frac{1}{\tau} P \sigma \theta \quad (5.4)$$

where  $\tau$  is the characteristic evaporation time,  $\sigma$  is the number density per unit area

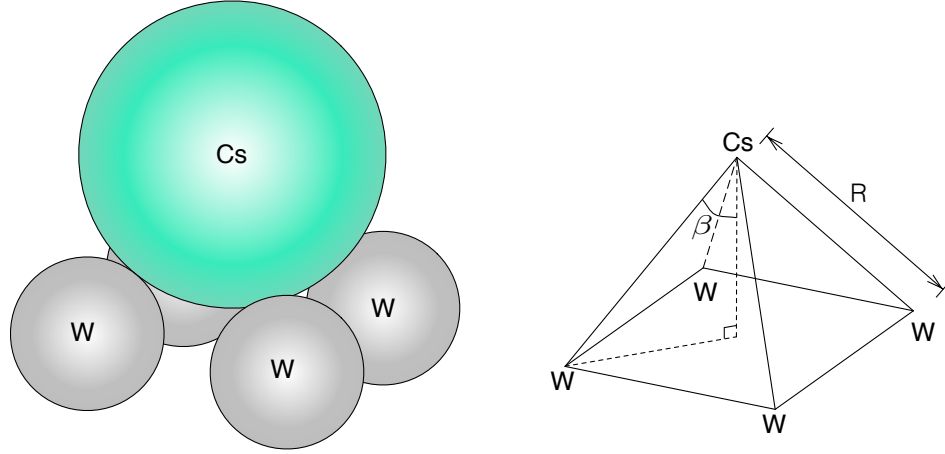


Figure 5.2: Arrangement of a cesium atom on the  $[100]$  surface of tungsten.

of available binding sites, and  $\theta$  is the fraction of those sites which are occupied (*aka* the coverage).

In Eq (5.4),  $\sigma$  is determined from information on the type of solid and the crystal face. For the purposes of this study, the evaporation of cesium atoms off of tungsten is considered. A tungsten solid forms a body centered cubic lattice with a lattice constant of  $3.15 \text{ \AA}$ . Knowing this, it is easy to calculate the atomic density per unit area of tungsten atoms for various crystal face cuts. A bound cesium atom at the surface will preferentially occupy spaces that are left in between adjacent tungsten atoms. For cesium on tungsten, the size of a cesium atom is such that there will be enough space on the tungsten lattice to accommodate 1 cesium atom for every 4 tungsten atoms [16]. An example of this arrangement for the  $[100]$  face of tungsten is shown in Fig 5.2. A calculated value of about  $10.0 \times 10^{14} \text{ atoms/cm}^2$  was obtained for the surface density of tungsten atoms on the  $[100]$  crystal face.

Dividing by 4 yields the calculated density of binding sites for cesium atoms to be  $2.5 \times 10^{14}$  sites/cm<sup>2</sup>. This is lower than the measured cesium density on the surface of tungsten reported by Taylor and Langmuir in their 1933 paper [53]. This difference is to be expected as an area of any tungsten surface will likely have more than one crystal face, not just [100]. The other crystal faces of tungsten, the [110] and [111] crystal faces, have tungsten atom densities that are  $14.0 \times 10^{14}$  atoms/cm<sup>2</sup> and  $17.0 \times 10^{14}$  atoms/cm<sup>2</sup> respectively [16]. The actual distribution of crystal faces for a solid tungsten surface is oftentimes an unknown. Therefore, there is some degree of ambiguity as to what the actual density of binding sites at the surface is. However, all values fall within an order of magnitude of  $10^{14}$  sites/cm<sup>2</sup>, and should not greatly affect the theory. For the rest of the chapter however, the assumption of a [100] crystal face of tungsten with  $\sigma = 4 \times 10^{14}$  sites/cm<sup>2</sup> is made.

With  $\sigma$  determined, most of the remaining work in applying Eq (5.4) is then calculating  $P$  and  $\tau$ . The remainder of this section is dedicated to explaining how these quantities are obtained.

### 5.3 Calculating the Evaporation Probability “P” and $V_0$

In order to apply Eq (5.3) to calculate  $P$ , the bound state energies  $E_n$ , and free state energies  $E_{free}$  need to be determined. These energies depend on the shape and size of the potential well each cesium atom experiences at its binding site. In this subsection, the assumptions and theory used for calculating  $E_n$  and  $E_{free}$  are explained. Parameters for cesium on tungsten are applied to the theory to yield

values for  $P$  as a function of coverage  $\theta$ .

From quantum mechanics, the bound state and free state energies for any arbitrary potential can be solved numerically from Schrödinger's equation. Therefore, to calculate  $E_n$  and  $E_{free}$ , most of the theory goes into determining the size and shape of the binding potential at the surface. It is assumed that the potential has no explicit dependence on time. Despite the complexity of the system, some reasonable simplifications can be made which allow the theory to develop further. Ignoring the possibility of surface roughness and contaminants, the binding sites for cesium atoms on a given crystal face cut should be indistinguishable from each other. As the cesium atom moves from site to site across the surface, it will experience the same periodic potential regardless of which direction it moves. Since the motion of the cesium atom along the plane of the surface does not contribute to evaporation, it is assumed that the problem can be reduced to an effective one dimensional binding potential in the  $z$  direction perpendicular to the surface. The second assumption that needs to be made is in the actual shape of the effective potential in the  $z$  direction. While many of the common potentials encountered in textbooks<sup>3</sup> are idealizations and do not represent realistic potentials encountered in nature, their simplicity alone is enough to make them useful as a first order approximation to many physical problems when other assumptions in the problem outweigh the need to seek for more accuracy. Because a simple theory to capture the physics of evaporation was sought after, a one dimensional square well potential shown in Fig 5.3 is used to approximate the desorption energy barrier. This leaves only two parameters

---

<sup>3</sup>harmonic oscillator, square well, linear, dirac delta potential, etc.

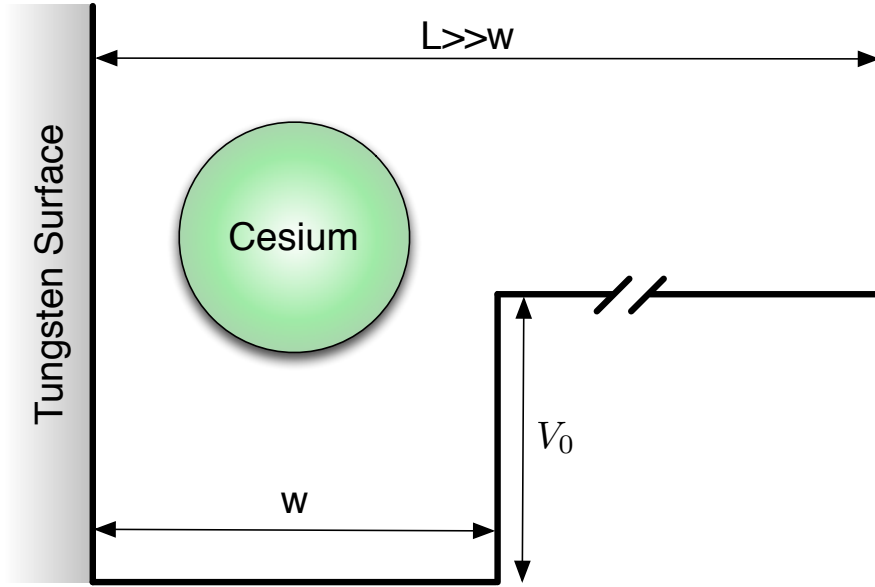


Figure 5.3: Effective 1D potential well used to model the evaporation.

to determine for the potential barrier: the well width  $w$  and the well depth  $V_0$ .

The well width  $w$  shown in Fig 5.3 is related to the range of the interaction forces between the cesium atoms and the lattice on which they are bound to. Since cesium atoms evaporate mostly as neutrals, the well width  $w$  is less than a nm (here,  $5 \text{ \AA}$ , or the covalent diameter of a Cs atom), and is set in a larger bounded region of length  $L \gg w$  so that  $E_{free}$  is discrete as well.

The remaining focus will now be in calculating the well depth parameter  $V_0$ . The theory here assumes that  $V_0$  is separable into several independent terms arising from the different physics that are present on the surface. The various terms contributing to  $V_0$  will now be introduced. More detailed derivations for each term present in  $V_0$  will be given separately in the sections that follow.

The first contribution to  $V_0$  is due to the Coulomb interactions arising from

the partial transfer of charge  $\pm Fe$  between the cesium atoms and the surface. In this expression,  $F$  is a dimensionless number and  $e$  is the fundamental charge of an electron. Cesium atoms partially ionize on solids to form a dipole layer at the surface<sup>4</sup> [16]. The dipole barrier is responsible for the electrostatic contribution to the binding potential  $V_0$  at the surface. Gyftopoulos et. al. also showed that this dipole barrier vanishes as a uniform monolayer of cesium is reached on the surface. Therefore, the Coulomb contributions to  $V_0$  vanish for a full monolayer coverage.

The second component to  $V_0$  is due to a combination of van der Waals dispersion forces as well as Pauli repulsion between cesium atoms on the surface with each other. While the totality of these interactions are complex and still not well understood, they are well approximated by the semi-empirical Lennard-Jones potential. Unlike the Coulomb interactions at the surface which vanish as a full monolayer is reached, the Lennard-Jones interactions do not. Including these interactions ensures that as the surface coverage approaches a full monolayer, the interactions approach those for a neutral cesium lattice.

The third contribution to  $V_0$  is due to the thermodynamics of the surface for a given coverage and temperature. Physical systems will tend towards configurations which maximize the entropy and minimize the free energy [18]. It will be shown that the thermodynamic contribution to  $V_0$  will be proportional to a thermodynamic factor given by  $\partial(\mu/kT)/\partial(\log \theta)$ .

Finally, the fourth contribution to  $V_0$  arises from the covalent bond formed between the adsorbed cesium and the substrate due to the partial sharing of the

---

<sup>4</sup>This is what leads to work function lowering of surfaces coated with cesium

valence band electrons. The covalent contribution should be independent of coverage and temperature and will be approximated as a constant that will be determined from experimental data. This constant is the only parameter in the model that is determined from fitting to experiment. Experimental data on cesium evaporation off tungsten taken by Taylor and Langmuir [53] was used to determine the covalent contribution to  $V_0$ .

In summing all these contributions together, the potential energy  $V_0$  is given to be:

$$V_0 = V_C + V_{LJ} + V_\mu + V_{CV} \quad (5.5)$$

Where  $V_C$  is the Coulomb contribution,  $V_{LJ}$  is the Lennard-Jones contribution,  $V_\mu$  is the thermodynamic contribution, and  $V_{CV}$  is the covalent contribution. The first three contributions are dependent on coverage  $\theta$  as well as temperature  $T$ . They will be discussed in turn in the the next few subsections. The last term  $V_{CV}$  is constant and will be determined from experimental data.

### 5.3.1 The Coulomb Contribution to $V_0$

Let  $V_C$  be the contribution to the well depth  $V_0$  arising from electrostatic forces on the surface. The expression sought after for the Coulomb contribution,  $V_C$ , is of the form:

$$V_C = \delta + \sum_{i=0}^4 N(i, \theta) V_{nn}^i \quad (5.6)$$

Eq (5.6) takes into account changes to  $V_C$  due to interactions with the surface, partially charged nearest neighbor cesium atoms, as well as interactions from atoms

farther away on the surface. The equation can be understood as follows: The first term  $\delta$  accounts for global interactions from charged cesium atoms farther away (because the electrostatic force is long range, it would be in error to consider only nearest neighbor interactions). The second term is the weighted average over the number of possible nearest neighbor configurations, where  $N(i, \theta)$  is the probability that a cesium atom will have  $i$  nearest neighbors for a given  $\theta$ .  $V_{nn}^i$  is the electrostatic potential a partially charged cesium atom on the surface experiences in the presence of “ $i$ ” nearest neighbors. For  $i = 0$ ,  $V_{nn}^0$  reduces to the electrostatic potential between the partially ionized cesium atom and the tungsten surface. For the [100] face of tungsten, a cesium atom can have between 0 to 4 nearest neighbor atoms. The weighting term,  $N(i, \theta)$ , is the probability that a cesium atom on the surface will have  $i$  nearest neighbors given a particular surface coverage  $\theta$ .

The expression used for  $V_{nn}^i$  will now be derived. In the dipole model of the surface, a partially charged cesium atom at the surface will form an image of equal but opposite charge a distance  $d$  away into the surface. Therefore, a cesium atom with  $i$  nearest neighbors will interact with both the atoms as well as their corresponding images. A schematic diagram of the interaction between a pair of cesium atoms on the surface is shown in Fig 5.4. Let  $\pm F(\theta)e$  be the charge of the cesium atoms and their images, then  $V_{nn}^i$  for a square lattice is:

$$V_{nn}^i = \frac{-kF^2e^2}{d} + i \cdot \left( \frac{kF^2e^2}{a} - \frac{kF^2e^2}{\sqrt{d^2 + a^2}} \right) \quad (5.7)$$

where  $a$  is the nearest neighbor separation distance,  $d$  is the distance between the cesium atom and its corresponding image,  $e$  is the fundamental charge unit, and  $k$

is the Coulomb constant. From the theory by Gyftopoulos and Levine [16],  $\pm F(\theta)e$  can be derived from knowing the strength of the dipole moment  $M$  produced by each cesium atom at the surface. The dipole moment  $M$  can be written as  $M = Fed$ , where  $d$  is the thickness of the surface dipole layer. Knowledge of  $M$  and  $d$  will result in  $F$  being determined.

According to Pauling [46] and Malone [31], the magnitude of the dipole produced when two dissimilar atoms come in contact is proportional to the difference in their relative electronegativities. From Pauling's rule, the strength of the dipole moment produced is given by:

$$M_0 = \chi(x_s - x_{Cs}) \quad (5.8)$$

where  $\chi = 3.83 \times 10^{-30}$ C-m/V is taken from literature.  $x_s$  and  $x_{Cs}$  are the relative electronegativities of the substrate atom and the adsorbed cesium atom respectively. Gyftopolous and Levin states that Pauling's correlation in Eq (5.8) does not correctly account for self depolarization. A more correct expression for the dipole moment is:

$$M_0 = \chi \frac{(x_s - x_{Cs})}{(1 + \alpha/(4\pi\epsilon_0 R^3))} \quad (5.9)$$

where  $R$  is the sum of the cesium and substrate covalent radii and  $\alpha$  is the polarizability of cesium. For the [100] face of tungsten, a cesium atom on the surface will be in contact with 4 surrounding tungsten atoms in the geometry shown in Fig 5.2. The net dipole moment produced is then given by:

$$M = 4M_0 \cos \beta \quad (5.10)$$

From Eq (5.9) and Eq (5.10), the factor  $F$  as a function of coverage can be written as:

$$F(\theta) = \frac{M}{ed} = \frac{4\chi(x_s - x_{Cs})G(\theta)}{eR(1 + \alpha/(4\pi\epsilon_0R^3))} \quad (5.11)$$

where an extra factor  $G(\theta)$  is added to account for the electronegativity variation with coverage at the surface.  $G(\theta)$  is commonly known as the Gyftopolous structure factor [16].  $R \cos \beta$  is the expression that Gyftopolous et. al. uses for “ $d$ ”, the thickness of the dipole layer at the surface. Lastly,  $\beta$ , presented in Fig 5.2, varies with crystal face.

Some care must be taken to point out the simplifications and incorrect physics used in this dipole model. The electron, a fundamental particle with charge  $e$ , can never be divided further. Therefore, the quantity “ $F(\theta)e$ ” in Eq (5.11) is unphysical in reality. A more realistic explanation of the physics is that when the cesium atom sits on the surface, the electron clouds redistribute in a particular way to produce a net electric field that mimics that of a dipole field. The calculation of the actual electron cloud distribution for the cesium-substrate system is an extremely difficult numerical problem and for most models including this one, unnecessary. Therefore, the dipole model is a good approximation for the fields the cesium atoms produce when sitting on the surface. The dipoles for a given coverage  $\theta$  are modeled with cesium atoms having partial charge  $+F(\theta)e$  and their corresponding image charges a distance “ $d$ ” away with charge  $-F(\theta)e$ .

The weighting term  $N(i, \theta)$  in Eq (5.6) is now discussed.  $N(i, \theta)$  is taken from the statistics for nearest neighbor occupation numbers for a given lattice already

developed in the Beth-Peierls approximation [47]. For a square lattice with each site having 4 neighboring sites, the probability  $N(i, \theta)$  of a cesium atom having  $i$  nearest neighbors where  $\theta$  is the surface coverage is given by:

$$\begin{aligned}
 N(i, \theta) &= \binom{4}{i} \frac{(ze^{-\epsilon/k_T T})^i}{(1 + ze^{-\epsilon/k_T T})^4} \\
 z &= \frac{(\eta - 1 + 2\theta)}{(2e^{-\epsilon/k_T T}(1 - \theta))} \\
 \eta &= \sqrt{1 - 4\theta(1 - \theta)(1 - e^{-\epsilon/k_T T})}
 \end{aligned} \tag{5.12}$$

Eq (5.12) for  $N(i, \theta)$  can be understood as follows: The combinatorics term  $\binom{4}{i}$  is necessary to account for the number of ways  $i$  atoms can be arranged around the 4 neighboring sites. This is multiplied by a weight that is very similar to that of the grand canonical ensemble. In the equation,  $z$  is a fugacity like term to account for the background chemical potential set up by the fractional  $\theta$  coverage of cesium globally. It is noted in Eq (5.12) that  $z$  is  $\theta$  dependent. The Boltzmann factor  $e^{-\epsilon/k_T T}$  accounts for the interactions between nearest neighbor cesium atoms with  $\epsilon$  being the interaction energy between two cesium atoms on the surface. The  $(1 + ze^{-\epsilon/k_T T})^4$  factor in the denominator is simply to ensure that the probabilities sum to unity. Because of the similarity between  $z$  and fugacity, the Beth-Peierls approximation is oftentimes known as the quasi-chemical approximation [18]. The interaction energy  $\epsilon$  in Eq (5.12) is simply the work that's required to bring a cesium atom an infinite distance away on the surface to the nearest neighbor separation distance of  $a$ :

$$\epsilon \equiv - \int_{\infty}^a \vec{N}_{net} \cdot d\vec{x} \tag{5.13}$$

$\vec{N}_{net}$  is the net force acting on the cesium atom as it is moved from infinity to  $a$ .

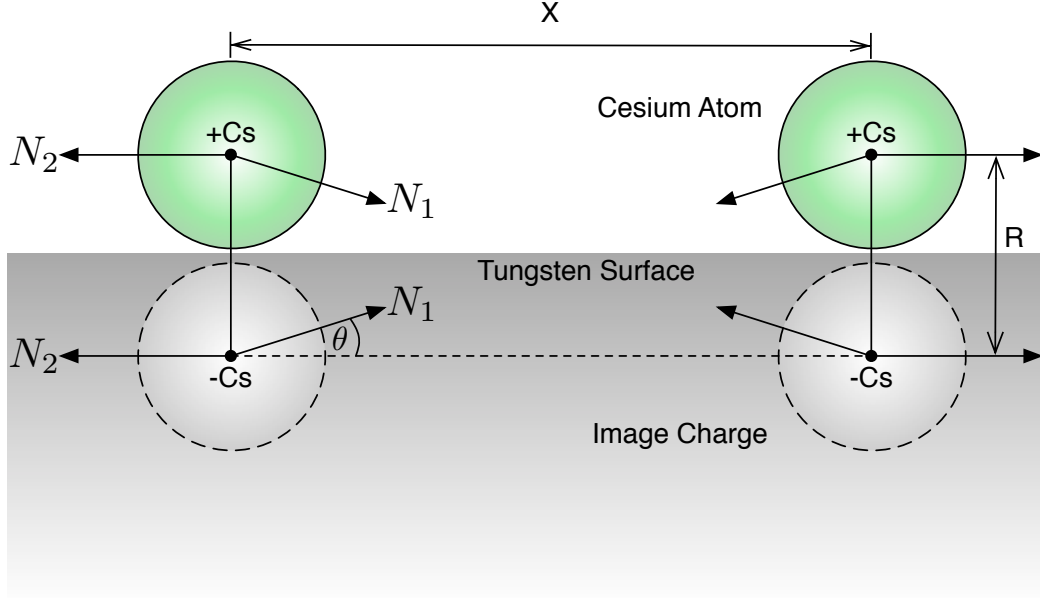


Figure 5.4: Cesium interaction with image charge and nearest neighbor

$\vec{N}_{net}$  can be calculated from the schematic force diagram in Fig 5.4. From Fig 5.4, the component of the net force on the cesium atom and its image charge parallel to the surface is given by:

$$2N_{1x} + 2N_{2x} = 2k \frac{F^2 e^2}{x^2} - 2k \frac{F^2 e^2}{x^2 + R^2} \cos \theta \quad (5.14)$$

where  $k$  is again the Coulomb constant, and  $x$  is the distance of interaction shown in Fig 5.4. Combining Eq (5.13) and Eq (5.14), and assuming  $a \approx R$ , the Coulomb interaction energy between nearest neighbor cesium pairs on the surface is:

$$\epsilon = k \frac{F^2 e^2}{R} \left( \frac{2\sqrt{2} - 2}{\sqrt{2}} \right) \quad (5.15)$$

With  $\epsilon$  determined, Eq (5.7) and Eq (5.12) can be applied to obtain  $N(i, \theta)$  as well as  $\sum_{i=0}^4 N(i, \theta) V_{nn}^i$ . To complete the expression for  $V_C$  (Eq (5.6)), all that remains

is to calculate the effect of long range interactions  $\delta$  for various temperatures and coverages.

Globally, partially charged cesium atoms move around on the surface in a way that can be approximated as 2D Maxwell-Boltzmann ensemble in equilibrium. Borrowing from plasma physics and in semiconductor physics, the effective interaction between the cesium atoms far away will be through a “screened” Coulomb interaction in 2 dimensions. The screening factor can be given by the Debye-Hückel approximation to be  $e^{-k_0 r}$  [41]. The damping factor “ $k_0$ ” describes the strength of the shielding. Using the Debye-Hückel approximation, the contribution to the electrostatic energy from far away atoms can be expressed as:

$$\delta = \sum_i \frac{kF^2 e^2 (2\sqrt{2} - 2)}{r_i \sqrt{2}} e^{-k_0 r_i} \quad (5.16)$$

where the summation index  $i$  sums over all occupied sites on the surface. For the [100] crystal face of tungsten, the surface in which the cesium atoms move on is a square lattice. It will be assumed that differences between various crystal faces are negligible. Indexing each cesium adsorption site the by  $(m, n)$  Eq (5.16) reduces to:

$$\delta = \theta \epsilon \sum_{n=-\infty}^{\infty} \sum_{m=-\infty}^{\infty} \frac{1}{\sqrt{m^2 + n^2}} e^{-k_0 a \sqrt{m^2 + n^2}} \quad \text{where } m, n \neq 0 \quad (5.17)$$

where  $\epsilon$  is given by Eq (5.15) and  $\theta$  is the fractional coverage of the surface. The summation can be approximated by noting that  $\int_{-\infty}^{\infty} \int_{-\infty}^{\infty} (1/\sqrt{x^2 + y^2}) e^{-k_0 a \sqrt{x^2 + y^2}} dx dy = 2\pi/(k_0 a)$ . The expression for  $k_0$  given by the Debye-Hückel approximation [13] is:

$$k_0 = \sqrt{\frac{k\sigma_1 \theta e^2}{k_T T}} \quad (5.18)$$

The final expression for  $\delta$  is then given by:

$$\delta \approx \frac{2\pi\theta\epsilon}{a\sqrt{(k\theta\sigma_1e^2)/(k_T T)}} \quad (5.19)$$

This completes the expression for  $V_C$ , the electrostatic contribution to  $V_0$  given by Eq (5.6):

$$V_C = \delta + \sum_{i=0}^4 N(i, \theta)V_{nn}^i$$

There is one last correction to  $V_C$  in Eq (5.6) still needing to be made. While the cesium atoms are partially ionized at the surface, they will still evaporate off as neutrals for temperatures below 900 K. So far, the expression for  $V_C$  in Eq (5.6) is the electrostatic energy required to remove a cesium ion with charge  $+Fe$  from the surface. But in practice, for the temperatures of interest in this dissertation cesium evaporates as a neutral not an ion. The correction that needs to be made is to add the energy required to remove the negative charge  $-Fe$  from the surface and add it to the cesium atom with charge  $+Fe$  to create a neutral atom. The energy required to remove a charge of  $-Fe$  from the surface is given by  $F\psi_e$ , where  $\psi_e$  is the workfunction of the material [27]. Combining the fractional electron with charge  $-Fe$  with the partially ionized cesium atom releases an amount of energy equal to  $F^2V_f$ , where  $V_f$  is the ionization potential of cesium [27]. The final expression for  $V_C$  with these corrections is given by:

$$V_C = \delta - F\psi_e + F^2V_f + \sum_{i=0}^4 N(i, \theta)V_{nn}^i \quad (5.20)$$

### 5.3.2 The Lennard-Jones Contribution to $V_0$

The second component to  $V_0$  is from the Lennard-Jones potential. The Lennard-Jones potential is an empirical formula for the short range energy of interaction between atoms due to van der Waals dispersion forces as well as Pauli repulsion. The potential is given in most texts to be the following [17]:

$$L = 4\varepsilon \left[ \left( \frac{r_m}{r} \right)^{12} - \left( \frac{r_m}{r} \right)^6 \right] \quad (5.21)$$

where  $\varepsilon$  and  $r_m$  are known as Lennard-Jones parameters, usually to be determined experimentally, and  $r$  is the separation distance between the atoms. The Lennard-Jones parameters used in the theory were given in Ref [14].

Since the Lennard-Jones potential is short ranged and falls off rapidly for increasing distance, only the nearest neighbor cesium atoms are considered. From simple superposition, the Lennard-Jones contribution to the well depth  $V_0$  from  $i$  nearest neighbors is given by:

$$L_i = i4\varepsilon \left[ \left( \frac{r_m}{a} \right)^{12} - \left( \frac{r_m}{a} \right)^6 \right] \quad (5.22)$$

The net contribution to the well depth  $V_0$  is from the weighted average of the Lennard-Jones contributions given by:

$$V_{LJ} = \sum_{i=0}^4 N(i, \theta) L_i \quad (5.23)$$

where  $N(i, \theta)$  is given by the Bethe-Pierls approximation in Eq (5.8).

### 5.3.3 The Thermodynamic Contribution to $V_0$

The third contribution to  $V_0$  is the thermodynamic contribution. The thermodynamic contribution to the well depth is given to be:

$$V_\mu = kT\theta \left( \frac{\partial(\mu/kT)}{\partial \log \theta} \right)_{T,A} \quad (5.24)$$

where thermodynamic contribution  $V_\mu$  is proportional to  $kT\theta$ , the free energy per unit adsorption site. The proportionality factor  $\partial(\mu/kT)/\partial(\log \theta)$ , is given by the Darken equation relating the change in the relative “order” of the surface to the chemical potential  $\mu$  set up by the cesium atoms on the surface [15]. The Darken equation is given by:

$$\left( \frac{\partial(\mu/kT)}{\partial \log \theta} \right)_{T,A} = \frac{\langle n \rangle}{\langle \Delta n^2 \rangle} \quad (5.25)$$

where  $\langle n \rangle$  is the average surface density and  $\langle \Delta n^2 \rangle$  is the average local fluctuation away from  $\langle n \rangle$  on the surface. Since the fluctuations  $\langle \Delta n^2 \rangle$  of the system is directly related to the entropy,  $\partial(\mu/kT)/\partial(\log \theta)$  is also a measure for the change in entropy of the surface as the coverage  $\theta$  is varied between 0 and 1. Since any system naturally tends towards states of higher disorder, the net effect of  $V_\mu$  should be to lower the well depth  $V_0$  as the coverage approaches a monolayer. For a two dimensional Langmuir surface of hard spheres, the expression for the chemical potential is given by:

$$\mu = \mu_0 + kT \log \left( \frac{\theta}{1 - \theta} \right) \quad (5.26)$$

Applying this Eq (5.24), the following expression is obtained for the thermodynamic contribution  $V_\mu$ :

$$V_\mu = kT \left( \frac{\theta}{1 - \theta} \right) \quad (5.27)$$

### 5.3.4 Summary

All terms in Eq (5.5) to evaluate  $V_0$  are now in place: with  $V_0$  in Eq (5.5) determined as a function of  $\theta$  and  $T$ , Eq (5.3) is applied to determine  $P$ , the probability of a cesium atom having enough energy to evaporate. Combined with  $\tau$  and  $\sigma$ , Eq (5.4) then gives the evaporation rate per unit area per unit time. As mentioned in previous sections, the theory here assumes a [100] crystal face of tungsten with  $\sigma$  given to be  $\sigma = 4 \times 10^{14}$  sites/cm<sup>2</sup>. The value of  $\tau$ , the characteristic time of evaporation on the surface, will now be calculated in the next section.

### 5.4 Calculating time $\tau$

From section 5.3, the variable  $\tau$  is the average time the cesium atom spends in a particular bound energy state before undergoing a transition. From Eq (5.4), the evaporation rate is proportional to  $1/\tau$ . In this subsection, the expression for  $1/\tau$  is calculated.

In the model, it is assumed that a bound cesium atom on the surface will likely undergo an energy change upon collision with any neighboring atoms on the surface. With this assumption,  $1/\tau$  is simply the collision frequency for the cesium atom in a given energy state.

In the absence of nearest neighbor atoms, a cesium atom on the surface will only undergo collisions with the surface lattice itself. The collision frequency in this case can simply be approximated as the frequency of oscillation for the cesium atom in the effective 1-D potential set up by the surface introduced in section 5.3 earlier

(Fig 5.3). The potential well with parameters  $V_0$  and  $w$  derived in the previous section for calculating the escape probability  $P$  will also be used here.

Quantum mechanically, a bound particle with energy  $E$  will undergo oscillations with frequency given by  $E/2\pi\hbar$ . Therefore, the oscillation frequency  $\nu_0$  averaged over all the available bound states is given by:

$$\langle \nu_0 \rangle = \frac{\sum_{i=0}^n \frac{E_i}{2\pi\hbar} e^{-E_i/kT}}{\sum_{i=0}^n e^{-E_i/kT}} \quad (5.28)$$

Here,  $E_i$  are the bound energy states calculated using the appropriate parameters  $V_0$  and  $w$ . Eq (5.28) gives the ensemble averaged collision frequency of a cesium atom that sits by itself on the lattice with no nearest neighbors.

If the cesium atom is surrounded by nearest neighbor atoms, then the calculation for the collision frequency will be modified. In the case of nearest neighbors, not only can the atom undergo collisions with the surface, but also with adjacent cesium atoms. In the latter case, collisions with neighboring atoms on the surface are caused by the transverse momentum components of the cesium atom. Continuing with the assumption that the transverse and perpendicular directions are separable on the surface, collisions with the surface lattice and collisions with other cesium atoms can be separated as follows – the contribution from collisions with the surface will be from the oscillation frequency of the atom bound within the potential in the  $z$  direction. The contribution from collisions with adjacent atoms will be from the oscillation frequency of the atom bound within a potential in the  $x$  and  $y$  directions across the surface.

The potential in the  $z$  direction is simply the potential well with parameters  $V_0$  and  $w$  derived in the previous section for calculating  $P$ , also used earlier to calculate the collision frequency with no nearest neighbors  $\nu_0$  in Eq (5.28). Assuming that nearest neighbor cesium atoms can be approximated as immovable hard spheres, the potential in the  $x$  and  $y$  directions for a cesium atom surrounded by nearest neighbors can be approximated by infinite potential walls. This oversimplification must be made for tractability and its validity will be determined by comparison with experiment. A more realistic model probably would have been to assume a harmonic oscillator potential to account for nearest neighbors. However, the lattice coupling constant between cesium atoms on the surface is unknown and would introduce an additional fitting parameter, which is not desirable for the model.

For a cesium atom surrounded by 4 nearest neighbors, the  $xy$  potential can be approximated by a two dimensional infinite square box with side length “ $a$ ”. Here, “ $a$ ” characterizes the distance in between adjacent atoms. The energy levels for a particle in a 2 dimensional infinite square box is given by the following:

$$E_{n_x, n_y} = \frac{\hbar^2 \pi^2 (n_x^2 + n_y^2)}{2ma^2} \quad (5.29)$$

It should be noted that the neighboring cesium atoms are finite in size so the infinite square box potential does not take this into account. However, if the atoms assume a Maxwell-Boltzmann ensemble, then higher energies states do not contribute much to the average quantities. At low energies, the energy levels for the finite potential box and the infinite box are very close to one another. The expression for the collision

frequency for a cesium atom surrounded by 4 nearest neighbors is then given by:

$$\langle \nu_4 \rangle = \frac{\sum_{j,k=0}^{n_x, n_y} \sum_{i=0}^n \frac{E_i + E_{j,k}}{2\pi\hbar} e^{-(E_i + E_{j,k})/kT}}{\sum_{j,k=0}^{n_x, n_y} \sum_{i=0}^n e^{-(E_i + E_{j,k})/kT}} \quad (5.30)$$

where  $E_i$  are the bound energy states in the z direction calculated using the appropriate parameters  $V_0$  and  $w$ , and  $E_{j,k}$  is given by Eq (5.29).

The next case to consider is a cesium atom that is surrounded by 2 nearest neighbor atoms, one on each side. Depending on the orientation, the cesium atom will undergo collisions with its neighbors in only one dimension, either x or y. The transverse contribution to the collision frequency for this case can therefore be approximated by calculating the frequency of oscillation of the cesium atom in a 1-D infinite square well.

$$\langle \nu_2 \rangle = \frac{\sum_{j=0}^{n_x} \sum_{i=0}^n \frac{E_i + E_j}{2\pi\hbar} e^{-(E_i + E_j)/kT}}{\sum_{j=0}^{n_x} \sum_{i=0}^n e^{-(E_i + E_j)/kT}} \quad (5.31)$$

where the  $x$  direction was chosen with no loss of generality and  $E_j$  are the energy levels for a particle in a 1-D infinite box. Before proceeding further, it must be mentioned that there is another arrangement possible for an atom surrounded by 2 nearest neighbors. The 2 neighboring atoms need not be arranged on opposite sides of the center atom, but also can be arranged adjacent to each other. For simplicity, the collision frequency for this case is assumed to be similar to the one calculated in Eq (5.31).

Lastly, the collision frequency for  $\langle \nu_1 \rangle$  is approximated as the average between  $\langle \nu_0 \rangle$  and  $\langle \nu_2 \rangle$ . The collision frequency for  $\langle \nu_3 \rangle$  is approximated as the average

between  $\langle \nu_2 \rangle$  and  $\langle \nu_4 \rangle$ . The net cesium collision frequency at the surface is then calculated as:

$$\langle \nu \rangle = \sum_{i=0}^4 \langle \nu_i \rangle N(n, \theta) \quad (5.32)$$

where  $N(i, \theta)$ , the probability of a cesium atom having  $i$  nearest neighbors for a surface coverage  $\theta$ , is given by the Beth-Peierls approximation introduced in the previous section.

## 5.5 Limitations of the Model and Future Work

In this section, an overview of the limitations and future work of the evaporation model presented in this chapter are discussed.

The first limitation of the model is that it cannot predict evaporation rates for coverages  $\theta$  outside of the range from 0 to 1. The evaporation model developed in this chapter has a singularity which causes the well depth parameter  $V_0$  in Eq (5.5) to diverge to infinity at  $\theta = 1$ , or a monolayer. The singularity is caused by the presence of a  $1 - \theta$  term in the denominator of the thermodynamic contribution  $V_\mu$  to the well depth in Eq (5.27). The  $1 - \theta$  term comes from assuming that the chemical potential of the surface is that of a two dimensional Langmuir layer given by Eq (5.26). The hard sphere interaction of the Langmuir layer causes the chemical potential to diverge as  $\theta$  goes to unity. Therefore, the model is nonphysical for values of  $\theta$  greater than  $\theta_{max}$ , the value of  $\theta$  in which the well depth  $V_0$  in Eq (5.5) goes to zero. In the model,  $\theta_{max}$  will be close to 1 but will vary slightly for different parameters such as temperature. At coverages around or greater than a monolayer,

the evaporation rates are high enough such that it becomes difficult to maintain an equilibrium coverage of cesium. Such high values of  $\theta$  are not of interest for the purposes of predicting the performance of CPD photocathodes since optimum electron emission typically occurs for cesium coverages of around 0.6. Therefore, almost all simulations using the evaporation model are such that the singularity at  $\theta = 1$  is irrelevant.

The second limitation of the model is that it does not take into account varying crystal faces on the surface. In the derivation, the model assumes a [100] crystal face geometry. Other crystal face geometries such as the [110], and [111] face can also be considered, but it has been assumed here that they do not significantly change the results. However, an area of future work will be to perform the model for evaporation over various crystal face surfaces. Such an analysis would yield further predictive capabilities of the model.

Lastly, in the derivation, the model simplifies the potential into the one shown in Fig 5.3. It will be shown later in comparing to experiment that this fictitious potential gives good agreement, and reproduces the nonlinear behavior of evaporation with varying coverage and temperature. However, it will be another area for future research to apply various other well shapes such as a harmonic well, or linear well and see how the results or predictions would vary.

## 5.6 Chapter Conclusions

- A model for cesium evaporation off tungsten was developed as part of a program to optimize and predict the performance of CPD photocathodes
- The evaporation model uses an effective one-dimensional potential well representation of the binding energy at the surface
- The evaporation model accounts for both local and global interactions of cesium with the surface metal as well as with other cesium atoms
- The end model contains only one constant parameter to be determined from experimental evaporation data taken by Taylor and Langmuir [53]. No other parameter is varied over the range of coverages and temperatures considered.

## Chapter 6

### Simulations of Cesium Tungsten Controlled Porosity Dispenser

#### Photocathode

The results obtained for the modeling are presented in this chapter. The first section in this chapter presents the results from chapter 3 for modeling the cesium coverage along the pore walls up to the surface. The second section discusses the results for the evaporation model presented in chapter 5 of cesium off tungsten surfaces. The third section combines the models and techniques developed for cesium resupply, diffusion, and evaporation (chapters 3-5) to give a map of the quantum efficiency of the CPD photocathode surface shown in Fig 1.4.

The results demonstrate that the model can be used as a predictive tool for the performance of a CPD photocathode for various parameters. Parameters such as the temperature, cathode thickness as well as pore size are all inputs that can be varied. The results for the simulations indicate that CPD photocathodes are able to maintain a uniform cesium coverage across the surface during operation.

#### 6.1 Results for Modeling the Cesium Flow through CPD Pores

The results for modeling the cesium diffusion and flow through the source pores leading from the reservoir to the surface of a CPD during operation is now presented. In chapter 3, the cesium resupply rate from a CPD reservoir onto the

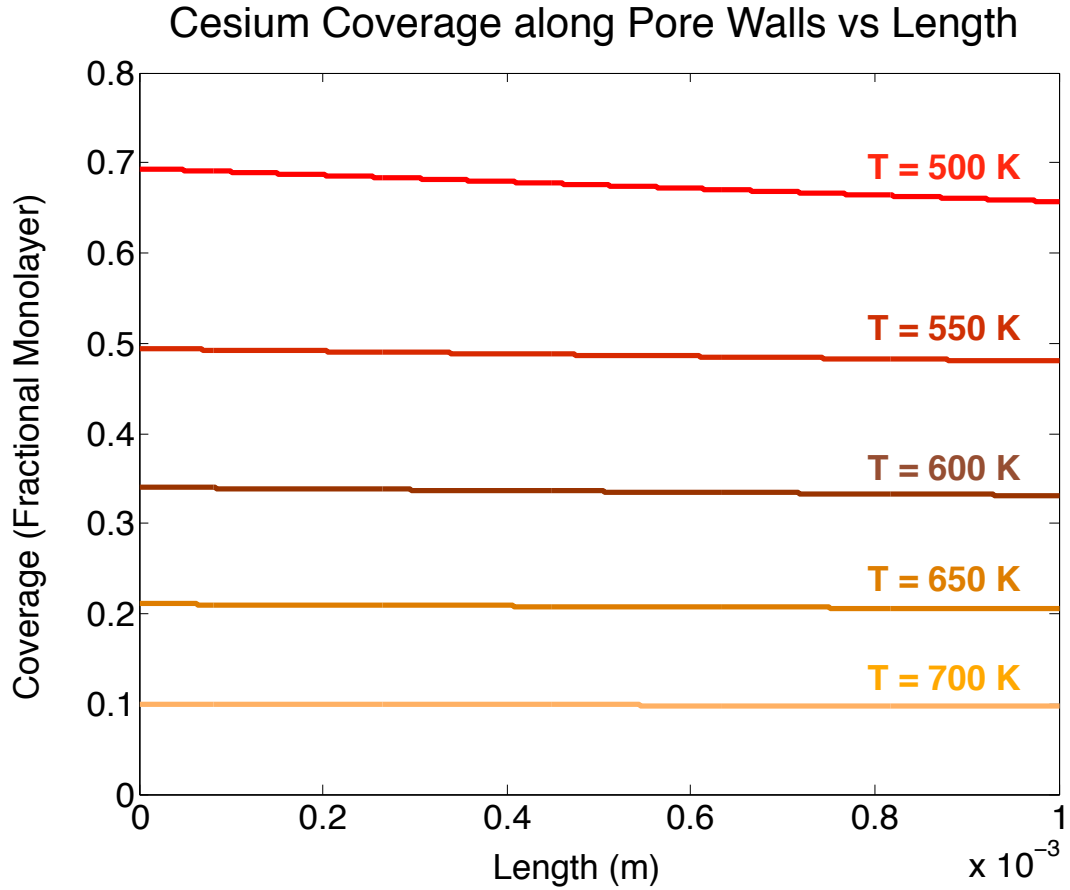


Figure 6.1: Results from modeling the cesium coverage along the pore walls as a function of distance down the pore

surface is primarily determined by the diffusion and flux of cesium along the walls of the pore, modeled by Eq (3.1). Eq (3.1) gives the cesium density  $\Theta$  maintained along the walls of the pores during CPD operation. This then determines the boundary conditions at the surface pore edges,  $\Theta_{pore}$  in equation (2.1) which determines the rate of cesium resupply to the surface.

Fig 6.1 shows plots of cesium coverage along the pore walls down the length of each pore for various temperatures. The results in Fig 6.1 were generated assuming an emitter thickness of one millimeter. Typical emitter thicknesses vary around

several millimeters with a pore radius of only several microns. The emitter thickness to pore radius ratio in this case was about  $L/R = 100$  (1 mm thickness with pore radius of 1 micron). Results in Fig 6.1 with  $L/R = 100$  reveal that the cesium coverage along the pore walls is fairly uniform for given temperatures. This is expected as diffusion happens much faster than evaporation. The same simulation was performed for  $L/R = 10$  and the results also show the coverage profile to be close the uniform down the pore. From these results it is argued that increasing the  $L/R$  value should not change the final distribution of coverage along the pore walls by much. In chapter 3 Eq (3.17)-(3.18), it was shown that for an infinitely long pore with uniform coverage, the evaporation flux  $F_{evap}$  exactly balances the flux onto the pore walls at all values of  $z$ . The result is that the coverage will stay uniform and not change for  $L/R \gg 1$ .

The other input parameter that was necessary to generate Fig 6.1 was the source term, or the flux of cesium atoms at the back end of the CPD emitter cap. The flux will be from the cesium vapor maintained at the back end of the emitter cap. For practical operation of CPD photocathodes, the cesium vapor in the reservoir is not directly exposed to the back of the CPD emitter cap. To limit the total cesium throughput, there will be a diffusion barrier between the actual reservoir filled with cesium vapor and the CPD emitter. This design was invented and prototyped by Montgomery, Ives, et al. in 2012 [34]. A schematic of the arrangement is shown in Fig 6.2. The diffusion barrier is made up of a sintered powder tungsten dispenser. The cesium diffuses through the sintered powder in a much slower and controlled manner before being available to pass into the source pores of the CPD emitter

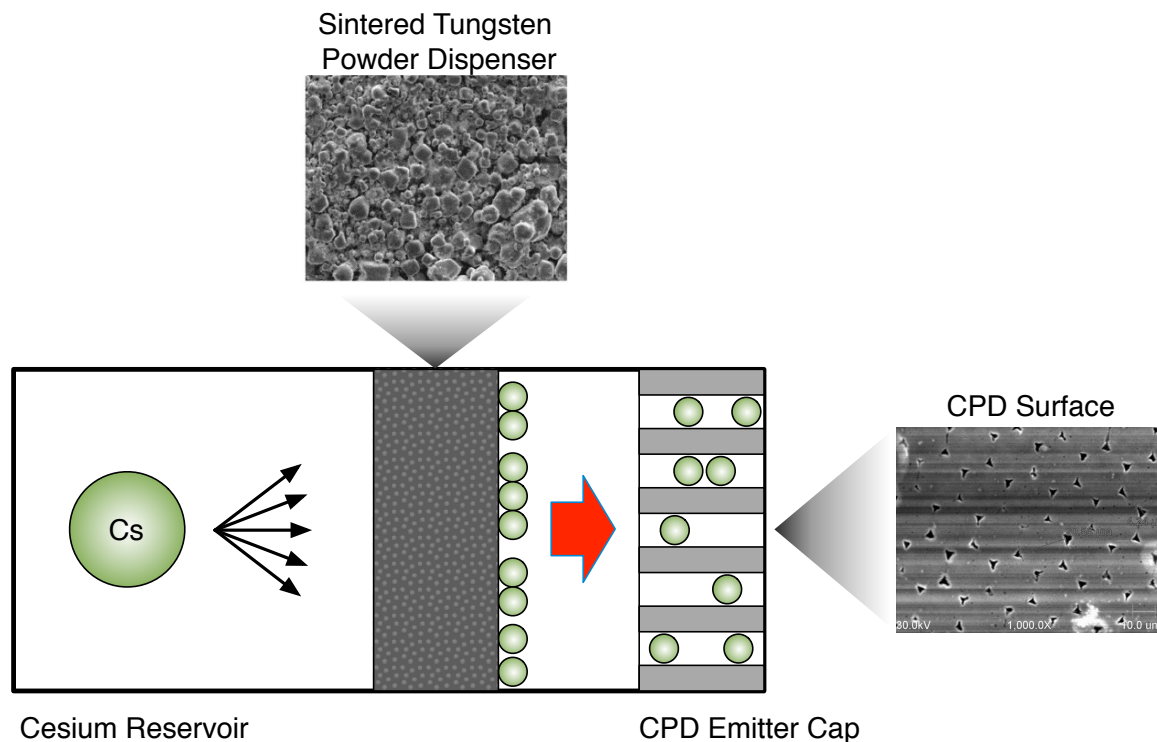


Figure 6.2: Schematic overview of the hybrid CPD dispenser [34]. The cesium throughput is limited and controlled by adding a sintered tungsten powder diffusion barrier between the reservoir and the CPD emitter [35].

array. Therefore, the cesium going into the source pores will be from the cesium atoms evaporating off the surface of the sintered tungsten powder directly behind the CPD emitter cap as shown in Fig 6.2. As discussed in Chapter 5, knowing the coverage that will be maintained at the surface will also determine the evaporation or flux unique to that temperature and coverage. The work then becomes to determine the coverage that is maintained for a given operating temperature at the surface of the sintered powder diffusion barrier.

In this case the coverage is inferred from past experimental data taken at UMD [36] for sintered powder dispenser photocathodes. QE measurements of cesium based sintered tungsten powder photocathodes can be used to back calculate the coverage

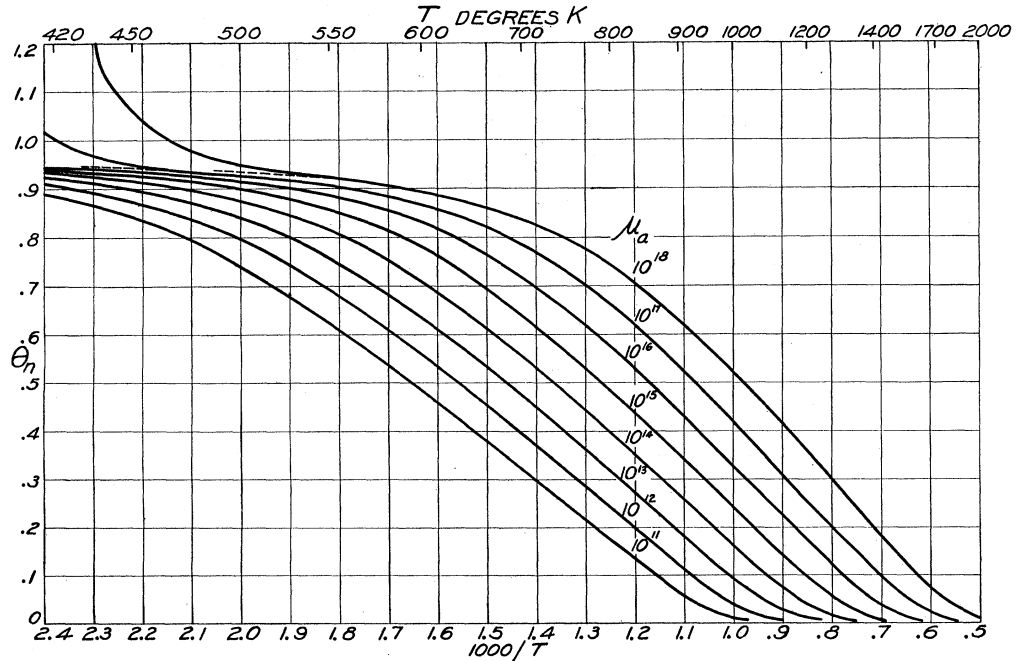


FIG. 10. Fraction ( $\theta_n$ ) of the tungsten surface covered with cesium at the temperature  $T$ ; calculated (Eq. (6) or Table I) for different  $\mu_a$ 's.  $\mu_a$  is proportional to cesium pressure.

Figure 6.3: Extrapolated curves from Langmuir's paper [53] for cesium coverage at various cesium vapor pressures. The coverage maintained goes linear in temperature over a wide range of temperatures, especially for lower vapor pressures.

from the workfunction lowering. At temperatures around and below 450K, the QE is such that there is close to a monolayer of cesium maintained on the surface of the sintered powder dispenser cathode. Above 700K, almost no QE is measured which indicates that very little cesium is present or is able to be maintained on the surface. For the inputs to the model, it was assumed that the cesium coverage on the surface of the sintered tungsten powder linearly decreases with  $1/T$  (where  $T$  is temperature) from  $\theta = 0.9$  at 450K, to  $\theta = 0.1$  at 700K. The linear dependence on  $1/T$  is supported from experimental data from published by Taylor and Langmuir shown in Fig 6.3. Fig 6.3 shows curves extrapolated from Taylor and Langmuir for cesium coverage maintained at various temperatures. Each curve in Fig 6.3

is a different partial cesium vapor pressure the surface is exposed to. It can be seen that especially for the lowest curves, the coverage at the surface has roughly a linear dependence with  $1/T$  for the given vapor pressure. This completes the determination of the input parameters used to apply equation (3.1) to calculate the results presented in Fig 6.1. Note that from the hybrid design, the coverage maintained on the surface of the diffusion barrier will be the same as or very close to the coverage of cesium maintained on the back end of the CPD emitter cap.

## 6.2 Results for Modeling Cesium Evaporation rates off CPD surfaces

The results of the evaporation modeling presented in chapter 5 are given in this section. In the context of this dissertation, evaporation  $F_{evap}$  appears in both Eq (2.1) in chapter 2 for modeling the CPD surface, as well as in (3.1) in chapter 3 for modeling the cesium resupply to the surface.

Fig 6.4 shows the comparison between the evaporation rates calculated from the theory with experimental data (and its extrapolation by Taylor and Langmuir) for cesium evaporation off tungsten. The extrapolated data presented by Taylor and Langmuir[53] is shaded in gray on the plot. The equation used for the extrapolation is given in their paper to be[53]:

$$\log_{10} F_{evap} = A - B/T \quad (6.1)$$

where  $A$  and  $B$  are coverage dependent fitting parameters determined from experimental data. Table 6.1 at the end of the chapter gives the tabulated values for  $A$  and  $B$  reported by Taylor and Langmuir.

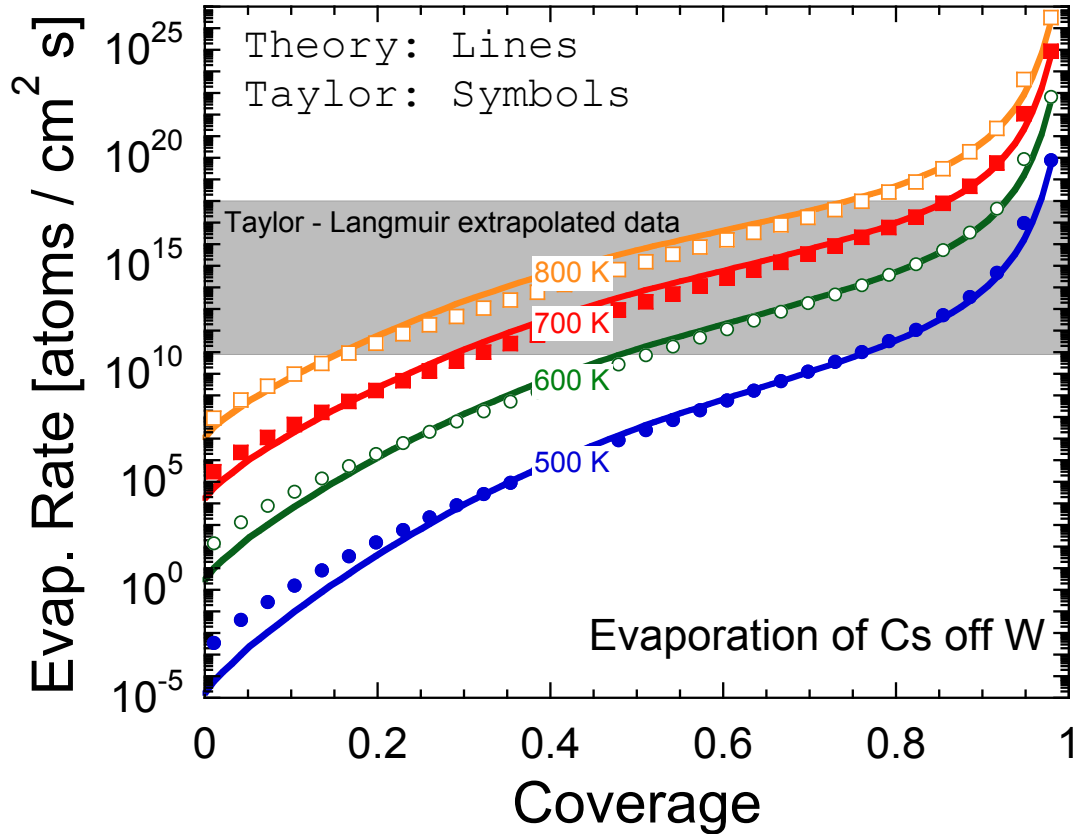


Figure 6.4: Comparison between theory and experimental data for evaporation of cesium off tungsten

From Fig 6.4, the model presented in chapter 5 captures the qualitative behavior of cesium evaporation over a wide range of coverages and temperatures. Quantitatively, the evaporation values predicted by the model agree to within 5% over the range of Langmuir’s data shaded in gray. In Fig 6.4, Eq (6.1) was used to extrapolate the data even further, beyond the range of Langmuir’s extrapolation. The model continues to give good qualitative agreement with the extrapolation even for coverages and evaporation rates outside of the shaded area. However, outside the shaded area, evaporation data has no real meaning since Taylor and Langmuir did not measure any such values and since it quickly becomes too low or too high to

measure accurately. A useful order of magnitude of reference for evaporation rates is a monolayer per second, which corresponds to roughly  $10^{14}$  atoms/cm<sup>2</sup> · sec.

As discussed previously in chapter 5, the model has a singularity at  $\theta = 1$ . However, for the purposes of simulating a CPD photocathode and comparing to the data within the gray area, the value for  $F_{evap}$  at  $\theta$  close to 1 is irrelevant. From Fig 6.4, there is still good agreement for coverages close to a monolayer up to 0.98.

### 6.3 Simulations for the QE map of a CPD photocathode

This section presents the results for modeling the surface QE distribution from cesium coverage for a CPD photocathode when the models for cesium resupply, diffusion, and evaporation are combined together via Eq (2.1).

In order to obtain the QE from the cesium coverage  $\theta$ , the Modified Fowler-Dubridge Model for QE was used [22] :

$$QE \approx (1 - R)F_{\lambda}(T) \left( \frac{U [\beta_T(\hbar\omega - \Phi(\theta))]}{U [\beta_T\mu]} \right) \quad (6.2)$$

Here,  $\hbar\omega$  is the energy of the incident photon,  $T$  is the temperature of the photocathode,  $\beta_T$  is the usual  $1/kT$ , and  $\mu$  is the Fermi level of the surface. A complete treatment of photoemission is beyond the scope of this dissertation and the reader is referred to the following references: [21] [51]. Eq (6.2) captures the major processes of photoemission as follows – the reflectivity of the surface,  $R$ , determines how much incident light is absorbed by the material; afterwards  $F_{\lambda}(T)$  gives the fraction of electrons that do NOT suffer a scattering event during their transport to the surface (if they do, they're lost, at least in the leading order approximation). Fi-

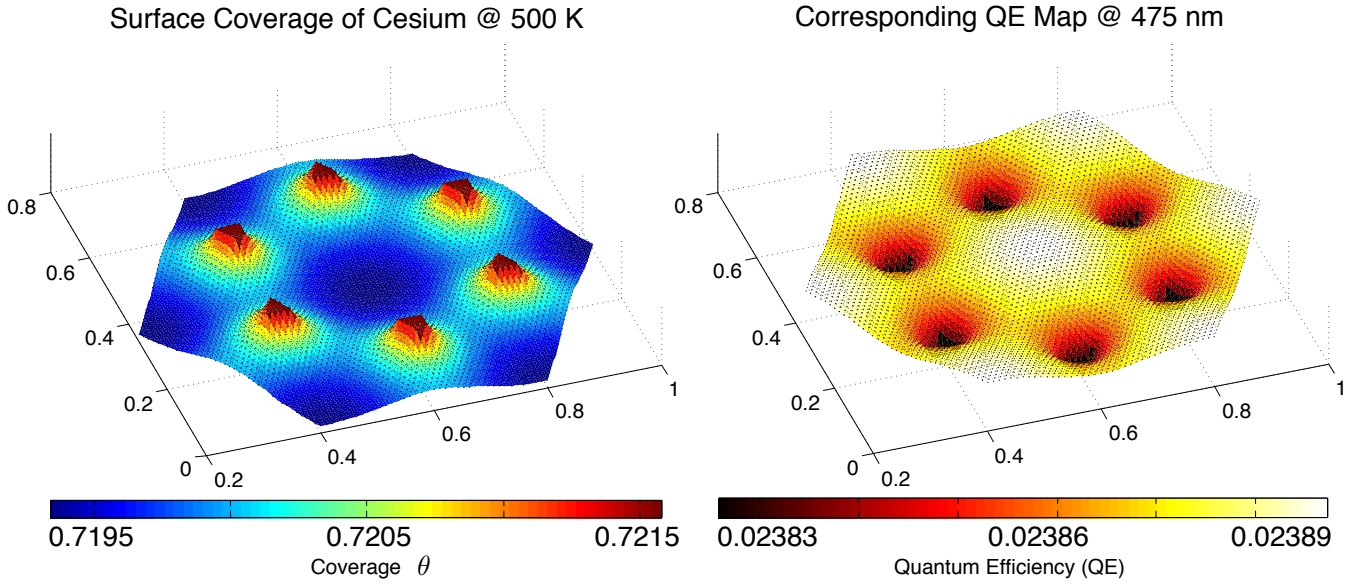


Figure 6.5: Results for modeling the cesium coverage  $\theta$  and the corresponding QE map across the surface for an operating temperature of 500 K at a wavelength of 475 nm

nally,  $U(x)$  is the Fowler-Duridge function and gives the probability for the electrons reaching the surface to escape into vacuum and be “emitted”. The cesium coverage  $\theta$  comes into play in determining the surface workfunction  $\Phi$  [36]. The workfunction vs cesium coverage for various metals including tungsten are studied and reported in previous works [16] [21].

Fig 6.5 presents a plot of the cesium coverage  $\theta$  and the corresponding QE map across the surface of a hexagonal region on the CPD (Fig 4.1) after equilibrium has been established. As discussed in chapter 4, because of the periodic nature of the CPD surface, it is only necessary to model a small region and assume periodic boundary conditions. At equilibrium, the simulations show that the QE across the surface is nearly uniform. As seen on the QE scale in Fig 6.5, there is less than a 1% variation in the QE maintained across the surface. The model also predicts that the

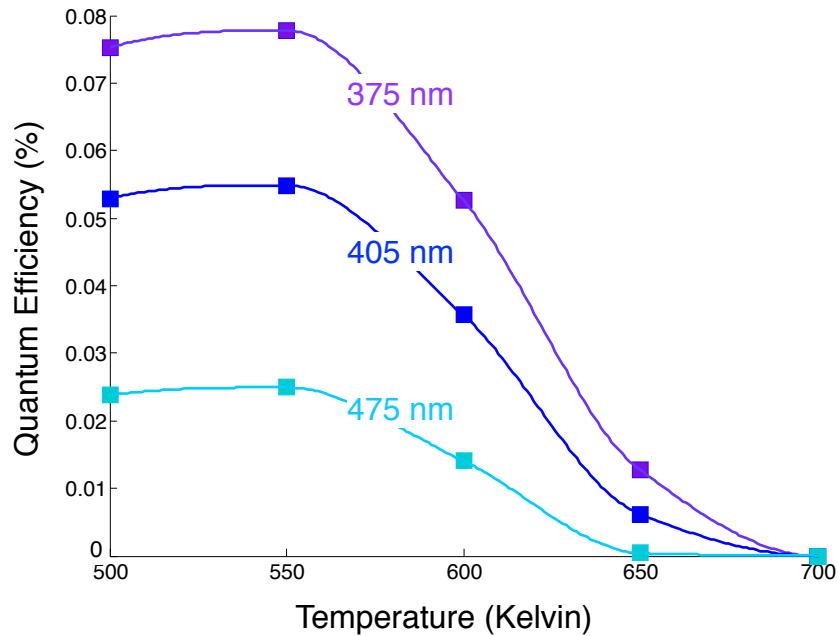


Figure 6.6: Simulations of Averaged QE of Cs:W as a function of Temperature and various wavelengths (nm)

QE maintained across the surface changes with temperature as expected. Higher temperatures yield lower cesium coverages on the surface thereby changing the QE. A plot of the average QE across the surface at various wavelengths as a function of cathode temperature is given in Fig 6.6. Though typical operating temperatures for a CPD photocathode will be closer to 500 K if rejuvenated continuously, or room temp (or lower) if rejuvenated periodically, the plot shows the predictive capabilities of the model over a range of temperatures.

Pore variations and non-homogeneity for realistic surfaces were also studied. Comparison with a scenario where two of the six pores in the simulated region were intentionally blocked off is shown in Fig 6.7. The ideal case where all the pores have the same Cs output is displayed next to it. Even for the non ideal case, there is no

greater than a 5% variation in QE across the surface compared to a less than 1% variation for an ideal surface where all the pores emit cesium uniformly.

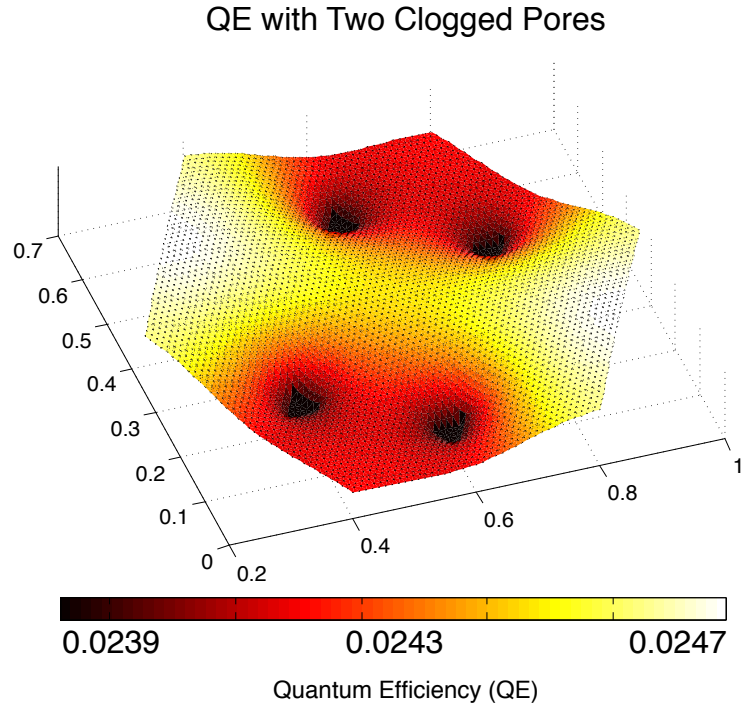


Figure 6.7: Results for modeling the QE map across the surface for an operating temperature of 500 K when two out of six pores are clogged

At peak operation, a CPD photocathode may be required to produce on the order of a nC of charge in less than 50 ps from  $\text{mm}^2$  areas, suggesting current densities on the order of  $1\text{kA}/\text{cm}^2$ . Differences in QE therefore can introduce non-uniformity which is correlated with increases in cathode intrinsic emittance. The present simulations for the CPD photocathodes concluded that the periodic pore arrangement, in both pore size and spacing, bodes well for maintaining more uniform coverage than would be possible using the random pore distribution and size characteristic of conventional sintered tungsten dispenser cathodes. The simulations also demonstrate that non uniformity in QE still can arise for realistic CPD surfaces. The

extent to which this affects the beam quality and emittance will be the subject of a separate investigation in a future work.

## 6.4 Chapter Conclusions

- The development of robust, long life, high efficiency photoemitters is critically needed for applications demanding high brightness electron sources, such as particle accelerators and high power Free Electron Lasers (FELs) [43].
- A model of the surface of a CPD, using a novel numerical technique, was developed to include resupply, evaporation, and migration of cesium.
- Simulations of cesium migration within the pores suggest that the coverage maintained along the pore walls to be close to uniform over the pore length. The cesium coverage able to be maintained at the surface is not strongly dependent on emitter thickness.
- The theory of cesium evaporation agrees with the experimental data taken by Taylor and Langmuir reported in their paper [53] to within 5%.
- Simulations of the CPD surface show the QE to be uniform at equilibrium during operation at various temperatures, with optimum operating temperatures at around 500 K.

Table 6.1: Experimental fitting data for evaporation rate extrapolation[53].

$$\log_{10} F_{evap} = A - B/T$$

Coverage	A	B
.002	24.2328	14043.2
.005	24.6401	14013.3
.01	24.9558	13963.8
.02	25.2859	13866
.03	25.4913	13769
.04	25.6459	13673
.05	25.7719	13579
.06	25.8804	13486
.07	25.9764	13394
.08	26.0633	13304
.10	26.2179	13127
.12	26.3556	12954
.15	26.5388	12703
.20	26.8081	12306
.25	27.050	11934
.30	27.276	11583
.40	27.707	10939
.50	28.142	10364
.55	28.375	10098
.60	28.629	9849
.65	28.916	9623
.70	29.256	9425
.75	29.683	9256
.80	30.266	9110
.85	31.159	8985
.90	32.821	8881
.95	37.495	8798

## Chapter 7

### Concluding Remarks

#### 7.1 Discussion of Results

Controlled porosity dispenser photocathodes (CPDs) are electron sources being developed for accelerator applications demanding high brightness electron beams such as Free Electron Lasers (FELs). CPDs promise to fill the current technology gap for a robust, long life, high efficiency photoemitters (Fig 1.1). The work done in this dissertation focuses on the modeling and simulation for the operation of tungsten based CPDs fabricated by sintering micron diameter tungsten wire (Fig 1.4). Such a model is useful for optimizing CPD performance during operation, as well as exploring the parameter space for CPDs. The results obtained in this study demonstrate that the model can be used to predict the operation of the CPD at various cathode temperatures and configurations.

The three major physical processes for a CPD photocathode that were modeled in this dissertation were:

1. Chapter 3: Cesium flow and resupply from the reservoir through the pores onto the surface
2. Chapter 4: Cesium diffusion across the surface from the pores
3. Chapter 5: Cesium evaporation off the CPD pores and surface during opera-

tion

For modeling the cesium flow and resupply from the reservoir through the pores, the results show the cesium coverage along the pore walls to be close to uniform over various temperatures, Fig 6.1. The coverage along the pore walls determine the cesium coverage at the pore boundaries on the surface which is how cesium resupply was simulated. The emitter thickness does not have a large affect on the cesium coverage along the pore walls and the cesium resupply rate to the surface for the regime where  $L/R \gg 1$  (where  $L$  is the emitter thickness and  $R$  is pore radius). The assumption of a linear pressure profile needs to be looked into and verified in a future work.

In modeling the cesium resupply, diffusion and evaporation at the surface, a QE map of the CPD surface was generated for various cathode temperatures and configurations. For the ideal configuration where all the pores are functioning, the model shows that the periodic geometry of the CPD allows the surface QE to not vary by more than 5% during normal cathode operation, as in Fig 6.5. In the case where some of the pores are blocked off, the simulations show more variation and structure to the QE maps generated, as in Fig 6.7. Such QE maps of the surface can be used in a future work to simulate the beam quality and or intrinsic emittance from the cathode for accelerator applications.

For the evaporation modeling of cesium off the surface of tungsten, comparison with experimental data taken by Taylor and Langmuir [53] gave impressive agreement across several orders of magnitude, as depicted in Fig 6.4. It is seen in Fig 6.4

that the theory performs well in capturing the qualitative behavior of evaporation over a wide range of coverages and temperatures. Quantitatively, the evaporation values predicted by the model agree to within 5% for the shaded gray region of Taylor's own reported extrapolations. In modeling the CPD, it was assumed that evaporation was primary mechanism in which cesium is lost on the CPD surface. Effects such as contamination and ion back bombardment, all things which are limited by vacuum quality, were not included. The model assumes that the vacuum is optimized such that affects from contamination are negligible when compared to evaporation over the lifetime of the CPD.

In the end, the theory developed is complete and is able to make predictions on the QE for CPD photocathodes at various temperatures and configurations in vacuum. It remains for future studies to modify the existing assumptions in the model as well as obtain predictions for the beam profile and emittance coming off the cathode going into the accelerator.

## Appendix A

### Main Source Code in MATLAB

```
% This is a diffusion code that simulates 2D surface diffusion on a hexgrid  
% plotted on a triangular interlaced lattice grid. On this grid each point  
% will be at the center of a hexagonal pattern and have six neighboring  
% points surrounding it. The 2D laplacian operator for each point on this  
% triangular grid will use all six of the neighboring points.  
  
%% Beginning Value Allocations  
  
global N Dx Dy A11 y d r h v sized1 n1 Beta Gamma pores AA T  
  
N = input('pore_discretization_parameter?\n');  
RR = input('Wire_Radius_in_meters?\n');  
LL = input('Emitter_Thickness_in_meters?\n');  
T = input('Temp?\n');  
timesteps = input('What_is_the_number_of_time_steps_you_wish_to_iterate?\n');  
  
NN_t = 2*N+30;  
  
pore1 = zeros(1,N+2*sum(1:N-1));  
pore2 = zeros(1,N+2*sum(1:N-1));  
  
s = (NN_t*2*10)+(20+N*2);  
s2 = (NN_t/2+5)*NN_t*2+20+(N*2)+20+1;
```

```

nn1 = 1;
nn2 = 1;
for i = 1:N
    pore1(nn1:nn1+2*(i-1))=s:s+2*(i-1);
    pore2(nn2:nn2+2*(N-i))= s2:s2+2*(N-i);
    s = s+2*NN_t-2;
    s2 = s2 + 2*NN_t;
    nn1 = nn1+2*(i-1)+1;
    nn2 = nn2+2*(N-i)+1;
end

```

```

i2 = N-2;
interior1 = 0;
interior2 = 0;
interior3 = 0;
interior4 = 0;
interior5 = 0;
interior6 = 0;

```

```

N2 = 2*NN_t;

vertex_x1 = zeros(1,(N2+1)^2);
vertex_y1 = zeros(1,(N2+1)^2);

nn = 1;
s1 = 0;
for i = 1:N2+1

```

```

vertex_x1 (nn:nn+N2) = s1:0.5:s1+N2*0.5;
vertex_y1 (nn:nn+N2) = 0:sqrt(3)/2:sqrt(3)/2*N2;
nn = nn+N2+1;
s1 = s1+1;

```

**end**

```

s1=1;
vs2 = 1:N2+1;
tri = zeros(2*N2*N2,3);
for i = 1:N2
    vs1 = vs2;
    vs2 = vs1+N2+1;
    tri(s1:2:s1+(2*N2-1)-1,1) = vs1(1:N2);
    tri(s1:2:s1+(2*N2-1)-1,2) = vs2(1:N2);
    tri(s1:2:s1+(2*N2-1)-1,3) = vs1(2:N2+1);
    tri(s1+1:2:s1+(2*N2-1),1) = vs1(2:N2+1);
    tri(s1+1:2:s1+(2*N2-1),2) = vs2(2:N2+1);
    tri(s1+1:2:s1+(2*N2-1),3) = vs2(1:N2);
    s1 = s1+2*N2;

```

**end**

```

pore11 = zeros(1,N+2*sum(1:N-1));
pore22 = zeros(1,N+2*sum(1:N-1));
nn1 = 1;
nn2 = 1;
for i = 1:N

```

```

    pore11(nn1:nn1+2*(i-1)) = pore1(nn1:nn1+2*(i-1))+N2*10+N2*(i);
    pore22(nn2:nn2+2*(N-i)) = pore2(nn2:nn2+2*(N-i))+N2*(NN_t/2+5)+N2*(i);
    nn1 = nn1+2*(i-1)+1;
    nn2 = nn2+2*(N-i)+1;
end

pore33 = pore22-60-2*N-2*N;
pore44 = pore11+ 2*N2*(NN_t-1)+N2;
pore55 = pore22+ 2*N2*(NN_t-1)+N2;
pore66 = pore44+60+2*N+2*N;

poreid1 = zeros(1, size(pore11,2));
poreid2 = zeros(1, size(pore11,2));
poreid3 = zeros(1, size(pore11,2));
poreid4 = zeros(1, size(pore11,2));
poreid5 = zeros(1, size(pore11,2));
poreid6 = zeros(1, size(pore11,2));

for i = 1:size(pore11,2)
    poreid1(i) = sum(vertex_x1(tri(pore11(i),1:3)))+
sum(vertex_y1(tri(pore11(i),1:3)));
    poreid2(i) = sum(vertex_x1(tri(pore22(i),1:3)))+
sum(vertex_y1(tri(pore22(i),1:3)));
    poreid3(i) = sum(vertex_x1(tri(pore33(i),1:3)))+
sum(vertex_y1(tri(pore33(i),1:3)));
    poreid4(i) = sum(vertex_x1(tri(pore44(i),1:3)))+
sum(vertex_y1(tri(pore44(i),1:3)));
    poreid5(i) = sum(vertex_x1(tri(pore55(i),1:3)))+

```

```

sum(vertex_y1(tri(pore55(i),1:3)));
poreid6(i) = sum(vertex_x1(tri(pore66(i),1:3)))+
sum(vertex_y1(tri(pore66(i),1:3)));
end
Npore = N;
N = N2;

vertex_x11 = zeros(1,(N+1)^2-((N/2*N/2)+N/2));
vertex_y11 = zeros(1,(N+1)^2-((N/2*N/2)+N/2));
mm = size(vertex_x11);
mm = mm(2);
mm = mm-N/2;
n1 = 1;
s1 = 0.5*N/2;
s2 = N;
ny1 = N/2*(sqrt(3)/2);

%% Hex Grid (x, y) Coordinate Allocation
%
% The following section of code assigns the correct (x,y) coordinate values
% to the vectors that store them vertex_x1 and vertex_y1. The code
% systematically fills each vector from both ends towards the center
% simultaneously. Graphically, this is the same as starting from the left
% and right most diagonal of the hex grid lattice and working towards the
% center diagonal.

for i = 1:N/2+1

```

```

vertex_x11(n1:n1+N/2+(i-1)) = s1:0.5:s1+0.5*((N/2)+i-1);
vertex_x11(mm:mm+N/2+(i-1)) = s2:0.5:s2+0.5*((N/2)+i-1);
vertex_y11(n1:n1+N/2+(i-1)) = ny1:sqrt(3)/2:ny1+sqrt(3)/2*((N/2)+i-1);
vertex_y11(mm:mm+N/2+(i-1)) = 0:sqrt(3)/2:sqrt(3)/2*((N/2)+i-1);

mm = mm-(N/2+i+1);

n1 = n1+N/2 + i;

s1 = s1+0.5;

s2 = s2-1;

ny1 = ny1-sqrt(3)/2;

end

xmax = vertex_x11((N+1)^2-((N/2*N/2)+N/2));
mm = 2*N*N*(1-1/4);
nn = 1;

mm2 = size(vertex_x11);
mm2 = mm2(2);
mm2 = mm2-N/2;
n1 = 1;
tri = zeros(1,3);
h = 1/(vertex_x11((N+1)^2-((N/2*N/2)+N/2))-vertex_x11(1));

%% Generate the Vertex Specification "tri" Matrix to Generate Hex Grid Base

for n = 1:N/2

```

$$vs1 = nn : nn + N/2 + (n - 1);$$

$$vs2 = nn + N/2 + n : nn + N + 2 * n;$$

$$tri(n1 : 2 : n1 + 2 * (N/2 + n - 1), 1) = vs1;$$

$$tri(n1 : 2 : n1 + 2 * (N/2 + n - 1), 2) = vs2(1 : n + N/2);$$

$$tri(n1 : 2 : n1 + 2 * (N/2 + n - 1), 3) = vs2(2 : n + N/2 + 1);$$

$$tri(n1 + 1 : 2 : n1 + 2 * (N/2 + n - 1), 1) = vs1(1 : n + N/2 - 1);$$

$$tri(n1 + 1 : 2 : n1 + 2 * (N/2 + n - 1), 2) = vs2(2 : n + N/2);$$

$$tri(n1 + 1 : 2 : n1 + 2 * (N/2 + n - 1), 3) = vs1(2 : n + N/2);$$

$$n1 = n1 + 2 * (N/2 + n - 1) + 1;$$

$$nn = nn + N/2 + n;$$

$$vs1 = mm2 : mm2 + N/2 + (n - 1);$$

$$vs2 = mm2 - (N/2 + n + 1) : mm2 - 1;$$

$$tri(mm - 2 * (N/2 + n - 1) : 2 : mm, 1) = vs2(1 : n + N/2);$$

$$tri(mm - 2 * (N/2 + n - 1) : 2 : mm, 2) = vs1;$$

$$tri(mm - 2 * (N/2 + n - 1) : 2 : mm, 3) = vs2(2 : n + N/2 + 1);$$

$$tri(mm - 2 * (N/2 + n - 1) + 1 : 2 : mm, 1) = vs2(2 : n + N/2);$$

$$tri(mm - 2 * (N/2 + n - 1) + 1 : 2 : mm, 2) = vs1(1 : n + N/2 - 1);$$

$$tri(mm - 2 * (N/2 + n - 1) + 1 : 2 : mm, 3) = vs1(2 : n + N/2);$$

$$mm = mm - 2 * (N/2 + n - 1) - 1;$$

```
mm2 = mm2-(N/2+n+1);
```

```
end
```

```
size_tri = size(tri,1);
```

```
hh = zeros(size_tri,1);
```

```
for i = 1:size_tri
```

```
    hh(i,1) = sum(vertex_x11([tri(i,1) tri(i,2) tri(i,3)]))+  
    sum(vertex_y11([tri(i,1) tri(i,2) tri(i,3)]));
```

```
end
```

```
nnid1 = zeros(1,size(pore11,2));
```

```
nnid2 = zeros(1,size(pore11,2));
```

```
nnid3 = zeros(1,size(pore11,2));
```

```
nnid4 = zeros(1,size(pore11,2));
```

```
nnid5 = zeros(1,size(pore11,2));
```

```
nnid6 = zeros(1,size(pore11,2));
```

```
for i = 1:size(pore11,2)
```

```
    nnid1(i) = find(abs(hh-poreid1(i)) < 0.00001);
```

```
    nnid2(i) = find(abs(hh-poreid2(i)) < 0.00001);
```

```
    nnid3(i) = find(abs(hh-poreid3(i)) < 0.00001);
```

```
    nnid4(i) = find(abs(hh-poreid4(i)) < 0.00001);
```

```
    nnid5(i) = find(abs(hh-poreid5(i)) < 0.00001);
```

```
    nnid6(i) = find(abs(hh-poreid6(i)) < 0.00001);
```

```
end
```

```

pores = zeros(1,3*3*size(pore11 ,2));
pores(1:end) = [tri(nnid1,:) tri(nnid2,1:3) tri(nnid3,1:3)];

if i2>0

    nn1 = 3;
    nn2 = 3;
    s = 1;
    s2 = 1;
    for i = 1:i2
        interior1(s:s+2*(i-1)) =
            tri(nnid1(nn1:nn1+2*(i-1)),2);
        interior2(s2:s2+2*(Npore-3)-2*(i-1)) =
            tri(nnid2(nn2:nn2+2*(Npore-3)-2*(i-1)),2);
        interior3(s2:s2+2*(Npore-3)-2*(i-1)) =
            tri(nnid3(nn2:nn2+2*(Npore-3)-2*(i-1)),2);
        interior4(s:s+2*(i-1)) = tri(nnid4(nn1:nn1+2*(i-1)),2);
        interior5(s2:s2+2*(Npore-3)-2*(i-1)) =
            tri(nnid5(nn2:nn2+2*(Npore-3)-2*(i-1)),2);
        interior6(s:s+2*(i-1)) = tri(nnid6(nn1:nn1+2*(i-1)),2);
        s = s+2*(i-1)+1;
        nn1 = nn1+i*2+1;
        s2 = s2+2*(Npore-3)-2*(i-1)+1;
        nn2 = nn2+2*(Npore-3)-2*(i-1)+5;
    end

end

end

```

```

%% Preparation to Obtain the Laplacian Operator on the Hex Grid
%
%
% The main hex grid program creates the 2D Laplacian matrix in sparse band
% storage mode using the function "spdiags". The way spdiags(inputs) works
% is that it only stores the nonzero diagonals of a particular matrix and
% references only those values when calling any matrix inversion or any
% other operation. In this manner, the function spdiags is extremely
% efficient when it comes to working with huge banded matrices such as in
% our diffusion problem. The zeros in these banded matrices would take up
% too much extra memory using conventional matrix storage schemes. In
% order to call the function spdiags we need to have all the necessary
% inputs to give it. The function call for "spdiags" is:
%
%
% A = spdiags(B-matrix, d, m, n)
%
%
% A      == The m by n banded matrix one wishes to create and store
%          using spdiags
% B-matrix == A min(m,n)-by-p matrix, usually (but not necessarily) full,
%             whose columns are the diagonals of A.
% d      == A vector of length p whose integer components specify the
%             diagonals in A.
%
%
% We proceed in the next few lines to generate the B-matrix and d column

```

```

% vector. The reader is referred online to:
% http://www.mathworks.com/help/techdoc/ref/spdiags.html for a more
% complete discussion of how the diagonals of a banded matrix are labeled
% by integers in the spdiag function call.
%
% The way the B-matrix is created is in sections. While the full banded
% matrix is never stored or created in this program (thanks to the "spdiag")
% the creation of the inputs necessary for spdiag to work such as B-matrix
% or d vector frequently required one to focus and think about how the
% full banded matrix looks.
%
% The full matrix laplacian operator (call it full(A)) for the hex grid can
% be divided into sections. Each section is a different diagonal on the
% hex grid lattice. As an example, one is referred to FIG 1 in this code.
% In this section, points 01 02 03 04 would be a section in the matrix
% full(A) and points 05 06 07 08 09 would be a different section.

s = 0;
y = zeros(1,N/2);

for i = 1:N/2
    y(i) = N/2+3+s;
    s = s + N/2+2+(i-1);
end

d = zeros(N+5,1);
z = -(N/2+2);

```

```
d(1) = -(N/2+2)+1;
```

```
d(N+5) = N/2+1;
```

```
z1 = N/2+2;
```

```
for n = 1:N/2
```

```
    d(n+1) = z;
```

```
    z = z-1;
```

```
    d(N+5-(n)) = z1;
```

```
    z1 = z1+1;
```

```
end
```

```
%% Generating the 2D Laplacian Operator on the Hex Grid Lattice
```

```
%
```

```
%
```

```
% The first column of B-matrix contains the nonzero elements of the  
% diagonal number specified by the first element in vector d. The second  
% column of the B-matrix contains the nonzero elements of the diagonal  
% number specified by the second element in vector d and so on and so on.
```

```
% The B-matrix is filled by moving along the down rows of the full(A)  
% matrix. Each "section" of full(A) is grouped and allocated into its  
% proper location in the B-matrix separately. The "sections" of the  
% full(A) matrix is described in the previous commented section.
```

```
% Specifically, each point on the hex grid uses its six neighboring points  
% to form the approximation to the laplacian. The diagonals used in the  
% full(A) matrix are the same in each section. Visually the sections are  
% simply different diagonal-strips on the hex grid as explained in the
```

*% previous section. If the boundary conditions on the hex grid are known,  
 % then the first non-constant point is point N/2+3 and the diagonal-strip  
 % in this section contains N/2 points of interest. The diagonals to be  
 % used for this first section are diagonals -(N/2+2), -(N/2+1), -1,0,1,  
 % N/2+2 and N/2+3. The diagonal numbers and how they relate to the full(A)  
 % matrix are explained in the MATLAB website given earlier. Suffice to say  
 % that the negative diagonals are diagonals below the main diagonal in the  
 % matrix and the positive diagonals are the diagonals above the main  
 % diagonal in the matrix.*

```
Nhalf = ((N/2+1)^2+sum(0:N/2));
```

```
kev = 8.617343*10^(-5);
```

```
L = 30*10^-6;
```

```
D0 = 0.23*exp(-.67/(kev*T));
```

```
D0 = D0*(1/100)*(1/100);
```

```
tdiffusion = (h^2*L^2)/(D0);
```

```
EE = tdiffusion;
```

```
dt = (EE*D0)/L^2;
```

```
r = (3*h^2)/dt;
```

```
d(N/2+2:N/2+4) = [-1 0 1];
```

```
sized1 = size(d,1);
```

```
B = zeros(Nhalf, size(d,1));
```

```
B(1:end, N/2+3) = 1;
```

```
z = ones(Nhalf,1);
```

```

VarDx = zeros(Nhalf, size(d,1));
VarDy = zeros(Nhalf, size(d,1));
for n = 1:N/2
    if n ~N/2
        B(y(n):y(n)+N/2-2+n, [n:n+1 N/2+2 N/2+4 size(d,1)-n-1:size(d,1)-n]) = -1;
        VarDx(y(n):y(n)+N/2-2+n, n+1) = 1;
        VarDx(y(n):y(n)+N/2-2+n, size(d,1)-n-1) = -1;
        B(y(n):y(n)+N/2-2+n, N/2+3) = 6+(3*h^2)/dt;
        z(y(n):y(n)+N/2-2+n) = (3*h^2)/dt - 6;
        VarDy(y(n):y(n)+N/2-2+n, [n N/2+4]) = 1;
        VarDy(y(n):y(n)+N/2-2+n, [N/2+2 size(d,1)-n]) = -1;

    else

        B(y(n):y(n)+N/2-2+n, n:n+1) = -2;
        B(y(n):y(n)+N/2-2+n, [N/2+2 N/2+4]) = -1;
        VarDx(y(n):y(n)+N/2-2+n, n+1) = 1;
        VarDx(y(n):y(n)+N/2-2+n, n) = -1;
        B(y(n):y(n)+N/2-2+n, N/2+3) = 6+(3*h^2)/dt;
        z(y(n):y(n)+N/2-2+n) = (3*h^2)/dt - 6;
        VarDy(y(n):y(n)+N/2-2+n, [N/2+4 n]) = 1;
        VarDy(y(n):y(n)+N/2-2+n, [N/2+2 n+1]) = -1;

    end
end
end

```

```

B(2:N/2,[N/2+2 N/2+4]) = -1;
B(2:N/2, [ sized1-1 sized1 ]) = -2;
B(2:N/2,N/2+3) = 6+(3*h^2)/dt;
z(2:N/2) = (3*h^2)/dt - 6;
VarDx(2:N/2, sized1) = -1;
VarDx(2:N/2, sized1-1) = 1;
VarDy(2:N/2, [N/2+2 sized1]) = -1;
VarDy(2:N/2, [N/2+4 sized1-1]) = 1;

```

```

B(1, N/2+4) = -2;
B(1, sized1) = -2;
B(1, sized1-1) = -2;
B(1,N/2+3) = 6+(3*h^2)/dt;
z(1) = (3*h^2)/dt - 6;

```

```

B(N/2+1, N/2+2) = -2;
B(N/2+1, sized1-1) = -2;
B(N/2+1, sized1) = -2;
B(N/2+1,N/2+3) = 6+(3*h^2)/dt;
z(N/2+1) = (3*h^2)/dt - 6;

```

```

% BOTTOM LEFT BOUNDARY

```

```

for i = 1:(N-2)/2

```

```

B(y(i)-1, [i N+5-i]) = -1;
B(y(i)-1, [N/2+4 N+4-i]) = -2;
B(y(i)-1, N/2+3) = 6+(3*h^2)/dt;
VarDx(y(i)-1, N+4-i) = 1;
VarDx(y(i)-1, N+4) = -1;
VarDy(y(i)-1,[i N/2+4 ]) = 1;
VarDy(y(i)-1,[N+5-i N+4-i]) = -1;
z(y(i)-1) = (3*h^2)/dt - 6;

```

**end**

*% TOP BOUNDARY*

```

for i = 1:(N-2)/2
    B(y(1+i)-2, [i+1 N+4-i ]) = -1;
    B(y(1+i)-2, [N+5-i N/2+2 ] ) = -2;
    B(y(1+i)-2, N/2+3) = 6+(3*h^2)/dt;
    z(y(1+i)-2) = (3*h^2)/dt - 6;
    VarDx(y(1+i)-2, N+4-i) = 1;
    VarDx(y(1+i)-2, i+1) = -1;
    VarDy(y(1+i)-2, [N/2+2 N+5-i ] ) = 0;

```

**end**

```

B(y(N/2)-1, N/2+3) = 6+(3*h^2)/dt;
B(y(N/2)-1, [i N/2+4]) = -3;
z(y(N/2)-1) = (3*h^2)/dt - 6;

```

```

B(y(N/2)-1+N, N/2+3) = 6+(3*h^2)/dt;
B(y(N/2)-1+N, [N/2+2 i+1]) = -3;

```

```
z(y(N/2)-1+N) = (3*h^2)/dt - 6;
```

```
xx = 0:(10*10^ -6)/10:LL;
```

```
g2 = size(xx,2);
```

```
slopeyy0 = (.9-.1)/((1/450)-(1/700));
```

```
bfactoryy0 = .9-(slopeyy0)*(1/450);
```

```
yy0=slopeyy0*(1/T)+bfactoryy0;
```

```
dude = zeros(1,g2);
```

```
dude(1:g2) = yy0;
```

```
dude = dude';
```

```
B(pores,:) = 0;
```

```
B(pores,N/2+3) = 6+(3*h^2)/dt;
```

```
z(pores) = 0;
```

```
VarDx(pores,:) = 0;
```

```
VarDy(pores,:) = 0;
```

```
sizeB = size(B,2);
```

```
sizeB1 = size(B,1);
```

```

for n = 1:sizeB
    m = B(:,n);
    m = m (mod((1:sizeB1)-d(n)-1, sizeB1)+1);
    B(:,n) = m;
end

sizeDx = size(VarDx,2);
sizeDy = size(VarDy,2);

for n = 1:sizeDx
    m = VarDx(:,n);
    m = m (mod((1:sizeB1)-d(n)-1, sizeB1)+1);
    VarDx(:,n) = m;
end

for n = 1:sizeDy
    m = VarDy(:,n);
    m = m (mod((1:sizeB1)-d(n)-1, sizeB1)+1);
    VarDy(:,n) = m;
end

B1 = -B;
B1(:,N/2+3) = z;
B2 = B1;
B2(:,N/2+3) = 0;
A = spdiags(B,d,Nhalf,Nhalf);

```

```

A1 = spdiags(B1,d,Nhalf,Nhalf);
A11 = spdiags(B2,d,Nhalf,Nhalf);
ff = A_tilde = -1 & A_tilde = 6+(3*h^2)/dt & A_tilde=0 & A_tilde=1 & A_tilde=-2 & A_tilde=-3;
A(ff) = -1;
ff = find(A1_tilde = 1 & A1_tilde=(3*h^2)/dt - 6 & A1_tilde=0 & A1_tilde=2 & A1_tilde=3);
A1(ff) = 1;
A11(ff) = 1;
Dx = spdiags(VarDx,d(1:sizeDx),Nhalf,Nhalf);
Dy = spdiags(VarDy,d(1:sizeDy),Nhalf,Nhalf);
ff = find(Dx < -1);
Dx(ff) = -1;
ff = find(Dx>1);
Dx(ff) = 1;
ff = find(Dy<-1);
Dy(ff) = -1;
ff = find(Dy>1);
Dy(ff) = 1;

zz = zeros((N+1)^2-((N/2*N/2)+N/2),1);
z = zeros(Nhalf,1);
z(pores) = yy0;

v = 1;
h11 = 1;
vertex_x11 = vertex_x11./xmax;
vertex_y11 = vertex_y11./xmax;
ymax = max(vertex_y11);

```

```

Beta = 1;
Gamma = 0;

z1 = z;

ff = find(A1==(3*h^2)/dt - 6);
A1(ff) = -6;

ff = (N+1)^2-((N/2*N/2)+N/2)+1;
ff = ff/2;
uox = vertex_x11(ff);
uoy = vertex_y11(ff);
FFF = moviein(timesteps);
AA = ((3*h^2)/2)*((L^2)/(D0));

zjj01 = z1;

for f = 1:500

    eev = AA*Langmuir(z1,T)/((4*10^14));
    eev(pores) = 0;
    bb = r*z1+(A1*z1).*(Beta)-eev;
    bb(pores) = (r+6)*z1(pores);
    while h11>0.001
        evap11 = AA*Langmuir(zjj01,T)/((4*10^14));
        evap11(pores) = 0;

```

```

    b = -evap11+bb;

    z1 = A\b;

    h11 = sum(abs(z1-zjj01));

    zjj01 = z1;

end

h11 = 1;

end

ysurf = z1(max(interior1+2));

for f = 1:timesteps
    dude = Knud_diffusion(RR,LL,T,dude,ysurf,yy0,xx);
    z1(pores) = dude(end-1);

    eev = AA*Langmuir(z1,T)/((4*10^14));
    eev(pores) = 0;
    bb = r*z1+(A1*z1).*(Beta)-eev;
    bb(pores) = (r+6)*z1(pores);
    while h11>0.001
        evap11 = AA*Langmuir(zjj01,T)/((4*10^14));
        evap11(pores) = 0;

        b = -evap11+bb;

```

```
z1 = A\b;
```

```
h11 = sum(abs(z1-zjj01));
```

```
zjj01 = z1;
```

```
end
```

```
h11 = 1;
```

```
ysurf = z1(max(interior1+2));
```

```
end
```

## Appendix B

### Functions and Subroutines

```
function y = Knud_diffusion(RR,L,T,yy,ysurf,yy0,x2)

%The following function “Knud_diffusion” is used to model the cesium
% coverage along the pore walls at each time step:

kev = 8.617343*10(-5);
sigma1 = 4*1018;
R = rrr(RR,.03);
dh = (10*10(-6))/10;
D0 = (1/100)*(1/100)*0.23*exp(-.67/(kev*T));
dt = zeros(1,2);
dt(1) = (dh)2/D0;
dt(2) = (.01*sigma1)/(100*100*Langmuir(max(yy),T));
dt = min(dt);
dt = (dt*D0)/L2;

z2 = find(x2 == 10*10(-6));
e2 = find(x2 == L-10*10(-6));

g2 = size(x2,2);

x = [-1: 1/1000 :0-1/1000  0-1/1000+1/10000: 1/10000 :0+1/1000
      0+1/1000+1/1000: 1/1000 :1];
```

```

x = x*10*10^-6;

ee = ones(g2,1);

A = spdiags([-ee (2*(dh.^2)/(dt))+2*ee -ee], -1:1,g2,g2);
A(1,:) = 0;
A(1,1) = (2*(dh)^2/(dt));
A(g2,:) = 0;
A(g2,g2) = 1;

A1 = spdiags([ee (2*(dh.^2)/(dt))-2*ee ee], -1:1,g2,g2);
A1(1,:) = 0;
A1(1,1) = (2*(dh)^2/(dt));
A1(g2,:) = 0;
A1(g2,g2) = 1;
error = 1;

y = yy;
y11 = y;
Ssource = 100*100*Langmuir(yy0,T)*(1-x2/L);
S = zeros(1,g2);

for i = 1:g2

    if i<=z2

        xnew = x+x2(i);

```

```
index = find(xnew>=0);
```

```
S(i) = trapz(xnew(index), poreprob(xnew(index), x2(i), x2, y, R, T))+  
trapz([xnew(end) x2(z2+i:end)],  
poreprob([xnew(end) x2(z2+i:end)], x2(i), x2, y, R, T));
```

```
elseif i>=e2
```

```
xnew = x+x2(i);
```

```
index = find(xnew<=L);
```

```
S(i) = trapz([x2(1:i-(g2-e2)-1) xnew(1) ],  
poreprob([ x2(1:i-(g2-e2)-1) xnew(1)] , x2(i), x2, y, R, T))+  
trapz(xnew(index), poreprob(xnew(index), x2(i), x2, y, R, T));
```

```
else
```

```
S(i) = trapz(x2(1:i-(g2-e2)), poreprob(x2(1:i-(g2-e2)), x2(i), x2, y, R, T))+  
trapz(x+x2(i), poreprob(x+x2(i), x2(i), x2, y, R, T))+  
trapz(x2(i+z2-1:end), poreprob(x2(i+z2-1:end), x2(i), x2, y, R, T));
```

```
end
```

```
end
```

```
gsource = S+Ssource;
```

```

gsource = gsource';
gsource1 = gsource;

fevap = Langmuir(y,T)*100*100;
fevap1 = Langmuir(y,T)*100*100;

while error > .01
    b = A1*y + ((dh.^2*L^2)./(D0*sigma1)).*(gsource+gsource1)
        - ((dh.^2*L^2)./(D0*sigma1)).*(fevap+fevap1);

    b(end) = ysurf;
    y1 = A\b;

    fevap1 = Langmuir(y1,T)*100*100;
    error = sum(abs(y1-y11));
    y11 = y1;

    for i = 1:g2

        if i <= z2

            xnew = x+x2(i);

            index = find(xnew >= 0);

            S(i) = trapz(xnew(index), poreprob(xnew(index), x2(i), x2, y1, R, T)) +
                trapz([xnew(end) x2(z2+i:end)]),

```

```
poreprob ([xnew(end) x2(z2+i:end)], x2(i), x2, y1, R, T));
```

```
elseif i>=e2
```

```
xnew = x+x2(i);
```

```
index = find(xnew<=L);
```

```
S(i) = trapz ([x2(1:i-(g2-e2)-1) xnew(1) ],
```

```
poreprob ([ x2(1:i-(g2-e2)-1) xnew(1)] , x2(i), x2, y1, R, T))+
```

```
trapz(xnew(index), poreprob(xnew(index), x2(i), x2, y1, R, T));
```

```
else
```

```
S(i) = trapz(x2(1:i-(g2-e2)),
```

```
poreprob(x2(1:i-(g2-e2)), x2(i), x2, y1, R, T))+
```

```
trapz(x+x2(i), poreprob(x+x2(i), x2(i), x2, y1, R, T))+
```

```
trapz(x2(i+z2-1:end), poreprob(x2(i+z2-1:end), x2(i), x2, y1, R, T));
```

```
end
```

```
end
```

```
gsource1 = Ssource+S;
```

```
gsource1 = gsource1 ';
```

```
end
```

```

y = y1;
end

function y = poreprob(x,L,x0,theta0,R,T)
%The following function is called by ‘‘Knud_diffusion’’
% in evaluating the flux integrals:

theta = interp1(x0,theta0,x);

xx = ((x-L)/(sqrt(2)*R)).^2;

y = ((1)./(2*R)).*(1-(sqrt(xx).*(3+xx))./(2+xx).^ (3/2));
y = Langmuir(theta,T)*100*100.*y;

end

function y = Langmuir(x,T)
%The following function gives the interpolation of the evaporation rate
%of cesium off tungsten from Langmuir’s data shown in table 6.1:

B_a = column 3 table 6.1;
A_a = column 2 table 6.1;
theta = column 1 table 6.1;

AA = interp1(theta,A_a,x);
BB = interp1(theta,B_a,x);
y = exp(AA-BB./T);

```

```

if min(x) < .01
    n1 = find(x < .01);
    y(n1) = 0;
end

if max(x) > .95
    n2 = find(x > .95);
    AA = interp1(theta, A_a, .95);
    BB = interp1(theta, B_a, .95);
    AA1 = interp1(theta, A_a, .94);
    BB1 = interp1(theta, B_a, .94);
    dy = (exp(AA-BB./T) - exp(AA1-BB1./T)) / .01;
    y(n2) = exp(AA-BB./T) + dy * (x(n2) - .95);
end

```

## Bibliography

- [1] B.H Alexander and R.W Balluffi. The mechanism of sintering of copper. *Acta Metallurgica*, 5(11):666 – 677, 1957.
- [2] Grazyna Antczak and Gert Ehrlich. The beginnings of surface diffusion studies. *Surface Science*, 589(1-3):52 – 66, 2005.
- [3] Joseph A. Becker. Thermionic and adsorption characteristics of caesium on tungsten and oxidized tungsten. *Phys. Rev.*, 28:341–361, Aug 1926.
- [4] Richard Charles Leslie Bosworth. The mobility of sodium on tungsten. *Proc. Royal Society London A.*, (150):58–76, 1935.
- [5] W. C. DeMarcus. The problem of knudsen flow part i. general theory. *United States Atomic Energy Commission Report K-1302*, 1, September 1956.
- [6] W. C. DeMarcus. The problem of knudsen flow part ii. solution of integral equations with probability kernals. *United States Atomic Energy Commission Report K-1302*, 1, October 1956.
- [7] W. C. DeMarcus. The problem of knudsen flow part iii. solutions for one-dimensional systems. *United States Atomic Energy Commission Report K-1302*, 1, September 1957.
- [8] W. C. DeMarcus. The problem of knudsen flow part v. application of the theory of radiative transfer. *United States Atomic Energy Commission Report K-1302*, 1, July 1957.

- [9] D. H. Dowell, K. J. Davis, K. D. Friddell, E. L. Tyson, C. a. Lancaster, L. Miliman, R. E. Rodenburg, T. Aas, M. Bemes, S. Z. Bethel, P. E. Johnson, K. Murphy, C. Whelen, G. E. Busch, and D. K. Remelius. First operation of a photocathode radio frequency gun injector a. high duty factor. *Appl. Phys. Lett.*, 63(15):2035–2037, 1993.
- [10] DH Dowell, I Bazarov, B Dunham, K Harkay, C Hernandez-Garcia, R Legg, H Padmore, T Rao, J Smedley, and W Wan. Cathode r and d for future light sources. *Nucl. Instr. and Meth. A*, 622:685–697, 2010.
- [11] G Ehrlich and K Stolt. Surface diffusion. *Annual Review of Physical Chemistry*, 31(1):603–637, 1980.
- [12] L.R. Falce and R.E. Thomas. Controlled porosity dispenser cathode: Iridium-barium oxide. *Tech. Dig. of IEEE IEDM*, 24:156–159, 1978.
- [13] Alexander L Fetter and John Dirk Walecka. *Quantum theory of many-particle systems*. McGraw-Hill, San Francisco, 1971.
- [14] M. H. Ghatee and H. Shams-Abadi. Linear exp-6 isotherm for compressed molten cesium over the whole liquid range including metalnonmetal transition and tc. *The Journal of Physical Chemistry B*, 105(3):702–710, 2001.
- [15] Robert Gomer. Diffusion of adsorbates on metal surfaces. *Rep. Prog. Phys.*, 53:917–1002, 1990.
- [16] Elias P. Gyftopoulos and Jules D. Levine. Work function variation of metals coated by metallic films. *J. Appl. Phys.*, 33(1):67, January 1962.

- [17] Jean-Pierre Hansen and Ian R. McDonald. *Theory of simple liquids*. Academic Press, London ; New York, 1976.
- [18] K. Huang. *Statistical mechanics*. Wiley, 1963.
- [19] R. Lawrence Ives, Louis R. Falce, George Miram, and George Collins. Controlled-porosity cathodes for high-current-density applications. *IEEE Trans. Plasma Sci.*, 38(6):1345 – 1353, June 2010.
- [20] R.L. Ives, L.R. Falce, S. Schwartzkopf, and R. Witherspoon. Controlled porosity cathodes from sintered tungsten wires. *Electron Devices, IEEE Transactions on*, 52(12):2800 – 2805, dec. 2005.
- [21] Kevin L. Jensen. Electron emission physics. In Kevin L. Jensen, editor, *Electron Emission Physics*, volume 149 of *Advances in Imaging and Electron Physics*, pages 147 – 279. Elsevier, 2007.
- [22] Kevin L. Jensen and Eric J. Montgomery. Photoemission theory and the development of high performance photocathodes. *Journal of Computational and Theoretical Nanoscience*, 6(8):1754–1769, 2009.
- [23] K.L. Jensen, Y.Y. Lau, and B. Levush. Migration and escape of barium atoms in a thermionic cathode. *Plasma Science, IEEE Transactions on*, 28(3):772 – 781, jun 2000.
- [24] S.H. Kong, J. Kinross-Wright, D.C. Nguyen, and R.L. Sheffield. Photocathodes for free electron lasers. *Nuclear Instruments and Methods in Physics Research*

*Section A: Accelerators, Spectrometers, Detectors and Associated Equipment*, 358(1-3):272 – 275, 1995. Proceedings of the Sixteenth International Free Electron Laser Conference.

- [25] Irving Langmuir and K. H. Kingdon. Thermionic effects caused by alkali vapors in vacuum tubes. *Science*, 57(1463):pp. 58–60, 1923.
- [26] Irving Langmuir and John Bradshaw Taylor. The mobility of caesium atoms adsorbed on tungsten. *Phys. Rev.*, 40:463–464, May 1932.
- [27] J.D. Levine and E.P. Gyftopoulos. Adsorption physics of metallic surfaces partially covered by metallic particles. i atom and ion desorption energies. *Surface Science*, 1(2):171 – 193, 1964.
- [28] J. W. Lewellen. High-brightness electron guns for linac-based light sources. *Proc. of SPIE - Int. Soc. Optical Engineering*, 22:5534, 2004.
- [29] Gilbert Newton Lewis and Merle Randall. *Thermodynamics*. McGraw-Hill, New York, 2 edition, 1961.
- [30] H. M. Love and H. D. Wiederick. Cesium diffusion at a tungsten surface. *Canadian Journal of Physics*, 47(6):657–663, 1969.
- [31] J. Gilbert Malone. The electric moment as a measure of the ionic nature of covalent bonds. *Journal of Chemical Physics*, 1:197, 1933.

- [32] E. J. Montgomery, D. W. Feldman, P. G. O'Shea, Z. Pan, N. Sennett, and K. L. Jensen. Electron emission from alkali-coated metal photocathodes. *Proceedings of the 11th IEEE Int'l Vac. Elec. Conf.*, 79, 2010.
- [33] E. J. Montgomery, Z. Pan, J Leung, D. W. Feldman, P. G. OShea, and K. L. Jensen. Towards a robust, efficient dispenser photocathode: the effect of recession on quantum efficiency. *Advanced Accelerator Concepts*, 1086:599–603, 2009.
- [34] E. J. Montgomery, Z. Pan, B. C. Riddick, P. G. O'Shea, D. W. Feldman, K. L. Jensen, R. L. Ives, and L. R. Falce. Enhanced lifetime hybrid-diffuser cesium reservoir photocathode. *Proc. of Adv. Accel. Concepts Workshop*, 2012.
- [35] Eric Montgomery. Sintered wire cesium dispenser photocathode. US Patent, Patent number: 13587200.
- [36] Eric J. Montgomery. *Characterization of Quantum Efficiency and Robust Cesium-Based Photocathodes*. PhD thesis, University of MD College Park, 2007.
- [37] Eric J. Montgomery, Donald W. Feldman, PG Oshea, Z Pan, N Sennett, Kevin L. Jensen, and Nathan A. Moody. Advances in cesium dispenser photocathodes: Modeling and experiment. *Journal of Directed Energy*, 3:66–79, 2008.
- [38] N. Moody, D.W. Feldman, P.G. O'Shea, and K.L. Jensen. Fabrication and measurement of low workfunction cesiated dispenser photocathodes. In *Particle*

*Accelerator Conference, 2005. PAC 2005. Proceedings of the*, pages 2953 – 2955, may 2005.

- [39] N. A. Moody, K. L. Jensen, D. W. Feldman, P. G. OShea, and E. J. Montgomery. Prototype dispenser photocathode: Demonstration and comparison to theory. *Appl. Phys. Lett.*, 90(11):114108–114103, 2010.
- [40] D. C. Nguyen, P. L. Colestock, S. S. Kurennoy, D. E. Rees, a. H. Regan, S. Russell, D. L. Schrage, R. L. Wood, L. M. Young, T. Schultheiss, V. Christina, M. Cole, J. Rathke, J. Shaw, C. Eddy, R. Holm, R. Henry, and J. Yater. Overview of the 100 ma average-current rf photoinjector. *Nucl. Instr. and Meth. A*, 528(1-2):71–77, 2004.
- [41] Lars Onsager and Nicholas N. T. Samaras. The surface tension of debye-h<sup>u</sup>ckel electrolytes. *The Journal of Chemical Physics*, 2(8):528, 1934.
- [42] Patrick G. O’Shea, SC Bender, BE Carlsten, JW Early, Donald W. Feldman, RB Feldman, WJD Johnson, AH Lumpkin, RI Sheffield, RW Springer, WE Stein, and LM Young. Performance of the photoinjector accelerator for the los alamos free-electron laser. *Proc IEEE Part Accel Conf*, pages 2754–2756 vol.5, 1991.
- [43] Patrick G. O’Shea and Henry P. Freund. Free-electron lasers: Status and applications. *Science*, 292:1853, June 2001.

- [44] Zhigang Pan, Kevin L. Jensen, and Patrick G. O'Shea. Modeling the quantum efficiency of controlled porosity dispenser photocathodes. *Appl. Phys. Lett.*, 100(3), January 2012.
- [45] Y. P. Pao. Knudsen flow through a long circular tube. *Phys. Fluids*, 13:527, 1970.
- [46] L. Pauling. *The Nature of the Chemical Bond: An Introduction to Modern Structural Chemistry*. The George Fisher Baker non-resident lectureship in chemistry at Cornell University [v. 18]. Cornell Univ, 1960.
- [47] David A. Reed and Gert Ehrlich. Surface diffusion, atomic jump rates and thermodynamics. *Surface Science*, 102(2-3):588 – 609, 1981.
- [48] T.N. Rhodin and G. Ertl. *The Nature of the Surface Chemical Bond*. North-Holland Pub. Co.
- [49] G. D. Smith. *Numerical Solution of Partial Differential Equations*. Oxford University Press, New York, 1965.
- [50] A. H. Sommer. The element of luck in research – photocathodes 1930 to 1980. *J. Vac. Sci. Technol.*, 1:119–124, 1983.
- [51] William E. Spicer and Alberto Herrera-Gomez. Modern theory and applications of photocathodes. In *Proceedings of SPIE*, volume 2022, feb 1993.
- [52] W. Steckelmacher. Effect of cross-sectional shape on molecular-flow in long tubes. *Vacuum*, 28:269, 1978.

- [53] John Bradshaw Taylor and Irving Langmuir. The evaporation of atoms, ions and electrons from caesium films on tungsten. *Phys. Rev.*, 44:423–458, Sep 1933.
- [54] R.E. Thomas, J.W. Gibson, G.A. Haas, and Jr. Abrams, R.H. Thermionic sources for high-brightness electron beams. *Electron Devices, IEEE Transactions on*, 37(3):850–861, mar 1990.
- [55] Chen-Show Wang. High photoemission efficiency of submonoayer cesium-covered surfaces. *Journal of Applied Physics*, 48(4), 1977.
- [56] R.W. Warren, We Stein, Mt Lynch, R. L. Sheffield, and J. S. Fraser. The los-alamos free-electron laser-accelerator performance. *Nucl. Instr. and Meth. A*, 237(1-2):180–186, 1985.
- [57] W.L. Winterbottom and J.P. Hirth. Diffusional contribution to the total flow from a knudsen cell. *Journal of Chemical Physics*, 37(4):784–793, 1962.